Robust Channel Estimation, Localization, and Tracking in Visible Light Systems under Signal-Dependent Noise

Author: **Sara Hassan Elfar**

Supervisor: Prof. Salama Ikki
Co-Supervisor: Dr. Maysa Yaseen

Submitted to
Lakehead University
In Partial Fulfillment of the Requirements for the degree of

Doctor of Philosophy

in
Electrical and Computer Engineering

Lakehead University
September 26, 2025

Acknowledgements

First and foremost, I am grateful to Almighty Allah (Subhanahu Wa Ta'ala) for His countless blessings and for granting me the knowledge and strength to accomplish my research work.

I dedicate this work with deep love and gratitude to my parents, **my mother Zeinab Emam and my father Hassan Elfar**; to my beloved husband, **Salahuddin Elkazak**; to my cherished daughters, **Roa and Raghad**, who have been my greatest source of joy, strength, and motivation; to my sister, **Youssra**, and my brother, **Hassan**, for their constant support and encouragement; and to the blessed memory of my grandmother, **Fatma Ziadan**.

I also extend my heartfelt appreciation to the blessed memory of my husband's parents—**my father-in-law, Mohammad Elkazak, and my mother-in-law, Eman Abdul-Moniem**—whose prayers, love, and encouragement have always been with me. Without their sacrifices, prayers, and love, this achievement would not have been possible.

I express my sincere gratitude to my supervisor, **Prof. Salama Ikki**, and my co-supervisor, **Dr. Maysa Yaseen**. Their continuous guidance, support, and encouragement have been invaluable throughout this work. Without their advice and thoughtful input on my research ideas and writings, this accomplishment would not have been possible.

Finally, I am deeply thankful to my colleagues at **Lakehead University** for their friendship, support, and stimulating discussions, which have enriched both my academic and personal journey. I would also like to express my gratitude to **Pharos University in Alexandria** and to my colleagues there for their support and encouragement throughout this work.

Declaration of Authorship

I, **Sara Hassan Elfar**, declare that the dissertation, which I hereby submit for the degree of Doctor of Philosophy at Lakehead University, is my own work and has not previously been submitted by me for a degree at this or any other tertiary institution. This is a true copy of the thesis, including any required final revisions, as accepted by my examiners.

Abstract

VISIBLE Light Communication (VLC) is an emerging wireless technology that employs light-emitting diodes (LEDs) or lasers to transmit data over the visible light spectrum. Due to its inherent advantages, such as license-free spectrum, high data rates, low power consumption, and enhanced security, VLC has attracted significant attention for a broad range of applications, including indoor wireless networking, vehicular communications, underwater communications, smart lighting, and indoor positioning systems. Additionally, VLC is immune to electromagnetic interference, making it particularly suitable for environments where radio-frequency systems are undesirable or restricted.

Despite these advantages, VLC systems face several challenges, including limited coverage range, susceptibility to interference from ambient light sources, and performance degradation under mobility. One of the most critical challenges arises from noise, which may originate from the inherent properties of light and hardware components. In particular, signal-dependent shot noise (SDSN) and relative intensity noise (RIN) significantly degrade the accuracy of channel estimation and localization in practical VLC systems.

In the first part of this thesis, we focus on channel estimation in the presence of SDSN, proposing a neural-network-augmented estimation framework that integrates with traditional estimators such as least squares (LS) and maximum likelihood estimation (MLE). We develop a complete mathematical framework enabling analytical mean-square-error (MSE) derivations and fair benchmarking. Simulations show that, under SDSN, the proposed method consistently outperforms LS while remaining competitive when SDSN is absent.

In the second part, we extend to visible light positioning (VLP) under SDSN. For a

SISO VLC system, we study range estimation using the extended Kalman filter (EKF), MLE, and nonlinear least squares (NLS), and establish Bayesian Cramér–Rao lower bounds (BCRLBs). Monte Carlo results confirm the analysis and demonstrate EKF's superior accuracy.

Finally, we address 2D localization and tracking for dynamic targets in a multiple-input single-output (MISO) VLC configuration. Accounting for both SDSN and RIN, we derive a closed-form 2D-BCRLB and show that EKF's recursive updates yield superior real-time tracking compared to static measurement-based methods. We further show that increasing the number of light sources improves spatial diversity, and that RIN has a more pronounced adverse effect on tracking accuracy than SDSN. Overall, this thesis provides a noise-aware framework that bridges traditional estimation with machine learning for robust VLC channel estimation and localization.

Table of Contents

List of Figures

Glossary

2D two dimensions 28, 29

2G second-generation 13

3D three dimensions 28, 29

6G sixth-generation 14

AoA angle-of-arrival 3, 29, 30, 82, 83

ARNNs Autoregressive neural networks 118

AWGN additive white Gaussian noise 3, 19

BCRLB bayesian cramér–Rao lower Bound 6, 7, 10, 31, 34, 46, 64, 65, 74–78, 80–82, 84, 87, 88, 95, 96, 106, 111, 113, 115, 117

BER bit error rate 23, 44

BFIM Bayesian Fisher information matrix 34, 96, 106

BLE blacktooth low energy 2

CC convolutional codes 17

CIR channel impulse response 29

CNN convolution neural network 27

CRF channel frequency response 48

CRLB Cramér-Rao Lower Bound 12, 31–36, 44, 45, 84, 94, 95, 98

CSK color shift keying 15, 18

CVNN complex-valued neural network 48

DD direct detection 16

DFIM distance Fisher information matrix 88, 90–94

DNN Deep learning neural network 48

DNNs deep neural networks 30

EKF Extended Kalman filter 4, 6–10, 39, 40, 46, 64, 65, 67, 71–73, 76–82, 84, 90, 97, 99, 100, 104–107, 111–113, 116, 117

ELMS extreme learning machines 30

EM electromagnetic 1

EMI ectromagnetic interference 3, 14

FFDNet flexible denoising convolutional neural network 48

FIM Fisher information matrix 88

FoV field of view 66, 86, 103

FPGA field- programmable gate array 83

FSK frequency shift keying 18

FSO free-space optical 14

GPS global positioning system 2

GUI graphical user interface 16

HCF hybrid coordination function 16

ID unique identifier 26

IM intensity modulation 16

IoT Internet of things 21

IPS indoor positioning systems 2, 3

IR infrared 13

JEITA Japan electronics and information technology industries association 14

KF Kalman filter 12, 29, 31, 37–39, 65

KNN k-nearest neighbors 29

LD laser diod 45, 46

LED light-emitting diode 3, 49–51, 65, 83, 84

LEDs light-emitting diodes 2, 14, 15, 21, 29, 30, 46, 82, 84

LiFi light fidelity 14

LMMSE least minimum mean square error 45, 51, 57

LoS line-of-sight 4, 44, 49, 113, 118

LS least squares 5, 31, 35, 36, 44, 45, 49, 51–53, 58–61, 70, 115, 116

m-MIMO massive MIMO (m-MIMO) 48, 51

MAP maximum a posteriori 45, 51

MIMO multiple-input multiple-output 48

MISO multiple-input single-output 7, 9, 81, 85, 102, 113, 117

MLE maximum likelihood estimation 5, 6, 9, 31, 35, 44, 45, 51, 57, 60, 64, 67–69, 71, 73, 76–80, 97, 98, 116

MLP multilayer perceptron 48, 58, 60, 116

MLPS multi-layer perceptions 6

MMSE minimum mean square error 45, 51, 57, 99

MPM mirror pulse modulation 18

MSE mean square error 6, 9, 10, 31, 45, 47, 51–56, 59–61, 69–71, 73, 101, 102, 115, 116

MUV Minimum Variance Unbiased 31, 32, 35

NLoS non-line-of-sight 49, 84, 113, 118

NLS nonlinear least squares 6, 9, 31, 36, 64, 67, 70, 71, 76–80, 116

NN Neural networks 49, 51, 55, 58, 59, 61, 115, 116

OBSS overlapping basic service sets 16

OCC optical camera communicationo 14, 15

OFDM orthogonal frequency division multiplexing 15

OOK On–Off keying 15, 18

OWC optical wireless communication 13, 14

PAM Pulse amplitude modulation 15

PD photodetector 6, 18–20, 23, 24, 29, 49, 50, 58, 65, 67, 76, 84–87, 89–93, 96, 97, 103, 104, 107–110

PDF probability density function 31, 68, 69

PDs photodetectors 3, 83

PEB Position error bound 96, 111

PF particle filter 4, 7, 8, 10, 105, 106, 113, 117

PFIM position Fisher information matrix 88, 93–95, 111

PSK phase shift keying 18

QSC quadrant solar cell 82

Rbf radial basis function 48

ResCBNet deep residual convolutional blind denoising network 48

RF radio frequency 1–4, 9, 12, 16, 18, 51

RFID radio frequency identification 2, 3

RIN Relative intensity noise vi, 3–5, 7, 10, 24, 25, 44–46, 81–84, 86, 88, 92, 102, 104, 111–113, 117, 119

RLL run-length limited 17

RLM recursive Levenberg–Marquard 7, 10, 105, 113, 117

RMS root-mean-square 82

RMSE root mean square error 77, 78

RNN recurrent neural networks 118

RRML ridge regression machine learning 82

RS Reed–Solomon 17

RSS received signal strength 2, 3, 26, 29, 30, 44, 65, 82–84

SDSN signal-dependent shot noise vi, 3, 5–7, 9, 10, 20–23, 44–51, 53, 58–61, 64–66, 69, 71, 75–78, 80–84, 86, 88, 102, 104, 111–113, 115–117, 119

SISO single-input single-output 44, 49, 58, 64, 65, 76, 80, 116

SNR signal-to-noise ratio 20, 23, 24, 44

TDM time-division multiplexing 26

TDoA dime Difference of arrival 27, 30, 82, 83

ToA time-of-arrival 3, 27, 28, 44, 82, 83

ToF time of flight 83

UV ultraviolet 13

UWB ultra-wideband 2

VLC visible light communication 1–9, 12, 14–23, 26, 27, 38, 40, 44, 46–49, 51, 52, 58, 61, 62, 64, 66, 81, 82, 84, 113, 116, 117

VLCC visible light communications consortium 15

VLP visible light positioning 3, 4, 6, 9, 12, 26, 27, 44, 46, 64, 65, 76, 82–85, 102, 104, 113

VLPC visible light positioning and communication 84

VPPM variable pulse position modulation 15, 18

VVLC vehicular visible light communication 48

WKNN weighted kNN 29

Chapter 1

Introduction

1.1 Background and Motivation

THE recent explosive growth in the number of devices connected to mobile networks, along with the accelerated development of online applications and services, has intensified the demand for widespread connectivity and high capacity. As a result, radio frequency (RF) communications are increasingly challenged in meeting these demands, and visible light communication (VLC) has been introduced as a complementary technology to help address them [6]. VLC exploits visible light for both illumination and data transmission. It utilizes the wide, untapped, free, and unlicensed electromagnetic (EM) spectrum from 375 nm to 782 nm [6].

VLC systems offer several fundamental advantages over RF-based systems. First, visible light does not interfere with RF signals, making it suitable for interference-sensitive environments such as hospitals, mines, and aircraft cabins [7]. Second, unlike RF signals that penetrate walls, visible light is spatially confined, providing enhanced physical-layer

security and reducing vulnerability to external eavesdropping [7]. Third, VLC benefits from the ubiquity of light-emitting diodes (LEDs), which have replaced traditional lamps in indoor illumination due to their energy efficiency, long operational lifetime, and environmental robustness. Importantly, LEDs support fast on–off modulation at rates imperceptible to the human eye, as standardized in IEEE 802.15.7 [8], enabling them to serve a dual role in both illumination and data communication at low additional cost. These features position VLC as a transformative technology capable of alleviating the spectrum scarcity crisis while simultaneously supporting high-speed data links and pervasive indoor connectivity.

Beyond communication, VLC has attracted significant attention for its potential in indoor localization and tracking. The ability to accurately determine the position and orientation of objects within indoor environments underpins a wide array of applications, including navigation in shopping malls and airports, asset tracking in smart factories, patient monitoring in healthcare facilities, augmented and virtual reality services, and emergency response in hazardous environments [9,10]. Unlike outdoor environments, where the global positioning system (GPS) provides reliable localization, indoor settings present unique challenges such as signal blockage, multipath propagation, and attenuation through walls, which render GPS ineffective. Consequently, a variety of indoor positioning systems (IPS) have been developed to fill this gap.

RF-based IPS technologies such as Wi-Fi, blacktooth low energy (BLE), ultra-wideband (UWB), and radio frequency identification (RFID) have been widely explored over the past two decades. Wi-Fi and BLE exploit received signal strength (RSS) indicators for location estimation, benefiting from the ubiquity of these technologies in consumer devices. However, RSS measurements are notoriously sensitive to multipath interference, shadowing, and environmental variability, which severely limit accuracy [11]. UWB systems provide supe-

rior accuracy at the centimeter level due to their wide bandwidth and precise time-of-flight measurements, yet their reliance on specialized and costly infrastructure hinders scalability to large deployments [12]. RFID-based solutions are effective in scenarios requiring tagged-object tracking but demand dense reader infrastructures, restricting their flexibility and applicability to broader indoor localization tasks [13]. Moreover, all RF-based IPS technologies are vulnerable to electromagnetic interference ectromagnetic interference (EMI), which poses a significant limitation in environments where many wireless devices coexist.

In contrast, visible light positioning (VLP), built on VLC principles, has emerged as an attractive alternative for indoor localization. VLP systems repurpose light-emitting diode (LED) luminaires as signal transmitters, exploiting their widespread deployment in illumination infrastructure. Position information can be derived from parameters such as RSS, time-of-arrival (ToA), angle-of-arrival (AoA) [14]. A key advantage of VLP lies in its cost-effectiveness: off-the-shelf photodetectors (PDs) or even smartphone cameras can be used as receivers without the need for specialized hardware. Furthermore, the propagation of visible light is more deterministic compared to RF, reducing the impact of multipath reflections and enhancing localization stability. Immunity to EMI, inherent spatial confinement for security, and dual-use with existing lighting systems make VLP particularly compelling for mission-critical applications such as hospitals, aircraft cabins, and industrial automation, where reliability and safety are paramount [15].

Despite these advantages, VLP is not without its challenges. The performance of VLP systems is strongly affected by noise in optical channels, particularly SDSN and RIN. Unlike conventional additive white Gaussian noise (AWGN), SDSN originates from the quantum nature of photon arrivals at the detector, which follow a Poisson process [16,17]. Since the variance of SDSN scales with the received optical power, noise levels dynamically change with user mobility, illumination variations, or LED dimming. This makes localization accu-

racy highly dependent on environmental conditions. Where, RIN arises from fluctuations in the intensity of light emitted by the light sources used in VLC systems. Its variance is directly proportional to the square of the transmission signal power. These variations, often due to the inherent properties of the light source or environmental factors, introduce additional noise into the communication channel [18], [19] In addition, real-world indoor environments present obstacles such as line-of-sight (LoS) dependence, signal blockage by objects or human bodies, and reflections from walls or furniture, which further complicate channel estimation [20]. These factors significantly degrade the reliability of both localization and tracking, highlighting the importance of robust estimation and tracking algorithms.

To overcome limitations in VLC and VLP, advanced estimation techniques are required, especially to address challenges arising from signal-dependent noise sources and imperfect hardware. Recursive estimators such as the Extended Kalman filter (EKF) and particle filter (PF) have shown potential for improving robustness under dynamic conditions by exploiting motion dynamics and feedback mechanisms. More recently, machine learning approaches have been explored to adaptively model non-linearities and capture complex noise distributions. However, the integration of these methods into VLP and VLC channel estimation systems remains an open research problem, particularly under such realistic impairments.

In summary, VLC and its extension to VLP provide a highly promising solution to the limitations of RF-based wireless communication and indoor localization systems. VLC exploits the vast unlicensed visible spectrum to deliver high-speed data, while VLP leverages the same infrastructure to enable accurate and secure indoor positioning . Nevertheless, the unique impairments of VLC systems, particularly signal-dependent noise and environmental uncertainties, pose significant challenges for reliable localization and tracking and

channel estimation. This thesis is motivated by the need to develop advanced frameworks for channel estimation, noise characterization, localization and tracking in VLC-based systems with the aim of bridging the gap between theoretical models and real-world indoor positioning applications.

1.2 Thesis Contributions

The main contributions of our work can be outlined as follows: This dissertation presents novel contributions to the channel estimation, localization, and tracking of VLC systems under progressively realistic noise conditions. The research advances in three stages: (*i*) channel estimation under SDSN, (*ii*) range estimation under SDSN noise, and (*iii*) localization and tracking of moving objects under the joint effect of SDSN and RIN.

1.2.1 Channel Estimation under Signal-Dependent Shot Noise

The first part of this dissertation addresses channel estimation in VLC systems in the presence of SDSN, which arises from the quantum nature of light and strongly impacts estimation accuracy. The main contributions are:

1. *Machine Learning-Based Estimator:* A lightweight shallow neural network (NN) estimator is proposed to enhance least squares (LS) and maximum likelihood estimation (MLE). By capturing the nonlinear effects of SDSN, the model effectively mitigates noise-induced errors and improves channel estimation accuracy.

2. *Polynomial Representation and Closed-Form MSE:* A polynomial representation of the trained network is derived, enabling analytical interpretation of its operation.

Additionally, we present a closed-form expression for the estimator's mean square error (MSE), providing theoretical benchmarks without extensive simulations.

3. *Computational Efficiency:* The proposed estimator achieves competitive accuracy compared to multi-layer perceptions (MLPS) while requiring significantly lower computational resources, making it suitable for real-time VLC estimation tasks.

1.2.2 Range Estimation under Signal-Dependent Shot Noise

The second part of this dissertation revisits range estimation between a transmitter and a photodetector (PD) receiver in the presence of SDSN. The contributions include:

1. *Estimation Framework:* We formulate the range estimation problem under SDSN, applying both recursive and non-recursive approaches for systematic evaluation.

2. *Non-Recursive Estimators:* MLE and nonlinear least squares (NLS) methods are implemented. For NLS, a closed-form MSE expression is derived using parameter transformation, providing theoretical accuracy benchmarks.

3. *Recursive Estimator:* The EKF is employed as a recursive estimator that integrates prediction and measurement updates. A detailed comparison with non-recursive techniques demonstrates the benefits of recursive filtering under SDSN noise.

4. *Impact of the Receiver Plane's Tilting Angle :* We investigate the effectiveness of the EKF in mitigating the impact of SDSN in VLP range estimation.

5. *Derive the bayesian cramér–Rao lower Bound (BCRLB):* We derive and analyze the BCRLB, providing insightful discussions on the impact of SDSN on the BCRLB.

1.2.3 Localization and Tracking of Moving Objects under SDSN and RIN

The final part of this dissertation extends the analysis to localization and tracking in VLC systems when both SDSN and RIN are present. The main contributions are:

1. *Systematic Study of joint SDSN and RIN:* We present the first systematic analysis of the combined effects of SDSN and RIN on VLC localization and tracking accuracy. The distinct and joint impacts of these noise sources are examined in detail.

2. *Closed-Form 2D-BCRLB Derivation:* A closed-form BCRLB is derived for VLC systems under both SDSN and RIN. This provides the fundamental theoretical benchmark for achievable accuracy in realistic conditions.

3. *EKF-Based Tracking of Moving Objects:* We implement an EKF framework to track a moving PD receiver under combined SDSN and RIN. To the best of our knowledge, this is the first application of EKF in this setting. Results confirm that EKF robustly balances prediction and noisy measurements, outperforming traditional estimators.

4. *Impact of Transmitter Density in multiple-input single-output (MISO)- VLC Systems:* The effect of increasing transmitter density in MISO VLC systems is investigated. Higher density improves measurement diversity and enhances localization accuracy, particularly in overlapping coverage regions.

5. *Comparison with Benchmark Estimation Techniques:* We compare the performance of our proposed position tracking and estimation approach with established techniques such as recursive Levenberg–Marquard (RLM) and PF. The results show that EKF outperforms RLM in terms of position error bounds and estimation reliability. While

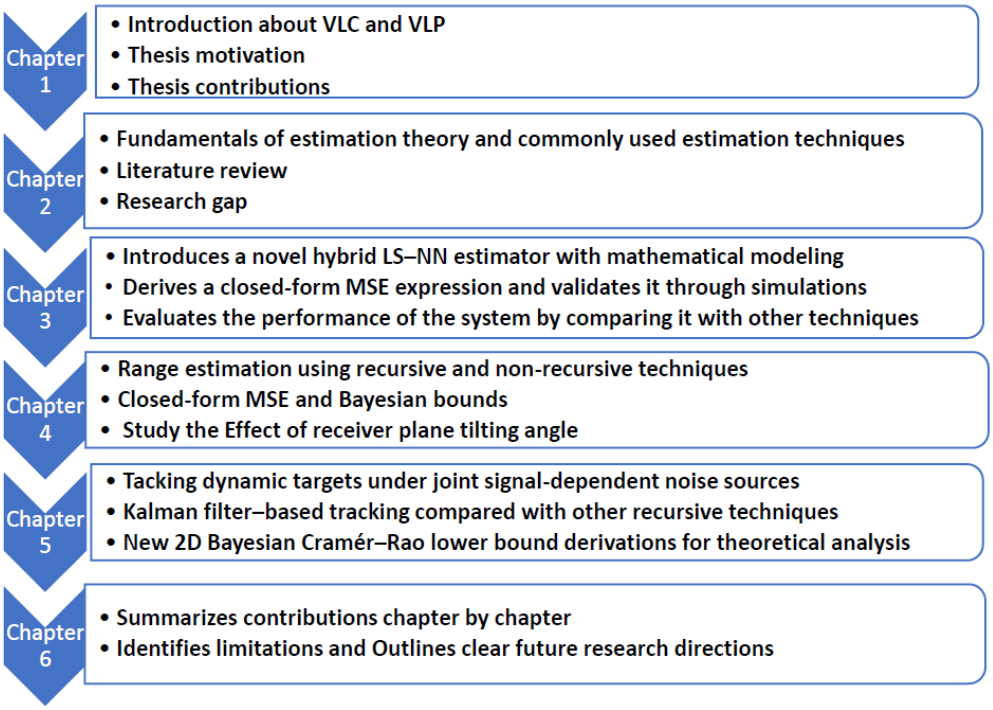

Figure 1.1: Summary of thesis outlines and contributions.

PF achieves performance close to EKF, EKF offers significantly lower computational complexity and is better suited for Gaussian noise models such as the one considered in our work.

Thesis Organization

This dissertation is organized into six chapters, each building upon the previous to develop a comprehensive framework for estimation, localization, and tracking in VLC systems under realistic noise conditions. A summary of the thesis organization and contributions can be

found in Fig. 1.1. The structure of the dissertation is detailed as follows:

- **Chapter 2** introduces the fundamentals of VLC systems and their application to indoor positioning. It then provides a broad overview of VLP techniques in comparison with traditional RF approaches. The main focus of this chapter is a literature review of prior studies on channel estimation and localization, with particular attention to works that analyze system performance under signal-dependent noise. This review highlights the challenges, limitations, and research gaps that motivate the contributions of this dissertation.

- **Chapter 3** presents a simple yet novel machine learning-based estimator to address the challenges posed by SDSN. A mathematical framework for the proposed estimator is developed, including a polynomial representation that enables closed-form computation of its MSE. The system model is introduced in this chapter, and the study is concluded with simulation results that validate the estimator's performance, followed by a critical discussion.

- **Chapter 4** introduces the proposed VLC-based range estimation framework. The system architecture, estimation techniques, evaluation benchmarks, and algorithmic designs are described in detail. Both recursive and non-recursive approaches are implemented, including MLE, NLS, and the EKF. A closed-form MSE expression for NLS is also derived, offering a theoretical reference for performance evaluation. This chapter begins with the system model and ends with simulation-based comparisons of the proposed techniques, accompanied by a comprehensive discussion of their relative performance.

- **Chapter 5** focuses on position estimation and tracking in indoor MISO-VLC systems with multiple light sources. An EKF is developed for real-time tracking and bench-

marked against alternative methods, including a geometric approach, RLM method, and PF. Results demonstrate that EKF achieves the lowest MSE, while PF offers comparable accuracy at a higher computational cost, and RLM and geometric methods show reduced robustness. The chapter also analyzes the impact of transmitter density, showing that increased light sources enhance spatial diversity and improve accuracy. The effects of SDSN and relative intensity noise RIN are further investigated, revealing that RIN degrades performance more severely than SDSN. Finally, the 2D-BCRLB is derived, providing a theoretical benchmark. The system model is detailed at the outset, and the chapter concludes with simulation results and a discussion synthesizing the effects of noise and transmitter density on localization accuracy.

- **Chapter 6** concludes the dissertation by consolidating the main findings and highlighting the key contributions of this research. This chapter outlines the limitations and future research directions, the chapter positions this work as a foundation for continued advancements in VLC-based localization and estimation.

1.3 List of Publications

1. S. H. ElFar, M. Yaseen and S. Ikki, "Insights into Visible Light Positioning: Range Tracking and Bayesian Cramér-Rao Lower Bound Analysis," *IEEE Communications Letters*, vol. 28, no. 9, pp. 2056-2060, Sept. 2024.

2. S. H. ElFar, M. Yaseen and S. Ikki, *"A Novel Machine Learning Algorithm for Channel Estimation in VLC Systems,"*, *IEEE Wireless Communications Letters*, vol. 14, no. 7, pp. 2084-2088, July 2025.

3. S. H. ElFar, M. Yaseen and S. Ikki, "Tracking and Positioning Dynamic Targets in VLC: Signal Dependent Noises and Bayesian Bound Analysis," in *IEEE Transactions on Communications*, accepted, 2025.

4. M. Yaseen, S. El-Far and S. Ikki, "Machine Learning-Based Channel Estimation in Visible Light Communication with Signal-Dependent Noise," *IEEE Middle East Conference on Communications and Networking* (MECOM), Abu Dhabi, United Arab Emirates, 2024, pp. 263-267.

5. *(Best Paper Award)* S. H. ElFar and S. Ikki, "An End-to-End Auto-Encoder Algorithm for Hardware-Impaired Transceivers Based on Meta and Joint Learning," *IEEE International Black Sea Conference on Communications and Networking* (BlackSeaCom), Istanbul, Turkey, 2023.

Chapter 2

Preliminaries and Literature Review

THIS chapter provides a general overview of the VLC system. In addition, it introduces the fundamentals of estimation theory and commonly used estimation techniques. Benchmark of estimation methods such as the Cramér-Rao Lower Bound (CRLB) and recursive estimation techniques like the Kalman filter (KF) are also discussed. In addition, we introduce VLP techniques, highlighting their unique characteristics, key differences, and the challenges faced in real-world applications. The chapter concludes with a literature review presented in the final subsection.

2.1 Wireless Communication Technologies

Currently, most existing wireless technologies rely on RF communication. However, there is growing consensus that the RF spectrum alone will not be sufficient to meet future connectivity demands, primarily due to overcrowding and rising costs associated with RF spectrum usage [21]. In contrast, the optical spectrum remains largely untapped, unregu-

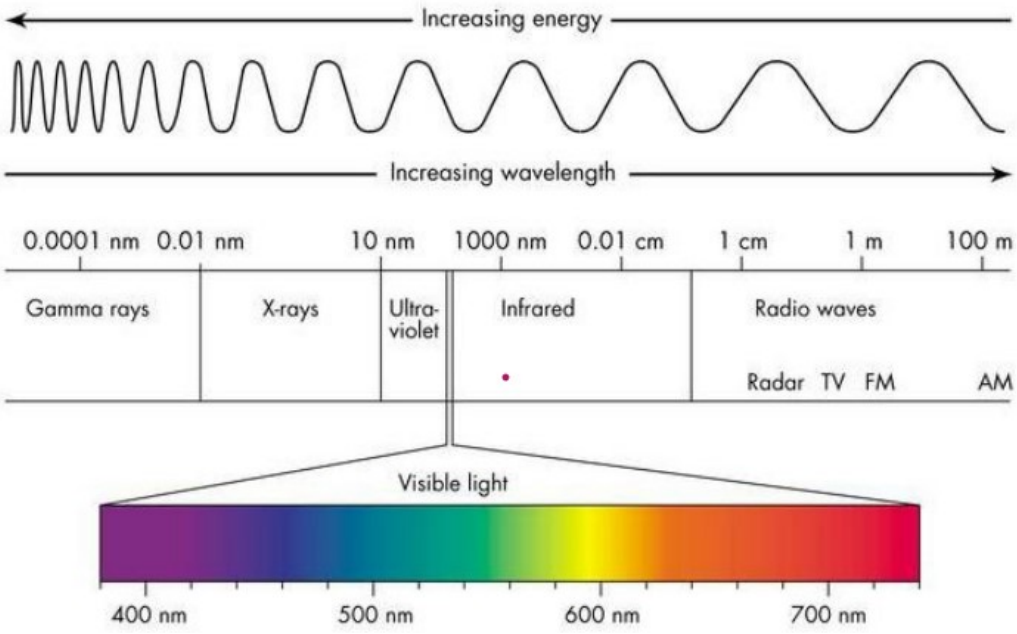

Figure 2.1: The electromagnetic spectrum [1].

lated, and abundantly available. As illustrated in Fig. 2.1, the optical spectrum comprises infrared (IR), visible light, ultraviolet (UV), X-rays, and gamma rays. Optical fiber communication already exploits this spectrum to deliver high data rates. Consequently, for last-mile connectivity and mobile access, it is a natural progression to extend the use of optical signals from guided media (fiber optics) to free-space optical communication [22], [1].

This shift has gained significant interest in optical wireless communication (OWC) technologies from both academia and industry. Historically, OWC using IR was employed in second-generation (2G) mobile devices to provide short-range, high-speed digital communication [23]. Looking ahead, OWC is anticipated to play a key role in supporting the goals

and requirements of sixth-generation (6G) communication systems [24]. OWC includes a variety of technologies that can address diverse application scenarios. These include VLC, free-space optical (FSO) communication, light fidelity (LiFi), and optical camera communicationo (OCC) also known as image-sensor-based communication [23].

2.2 Visible Light Communication Origins and Standardization

VLC has a long and interesting history, beginning in the 1880s, when Alexander Graham Bell developed the *photophone*, an early device that used modulated sunlight to transmit speech wirelessly for several hundred meters [25]. Coincidentally, this invention predates the emergence of radio-based speech transmission. The modern concept of VLC re-emerged in 1998 with the commercialization of white-light LEDs [26]. Later on, researchers demonstrated the use of white LEDs to transmit audio signals wirelessly, marking one of the earliest practical implementations of contemporary VLC [26]. Research in VLC has accelerated due to its numerous advantages, including high achievable data rates, low deployment costs, scalability, and immunity to electromagnetic interference (EMI). As can be seen in Fig. 2.1, the visible light spectrum ranges from approximately 380 to 750 nanometers, equivalent to frequencies between 430 and 790 Terahertz (THz). Radio waves, however, have a broader range, from 1 millimetre to 100 kilometres, covering frequencies between 3 kHz to 300 GHz [27].

Global standardization efforts have played a crucial role in the development of VLC technologies. Initial proposals were made in Japan: in 2007, Japan electronics and information technology industries association (JEITA) introduced a *Visible Light ID System*,

followed by the visible light communications consortium (VLCC) in 2008, which published its own specification. However, these early standards lacked essential features such as flicker mitigation and dimming support [8]. The initial international full-comprehensive VLC standard was published by the *IEEE* 802.15 Working Group in 2011 under the title *IEEE* 802.15.7. This standard defines three physical (PHY) layers to accommodate different application scenarios as follows [8]:

- *PHY I:* Designed for outdoor applications, offering data rates from 11.67 to 266.6 kbps using On–Off keying (OOK) and variable pulse position modulation (VPPM).
- *PHY II:* Designed for indoor environments, providing support for data rates from 1.25 to 96 Mbps.
- *PHY III:* Optimized for high-speed communication based on multi-color LEDs and color shift keying (CSK) to meet data rate requirements from 12 Mbps to 96 Mbps.

To address emerging applications and limitations of *IEEE* 802.15.7, two extensions were proposed as follows

- *IEEE* 802.15.7m (2018): Focuses on OCC using LED transmitters and camera-based receivers. This standard is particularly useful for applications like indoor navigation and augmented reality.
- *IEEE* 802.15.13 (2023): Targets high-speed, high-reliability industrial applications. It supports data rates up to 2.91 Gbps using advanced modulation schemes such as Pulse amplitude modulation (PAM) and orthogonal frequency division multiplexing (OFDM).

Simultaneously, the *IEEE* 802.11 Working Group, responsible for Wi-Fi standards, initiated efforts in 2018 to integrate VLC into existing wireless networks. This led to the development of *IEEE* 802.11bb, which enables VLC operation in the 380–1000 nm wavelength range, encompassing visible and near-infrared light. The standard builds on existing MAC layer functionality, with enhancements for hybrid coordination function (HCF), coexistence with overlapping basic service sets (OBSS), and advanced power management. *IEEE* 802.11bb mandates a minimum throughput of 10 Mbps and ensures interoperability with existing Wi-Fi infrastructure [28]. To facilitate standardized evaluation, *IEEE* 802.11bb introduced reference channel models based on accelerated ray tracing simulations. These models were validated through experimentation and made publicly available along with a MATLAB® graphical user interface (GUI), facilitating collaborative research and development. The comparison between the key *IEEE* VLC-related standards can be found in Table 2.1. This table highlights the major differences in publication dates, targeted use cases, achievable data rates, and modulation techniques [28]. These standards collectively provide a comprehensive foundation for future VLC applications across consumer, industrial, and hybrid wireless networks, offering new possibilities for secure, high-speed communication.

2.2.1 The Physical Layer in Visible Light Communication

The physical layer in VLC systems differs significantly from that of conventional RF communication systems. VLC employs intensity modulation (IM) with direct detection (DD), which requires the transmitted signal to be both real-valued and positive (unipolar) [29]. As a result, standard RF modulation schemes, typically bipolar and complex-valued, must be adapted to meet VLC's unipolar signal constraints [26]. The unique characteristics of

Table 2.1: Comparison of Key VLC Standards

Standard	**Published**	**Primary Use Case**	**Data Rate**	**Modulation Techniques**
IEEE 802.15.7	2011	Indoor/outdoor VLC, smart lighting	11.67 kbps to 96 Mbps	OOK, VPPM, CSK
IEEE 802.15.7m	2018	Optical Camera Communication (OCC)	from kbps to few Mbps	Intensity modulation with camera reception
IEEE 802.15.13	2023	High-speed industrial VLC	Up to 2.19 Gbps	PAM, OFDM, advanced modulation
IEEE 802.11bb	2023	Wi-Fi-compatible VLC	$\geq$10 Mbps to 10 Gbps	CSK, OFDM, MAC-layer optimized

visible light, such as its propagation behavior and susceptibility to various types of noise, influence key aspects of the VLC system. These include path loss, channel modeling, noise sources, modulation techniques, and coding strategies.

Fig. 2.2 shows the physical layer block diagram of the *IEEE* VLC model. At the transmitter, the input bitstream is channel-encoded with redundancy (e.g., parity bits) to support error correction against path loss and optical noise. Forward Error Correction (FEC) codes such as Reed–Solomon (RS) and convolutional codes (CC) are commonly used, depending on environmental conditions like indoor/outdoor settings, data rate requirements, and frame length [30]. To prevent flickering caused by long sequences of 1s or 0s (which result in DC imbalance), the output of the channel encoder is passed through a run-length limited (RLL) line encoder. This ensures DC balance and supports clock recovery by maintaining a more uniform distribution of 1s and 0s.

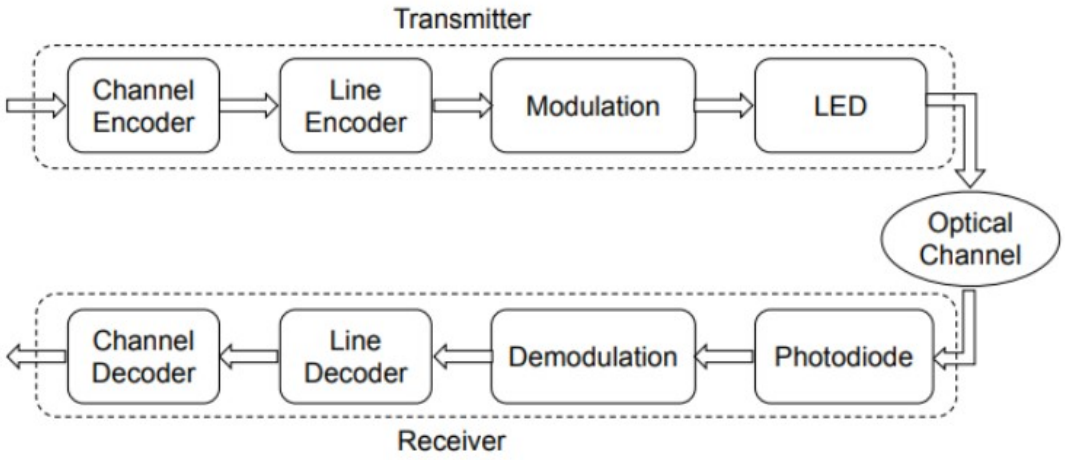

Figure 2.2: IEEE general model for VLC physical layer [2].

After line encoding, modulation is performed. Unlike RF systems, where signals are typically bipolar and may carry phase information, VLC receivers, based on PDs, are sensitive only to signal amplitude. Therefore, the modulated signals must be converted to real and positive values. This is achieved by adding a DC bias to shift the signal into the unipolar range, and by ensuring all subcarriers are modulated at frequencies above the flicker fusion threshold to remain imperceptible to the human eye [30]. The *IEEE* VLC standard supports a range of modulation schemes suited for different applications. These include OOK, VPPM, CSK, mirror pulse modulation (MPM), frequency shift keying (FSK), and phase shift keying (PSK) mong these OOK is the simplest, where logical bits are represented by switching the LED on or off, where '1' corresponds to high-intensity light, and '0' to low-intensity light [2].

2.3 Noise in Visible Light Communication System

Noise is a fundamental limiting factor in the performance of VLC networks. It can substantially degrade the efficiency, accuracy, and reliability of these systems by interfering with signal detection, reducing data integrity, and increasing the probability of transmission errors. The impact of noise is particularly pronounced in environments with fluctuating illumination levels, where a combination of internal and external noise sources can affect signal quality [24]. In VLC systems, noise sources are generally classified into two main categories: *independent noise* and *dependent noise*, based on whether the noise characteristics vary with the transmitted optical signal [24].

Independent Noise: Independent noise encompasses all types of noise whose magnitude and statistical properties remain unaffected by the signal level. Common contributors to this category include ambient light interference, such as sunlight or illumination from LED sources, dark current noise inherent to PDs, and thermal noise arising due to the intrinsic properties of electronic components [31]. Among these, thermal noise, also referred to as Johnson-Nyquist noise, is often the most dominant. It is generated by the random motion of electrons in a conductor due to temperature and is present regardless of signal presence. This type of noise is typically modeled as AWGN and is mathematically described as: [20]

$$n \sim \mathcal{N}(0, \sigma_n^2), \tag{2.1}$$

where σ_n^2 denotes the variance of the noise. Since it is spectrally flat and statistically independent of the signal, its impact on system design can be estimated and mitigated through filtering and circuit optimization.

Dependent Noise: Dependent noise, in contrast, is intrinsically linked to the magnitude of the input signal. Its intensity fluctuates proportionally with the signal strength, making it significantly more complex to model and manage. This type of noise is especially challenging in applications that require high dynamic range or operate in low signal-to-noise ratio (SNR) conditions. One of the most critical sources of dependent noise in VLC systems is SDSN, which originates from the quantum nature of light and the random arrival of photons at the PD. As optical power increases, the mean arrival rate of photons increases, but so does the variance in the number of photons detected, leading to fluctuations that manifest as noise. This dependence makes SDSN a fundamental performance limiter, particularly in scenarios involving high-speed data transmission or weak optical signals.

Because of its impact on signal fidelity, SDSN requires careful modeling and mitigation. Strategies include adaptive signal processing, threshold optimization, and hardware-level enhancements. Given its importance in practical VLC system design, SDSN is explored in greater depth in the following subsections.

2.3.1 Background and Origin of Shot Noise

Shot noise, also known as Poisson noise or quantum noise, arises due to the discrete and random nature of particle flow, such as electrons or photons, within physical systems. It was first introduced by Walter Schottky in 1918 while studying vacuum tubes. Schottky observed that the electrical current was not continuous, but rather fluctuated due to the individual arrival of electrons in packets or "shots". These fluctuations could not be explained using classical physics alone. His observations were later supported by John B. Johnson and Harry Nyquist, who identified similar behavior in other electronic systems.

Shot noise has since become an important concept in the fields of quantum mechanics, solid-state physics, semiconductor devices, and optical communications. Its applications span from studying the behavior of quantum systems to evaluating performance in communication channels. One notable application is VLC systems, where shot noise plays a major role in limiting the receiver sensitivity and defining system performance [32]. The magnitude of shot noise is signal-dependent and increases with the square root of the average current or light intensity. It is particularly significant in low-light conditions or high-speed applications, where precise detection of photons is required. Shot noise is a fundamental noise limit and is independent of temperature, making it distinct from thermal noise. It also arises in non-electronic domains, such as photon emission, granular flow, and even biological processes.

Furthermore, SDSN is more dominant in systems where the signal power is low and the signal is comprised of discrete particle arrivals, which is often the case in VLC systems operating in indoor environments with reflections and varying illumination levels. The importance of understanding shot noise in these systems is heightened as the performance of modern VLC systems relies heavily on precise signal interpretation. Finally, in practical VLC deployments, ambient light sources such as sunlight or artificial LEDs can cause unpredictable changes in the photon arrival rate, which increases the randomness in the received signal and exacerbates shot noise effects. Therefore, even though VLC offers high data rates and secure transmission, its performance can be significantly constrained by noise sources like SDSN. System designers must take this into account when designing receivers and signal processing algorithms, especially for applications such as indoor localization, motion tracking, and Internet of things (IoT) connectivity [32].

2.3.2 Mathematical Modeling of Signal-Dependent Shot Noise

SDSN is mathematically modeled using a Poisson process. In this process, the events (e.g., electron or photon arrivals) occur randomly, independently, and with a constant average rate. The key property of the Poisson process is that the mean and variance are equal. This randomness translates to variations in the received signal, impacting system performance. The probability of observing k arrivals in time t is given by the Poisson distribution:

$$\Pr(N = k) = \frac{(\lambda t)^k e^{-\lambda t}}{k!}, \tag{2.2}$$

where λ is the expected number of arrivals per unit time. This expression shows the discrete nature of shot noise, with $\mathbb{E}[N] = \mathrm{Var}[N] = \lambda t$, where $\mathbb{E}[.]$ and $\mathrm{Var}[.]$ are the expectation and variance operators, respectively.

In terms of current, the root mean square value of shot noise is given by:

$$I_{\mathrm{sh}} = \sqrt{2qIf}, \tag{2.3}$$

where q is the electron charge (C), I is the average photocurrent (A), and f is the system bandwidth (Hz). This relationship highlights that the shot noise increases with the square root of the signal. When the number of events is large (as in VLC systems), the Poisson distribution can be approximated by a Gaussian distribution due to the Central Limit Theorem. Thus, the SDSN can be represented as a Gaussian distribution:

$$\mathrm{SDSN} \sim \mathcal{N}(0, \sigma_{\mathrm{ds}}^2), \tag{2.4}$$

where the variance σ_{ds}^2 is defined as:

$$\sigma_{\text{ds}}^2 = \zeta^2 \sigma^2, \quad \text{with} \quad \zeta^2 = \frac{\sigma_{\text{ds}}^2}{\sigma_n^2}, \tag{2.5}$$

This expression illustrates how the signal-dependent component scales with the signal variance. The Gaussian approximation simplifies the modeling and enables the use of signal processing tools that assume normality. To better understand the nature of SDSN, one can also consider practical analogies. For instance, if one imagines an hourglass where grains of sand fall randomly through the neck, the arrival time of each grain is unpredictable. This randomness closely resembles the arrival of photons or electrons at a detector in a VLC system. While the average rate of arrival may be constant, the fluctuations from moment to moment generate noise [33].

In VLC systems, SDSN significantly affects overall system design and performance. One of the most critical issues introduced by SDSN is the reduction in the SNR. The random nature of SDSN causes fluctuations in the detected signal, which lowers the clarity and reliability of the transmission. As a result, bit error rate (BER) tends to increase, particularly in low-light or high-speed communication scenarios where tolerance for noise is minimal [34]. The SDSN also imposes a fundamental constraint on the minimum detectable power of the receiver. Because the magnitude of shot noise increases with the signal intensity, VLC systems must strike a balance between increasing throughput and minimizing the noise floor. Additionally, components such as optical transmitters, amplifier circuits, and PDs contribute to the total noise within the system, and their influence can exacerbate the effects of SDSN. These cumulative noise contributions complicate the development of reliable VLC protocols and demand robust design strategies [35].

2.3.3 Background and Origin of Relative Intensity Noise

In semiconductor lasers, the optical output power is not perfectly stable but instead exhibits random fluctuations over time. These fluctuations are collectively referred to as RIN. Hence RIN is defined as the ratio of the mean-square fluctuation in the laser output power to the square of the average output power. It is one of the key noise sources that directly impacts the SNR in optical communication systems, especially those using intensity modulation formats. In practice, RIN degrades the achievable system sensitivity and limits transmission performance. The dominant source of RIN in semiconductor lasers is spontaneous emission. When a laser operates above its threshold, most photons are generated by stimulated emission, which produces coherent photons with identical phase, direction, and frequency. However, a small fraction of photons always originates from spontaneous emission. These photons have random properties (wavelength, phase, polarization, and direction) and, when coupled into the lasing mode, interfere with the stimulated photons. This interference leads to random fluctuations in the output intensity.

At the receiver side, in a direct-detection system, the PD current is proportional to the square of the incident optical field. Consequently, the coexistence of stimulated and spontaneous emission produces a beat signal, where optical frequency components interfere with one another. This beating process manifests as electrical noise at the output of the detector, as illustrated in Fig. 2.3. Thus, RIN effectively characterizes the contribution of laser intensity fluctuations to the detected electrical noise relative to the average signal power.

Formally, RIN is expressed in terms of the power spectral density (PSD) of the intensity noise as

$$\mathrm{RIN}(\omega) = \frac{S_P(\omega)}{P_{\mathrm{opt}}^2}, \tag{2.6}$$

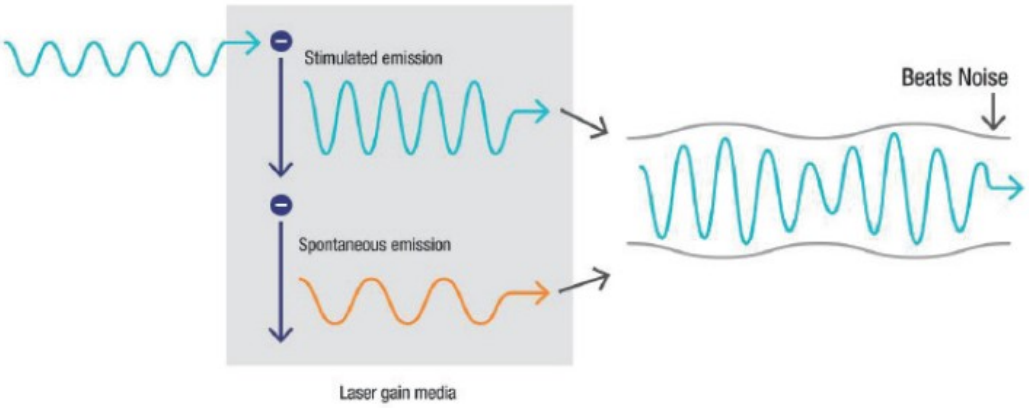

Figure 2.3: Illustration of laser intensity noise as an interference (beat) between stimulated and spontaneous emissions. [3].

where $S_P(\omega)$ denotes the PSD of the power fluctuations at angular frequency ω, and P_{opt} represents the average optical output power. RIN is therefore a normalized quantity and is typically expressed in units of Hz^{-1} or dB/Hz [3]. Alternatively, in time-domain representation, RIN may be written as

$$\text{RIN} = \frac{\langle \Delta P^2 \rangle}{\langle P_0 \rangle^2}, \tag{2.7}$$

where $\langle \Delta P^2 \rangle$ is the mean-square fluctuation of the optical power, and $\langle P_0 \rangle$ is the average optical power. Figure 2.4 contrasts the ideal and practical cases of laser output intensity. In the ideal case, when the laser is biased with a stable DC current and all external factors (temperature, reflections, etc.) are constant, the output power remains fixed. In reality, the output exhibits random fluctuations due to RIN, resulting in noisy deviations around the mean value.

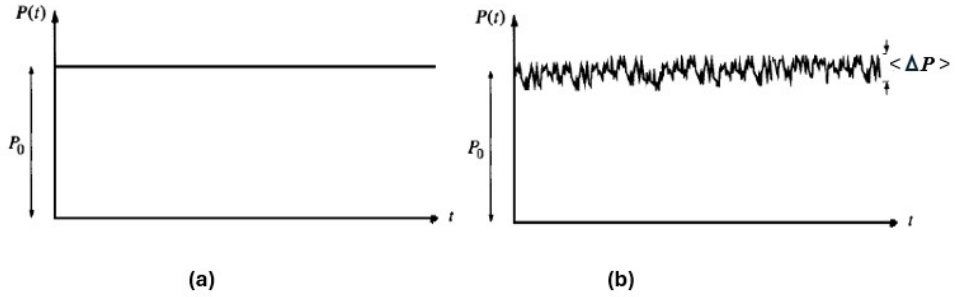

Figure 2.4: (a) Ideal laser output with constant DC bias. (b) Practical laser output showing random fluctuations due to RIN [4].

2.4 Visible Light Positioning Algorithms

VLP algorithms play a central role in determining the position of a receiver in indoor VLC systems. These algorithms leverage different properties of light propagation and signal characteristics to infer spatial location. VLP algorithms can be broadly categorized into classes as shown in Fig. 2.5. In the following subsections, each technique is briefly described.

2.4.1 Proximity-Based Positioning

Proximity is the simplest form of VLP. The receiver estimates its position by identifying the closest visible LED transmitter, which continuously broadcasts a unique identifier (ID). The receiver matches the ID to a known location stored in a database. In environments with overlapping signals, the receiver typically selects the transmitter with the highest received signal strength RSS. Although this method offers limited accuracy, it is low-cost and easy to implement. Enhancements such as time-division multiplexing (TDM) and camera-based LED-ID detection can help resolve conflicts in multi-signal environments [10].

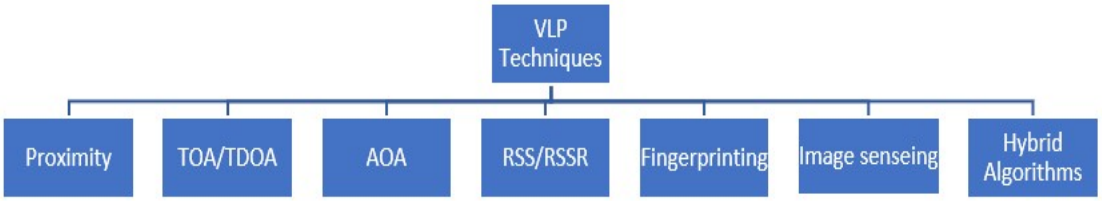

Figure 2.5: Key visible light positioning (VLP) algorithms.

2.4.2 Time of Arrival and Time Difference of Arrival

ToA and dime Difference of arrival (TDoA) methods determine location based on the propagation time of optical signals. ToA calculates absolute signal travel time, while TDoA uses the difference in arrival times between multiple transmitters. These techniques can achieve high positioning accuracy but require nanosecond-level synchronization and high-speed ADCs. Advanced solutions include convolution neural network (CNN)-based phase difference estimation and particle filtering to improve resilience against synchronization errors and multipath effects. However, their adoption in VLC systems is limited due to hardware complexity [10].

ToA-Based Trilateration

Trilateration is a fundamental geometric technique used in ToA-based positioning systems. In a VLP context, the receiver's position is estimated by calculating its distances from multiple known LED transmitters based on the signal's time of arrival. Assuming the coordinates of the receiver are denoted by (x, y, z) and the coordinates of n LED transmitters are given by (x_i, y_i, z_i) for $i = 1, 2, ..., n$, the time it takes for the signal to travel from the i-th transmitter to the receiver is τ_i. Since light travels at a constant speed c, the

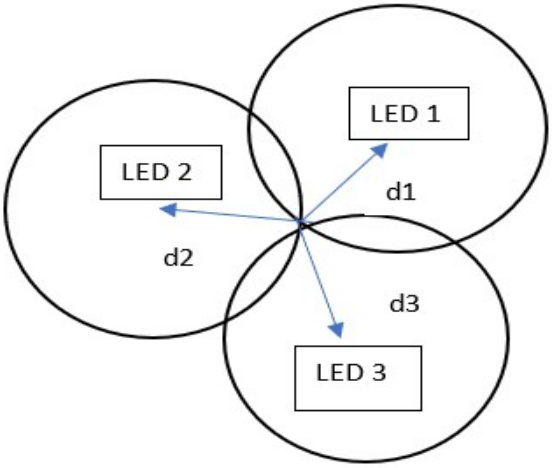

Figure 2.6: Illustration of trilateration technique in 2D space.

distance between the transmitter and receiver can be modeled as:

$$d_i = \sqrt{(x - x_i)^2 + (y - y_i)^2 + (z - z_i)^2} = c \cdot \tau_i. \tag{2.8}$$

This equation forms the basis of the trilateration method. In a two dimensions (2D) environment, each distance measurement describes a circle centered at the respective LED transmitter. The intersection point of at least three such circles corresponds to the receiver's estimated location as shown in Fig. 2.6. Similarly, in three dimensions (3D) space, each distance measurement forms a sphere, and the intersection of at least four spheres is used to localize the receiver.

This method requires high precision in measuring the arrival time τ_i for each signal. Any error in time synchronization or environmental interference can significantly affect the accuracy of the distance estimation and, consequently, the position calculation. Therefore, ToA-based trilateration methods are highly sensitive to time resolution and are often supported by signal processing techniques or hybrid methods to improve robustness.

2.4.3 Angle of Arrival

AoA techniques estimate the receiver's location by analyzing the angles at which signals arrive from different transmitters. Using geometric triangulation, the receiver's position is obtained from the intersection of angle vectors. A minimum of two LEDs is required for 2D localization and three for 3D. AoA methods can achieve high accuracy but are sensitive to device orientation and alignment. To address this, specialized detectors such as quadrant PDs and complementary PDs have been developed [31].

2.4.4 Received Signal Strength and Relative Received Signal Strength

RSS-based positioning estimates distance based on signal attenuation over space, often modeled using the Lambertian radiation model. It is one of the most widely used techniques due to its simplicity and low hardware requirements. However, RSS-based methods are highly sensitive to environmental changes, noise, and reflections. Signal filtering techniques (e.g., KF, particle filters) and machine learning-based models have been proposed to improve robustness and accuracy.

2.4.5 Fingerprinting

Fingerprinting is a data-driven localization technique that consists of two phases: offline and online. In the offline phase, a database of signal characteristics (e.g., RSS vectors, channel impulse response (CIR), extinction ratios) is collected at known locations. In the online phase, the receiver's current signal measurement is compared with the database to estimate its location. Matching methods include k-nearest neighbors (KNN), weighted kNN (WKNN), Bayesian inference, and machine learning algorithms such as random forests,

extreme learning machines (ELMS), and deep neural networks (DNNs). Fingerprinting provides high accuracy in complex indoor environments but requires significant calibration and is sensitive to environmental dynamics [36].

2.4.6 Image Sensing

Image sensing techniques use camera-equipped devices to capture visual information from LEDs. Features such as light intensity distributions, LED IDs, or geometric arrangements are extracted from images and used to estimate position. This method can achieve very high positioning accuracy, often in the centimeter range. However, it is sensitive to ambient lighting, motion blur, and processing latency. Algorithms like Light Print and Fisher discriminant analysis have been proposed to enhance performance in such scenarios [36].

2.4.7 Hybrid Algorithms

Hybrid approaches combine two or more of the aforementioned techniques to improve localization performance. For instance, combining RSS with AoA mitigates the limitations of each individual method. Other examples include TDoA-fingerprinting fusion and image-RSS integration. Although hybrid methods can significantly improve accuracy and robustness, they typically require more complex system design and computational resources.

2.5 Introduction to Estimation Theory

This section presents the foundational theoretical concepts used in this work, with a focus on estimating unknown deterministic parameters from noisy measurements, a central

theme in classical estimation theory. We provide an overview of the MLE, LS, NLS, and KF estimators, and discuss the benchmark performance limits defined by the CRLB and BCRLB.

2.5.1 The Mathematical Estimation Problem

Let $\mathbf{x}$ denote an observation vector of length L. The estimation of an unknown parameter β is feasible only if the data $\mathbf{x}$ depend on β. In practice, the data are modeled as random, described by probability density function (PDF) that itself is a function of β. The stronger the dependence of the PDF on β, the more accurately the parameter can be estimated. Conversely, if the PDF has little or no sensitivity to β, accurate estimation becomes unlikely [37]. In classical estimation theory, β is considered a deterministic but unknown quantity. In contrast, Bayesian estimation treats β as a random variable. Regardless of the approach, the estimator is a random variable whose performance is best characterized through its statistical properties.

Because classical estimation strives to identify optimal or near-optimal estimators for unknown deterministic parameters, various optimality criteria have been introduced. The MSE is one natural metric, measuring the average squared deviation between the estimator and the true value. However, MSE typically involves the bias of the estimator, and minimizing it directly can lead to impractical solutions. Hence, a common strategy is to first enforce zero bias and then seek an estimator that minimizes the variance, known as the Minimum Variance Unbiased (MUV) estimator [37].

2.5.2 Cramér-Rao Lower Bound

The CRLB provides a lower limit on the variance of any unbiased estimator, serving as a fundamental benchmark in estimation theory. It sets a standard against which the performance of any unbiased estimator can be compared. If an estimator reaches this bound for all values of the unknown parameter, it is deemed the MUV estimator.

For a scalar parameter β, the CRLB is expressed as:

$$\text{var}(\hat{\beta}) \geq \text{CRLB}(\beta) = \frac{1}{J(\beta)}, \tag{2.9}$$

provided that the regularity condition

$$\mathbb{E}\left\{\frac{\partial \ln p(\mathbf{x}, \beta)}{\partial \beta}\right\} = 0, \quad \forall \beta, \tag{2.10}$$

is satisfied, where the derivative is evaluated at the true value of β. Here, $J(\beta)$ is the Fisher information, given as:

$$J(\beta) = -\mathbb{E}\left\{\frac{\partial^2 \ln p(\mathbf{x}, \beta)}{\partial \beta^2}\right\}. \tag{2.11}$$

Transformation of Parameters: When the parameter of interest is a function of another variable (e.g., $\beta = g(\mu)$), the CRLB for μ can be derived from that of β as:

$$J(\mu) = \left(\frac{\partial \beta}{\partial \mu}\right)^2 J(\beta). \tag{2.12}$$

Extension to Vector Parameters: For a vector parameter $\boldsymbol{\beta} = [\beta_1, \beta_2 \ldots, \beta_p]^{\mathrm{T}}$, the

Fisher Information Matrix (FIM) is a $p \times p$ matrix with elements defined by:

$$[\mathbf{J}(\boldsymbol{\beta})]_{ij} = -\mathbb{E}\left\{\frac{\partial^2 \ln p(\mathbf{x};\boldsymbol{\beta})}{\partial\beta_i \partial\beta_j}\right\}. \tag{2.13}$$

The CRLB for β_i is then given by

$$\text{CRLB}(\beta_9) = [\mathbf{J}(\boldsymbol{\beta})]^{-1}_{i,i}. \tag{2.14}$$

Furthermore, if $\boldsymbol{\beta} = \mathbf{g}(\mu)$, where μ is an r-dimensional parameter, their FIMs relate via the Jacobian matrix $\mathbf{T} \in \mathbb{R}^{r\times p}$:

$$\mathbf{J}(\mu) = \mathbf{T}\mathbf{J}(\boldsymbol{\beta})\mathbf{T}^{\mathrm{T}}, \tag{2.15}$$

with

$$\mathbf{T} = \frac{\partial \boldsymbol{\beta}^{\mathrm{T}}}{\partial \mu} = \begin{bmatrix} \frac{\partial\beta_1}{\partial\mu_1} & \frac{\partial\beta_2}{\partial\mu_1} & \cdots & \frac{\partial\beta_p}{\partial\mu_1} \\ \frac{\partial\beta_1}{\partial\mu_2} & \frac{\partial\beta_2}{\partial\mu_2} & \cdots & \frac{\partial\beta_p}{\partial\mu_2} \\ \vdots & \vdots & \ddots & \vdots \\ \frac{\partial\beta_1}{\partial\mu_r} & \frac{\partial\beta_2}{\partial\mu_r} & \cdots & \frac{\partial\beta_p}{\partial\mu_r} \end{bmatrix}. \tag{2.16}$$

For Gaussian observations where $\mathbf{x} \sim \mathcal{CN}\left(\varphi(\boldsymbol{\beta}), \mathbf{C}(\boldsymbol{\beta})\right)$ implying that both the mean and covariance depend on $\boldsymbol{\beta}$, FIM can be computed as [37]:

$$[\mathbf{J}(\boldsymbol{\beta})]_{ij} = \Re\left\{\left[\frac{\partial\varphi(\boldsymbol{\beta})}{\partial\beta_i}\right]^{\mathrm{H}} \mathbf{C}^{-1}(\boldsymbol{\beta})\left[\frac{\partial\varphi(\boldsymbol{\beta})}{\partial\beta_j}\right]\right\} + \text{tr}\left[\mathbf{C}^{-1}(\boldsymbol{\beta})\frac{\partial\mathbf{C}(\boldsymbol{\beta})}{\partial\beta_i}\mathbf{C}^{-1}(\boldsymbol{\beta})\frac{\partial\mathbf{C}(\boldsymbol{\beta})}{\partial\beta_j}\right]. \tag{2.17}$$

The corresponding derivatives are defined for the mean and covariance functions.

2.5.3 Bayesian Cramér–Rao Lower Bound (BCRLB)

The BCRLB extends the classical CRLB to dynamic systems where prior knowledge about parameter evolution is available. It incorporates both measurement information and prior information, making it suitable for recursive estimation and tracking [38], [39].

Scalar parameter: For a scalar parameter β_t evolving in time, the Bayesian Fisher information is given as

$$J^{(B)}(\beta_t) \;=\; J^{(O)}(\beta_t) + J^{(I)}(\beta_t), \tag{2.18}$$

where $J^{(O)}$ comes from the measurement model and $J^{(I)}$ comes from the prior (dynamic) model. The BCRLB states that

$$\mathrm{var}(\hat{\beta}_t) \;\geq\; \left(J^{(B)}(\beta_t)\right)^{-1}. \tag{2.19}$$

Vector parameter: For a vector parameter $\boldsymbol{\beta}_t \in \mathbb{R}^p$, the Bayesian Fisher information matrix (BFIM) is

$$\mathbf{J}^{(B)}(\boldsymbol{\beta}_t) \;=\; \mathbf{J}^{(O)}(\boldsymbol{\beta}_t) + \mathbf{J}^{(I)}(\boldsymbol{\beta}_t), \tag{2.20}$$

Recursive form: The BFIM evolves recursively as

$$\mathbf{J}^{(B)}[t] \;=\; \mathbf{J}^{(O)}[t] + \mathbf{G}_{22}[t] - \mathbf{G}_{21}[t]\left(\mathbf{J}^{(B)}[t-1] + \mathbf{G}_{11}[t]\right)^{-1}\mathbf{G}_{12}[t]. \tag{2.21}$$

Definition of $\mathbf{G}_{ij}[t]$: The $\mathbf{G}_{ij}[t]$ blocks are defined as

$$\mathbf{G}_{ij}[t] \;=\; \mathbb{E}\Bigg[-\frac{\partial^2 \log p(\boldsymbol{\beta}[t] \mid \boldsymbol{\beta}[t-1])}{\partial \boldsymbol{\beta}[t+i-2]\, \partial \boldsymbol{\beta}[t+j-2]^{\mathrm{T}}}\Bigg], \qquad i,j \in \{1,2\}. \tag{2.22}$$

2.5.4 Maximum Likelihood Estimator

Since a MUV estimator is not always available, alternative estimation techniques become necessary. The MLE approach is widely adopted due to its practical advantages in complex estimation problems. It is well-known that the MLE estimator is asymptotically optimal, becoming unbiased and efficient (i.e., attaining the CRLB) as the number of observations increases.

For a scalar deterministic parameter β, the MLE estimate, denoted by $\hat{\beta}$, is the value that maximizes the likelihood function $P(\mathbf{x};\beta)$. One typically finds $\hat{\beta}$ by solving:

$$\frac{\partial \ln p(\mathbf{x};\beta)}{\partial \beta} = 0, \tag{2.23}$$

which may yield a closed-form solution or, alternatively, require numerical methods such as grid search or iterative maximization [37]. In the case where $\boldsymbol{\beta}$ is a vector, we take the partial derivative of each element within the vector individually.

2.5.5 Least Squares Estimator

The LS method offers an alternative approach that focuses on minimizing the discrepancy between the observed data and the model predictions. Unlike methods that rely on statistical descriptions of noise, the LS estimator is derived by directly minimizing the sum of the squared differences between the measured values and the predicted (or noiseless)

signal:

$$\hat{\beta}_{LS} = \arg\min_{\beta} \sum_{i=1}^{L} \left(x_i - \varphi_i(\beta)\right)^2 . \tag{2.24}$$

Here, $\varphi_i(\beta)$ represents the model's prediction corresponding to the i^{th} observation. The LS approach is particularly attractive due to its simplicity and minimal dependence on probabilistic assumptions regarding the noise. However, it should be noted that LS estimators are generally suboptimal; they do not necessarily attain the CRLB.

2.5.6 Nonlinear Least Squares Estimator

In many practical scenarios, the relationship between the observations and the parameter is nonlinear. The NLS estimator extends the LS approach to such cases by addressing the minimization of a nonlinear cost function:

$$\hat{\beta}_{\text{NLLS}} = \arg\min_{\beta} \sum_{i=1}^{L} \left(x_i - \varphi_i(\beta)\right)^2 . \tag{2.25}$$

In this formulation, the function $\varphi_i(\beta)$ is nonlinear in β. Due to the inherent nonlinearity, closed-form solutions are rarely available, and iterative numerical methods such as the Gauss-Newton or Levenberg-Marquardt algorithms are employed to obtain the solution. Despite their increased computational complexity, NLS methods are effective in providing accurate estimates in complex models, especially when initial parameter guesses are close to the true values and the noise levels are moderate [38], [37].

2.5.7 Kalman Filter for State Estimation

KF are widely used to estimate system states in linear dynamic systems represented in state-space form. The process model describes the evolution of the system state from time step $k-1$ to time step k as:

$$x_k = Fx_{k-1} + Bu_{k-1} + w_{k-1}, \tag{2.26}$$

where F is the state transition matrix, x_{k-1} is the previous state vector, B is the control-input matrix, u_{k-1} is the control vector, and w_{k-1} is the process noise, assumed to be zero-mean Gaussian with covariance Q, i.e., $w_{k-1} \sim \mathcal{N}(0, Q)$. The corresponding measurement model that links the state to the observed measurements is given by:

$$z_k = Hx_k + v_k. \tag{2.27}$$

Here, z_k is the measurement vector, H is the measurement matrix, and v_k is the measurement noise, also assumed to be zero-mean Gaussian with covariance R, i.e., $v_k \sim \mathcal{N}(0, R)$. This model establishes the relationship between the current state and the observed measurements.

The Kalman Filter aims to estimate the state x_k at time k, given the initial estimate x_0, the sequence of measurements $z_1, z_2, \ldots, z_k$, and the system matrices F, B, H, Q, and R. In most applications, these matrices are assumed to be time-invariant. Although Q and R are theoretically based on noise statistics, in practice, they are often treated as tuning parameters to optimize filter performance [40].

Kalman Filter Algorithm:

The KF consists of two main stages: *prediction* and *update*. These are also referred to as *propagation* and *correction* in some literature. The algorithm proceeds as follows:

Prediction Step

$$\hat{x}_k^- = F\hat{x}_{k-1}^+ + Bu_{k-1} \tag{2.28}$$

$$P_k^- = FP_{k-1}^+F^T + Q, \tag{2.29}$$

Update Step

$$y_k = z_k - H\hat{x}_k^-, \tag{2.30}$$

$$K_k = P_k^- H^T (HP_k^- H^T + R)^{-1}, \tag{2.31}$$

$$\hat{x}_k^+ = \hat{x}_k^- + K_k y_k, \tag{2.32}$$

$$P_k^+ = (I - K_k H)P_k^-. \tag{2.33}$$

In the above-listed equations, the hat notation , i.e., $\hat{x}$ indicates an estimate of a variable. Superscript minus (–) represents the predicted (prior) estimate, and superscript plus (+) represents the updated (posterior) estimate. P_k denotes the error covariance matrix, and K_k is the Kalman gain, which determines the weight given to the new measurement.

Finally, it is worth mentioning that the KF provides an optimal recursive solution to the linear quadratic estimation problem under the assumption of Gaussian noise, and it is highly effective in a wide range of applications, including localization, tracking, and sensor fusion in VLC systems [41].

2.5.8 Extended Kalman Filter

In real-world systems, many process and measurement models exhibit nonlinear behavior, which violates the assumptions of the standard KF. When either the state transition or the measurement function,or both, are nonlinear, the KF must be extended to handle such cases. The EKF addresses this by linearizing the nonlinear functions using first-order Taylor series expansions [37]. The nonlinear system can be described as follows:

$$s[t] = a(s[t-1]) + Bu[t-1], \tag{2.34}$$

$$x[t] = h(s[t]) + w[t]. \tag{2.35}$$

Here, $a(\cdot)$ is a nonlinear function describing the system dynamics, $h(\cdot)$ is a nonlinear function mapping states to measurements, and $w[t]$ is the measurement noise.

To apply EKF, we linearize $a(s[t-1])$ around the previous state estimate $\hat{s}[t-1|t-1]$ and $h(s[t])$ around the predicted state $\hat{s}[t|t-1]$ using first-order Taylor expansion:

$$a(s[t-1]) \approx a(\hat{s}[t-1|t-1]) + A[t-1](s[t-1] - \hat{s}[t-1|t-1]), \tag{2.36}$$

$$h(s[t]) \approx h(\hat{s}[t|t-1]) + H[t](s[t] - \hat{s}[t|t-1]). \tag{2.37}$$

The Jacobian matrices are defined as:

$$A[t-1] = \left.\frac{\partial a}{\partial s[t-1]}\right|_{s[t-1]=\hat{s}[t-1|t-1]} \quad \text{and} \quad H[t] = \left.\frac{\partial h}{\partial s[t]}\right|_{s[t]=\hat{s}[t|t-1]}. \tag{2.38}$$

Using the linearized approximations, the system becomes:

$$s[t] = A[t-1]s[t-1] + Bu[t-1] + (a(\hat{s}[t-1|t-1]) - A[t-1]\hat{s}[t-1|t-1]), \tag{2.39}$$

$$x[t] = H[t]s[t] + w[t] + (h(\hat{s}[t|t-1]) - H[t]\hat{s}[t|t-1]). \tag{2.40}$$

The EKF then proceeds with the following steps:

Prediction:

$$\hat{s}[t|t-1] = a(\hat{s}[t-1|t-1]) \tag{2.41}$$

$$N[t|t-1] = A[t-1]N[t-1|t-1]A[t-1]^T + BQB^T, \tag{2.42}$$

Update:

$$K[t] = N[t|t-1]H[t]^T \left(C[t] + H[t]N[t|t-1]H[t]^T\right)^{-1} \tag{2.43}$$

$$\hat{s}[t|t] = \hat{s}[t|t-1] + K[t]\left(x[t] - h(\hat{s}[t|t-1])\right) \tag{2.44}$$

$$N[t|t] = (I - K[t]H[t])N[t|t-1]. \tag{2.45}$$

The EKF is widely used in nonlinear tracking and estimation problems such as robot localization, navigation, and nonlinear signal processing in VLC applications.

2.5.9 Neural Network Fundamentals

An artificial neural network (ANN) can be regarded as a non-linear mapping from an input space to an output space, parameterized by weights and biases. Under mild assumptions, neural networks are universal function approximators and can represent any smooth func-

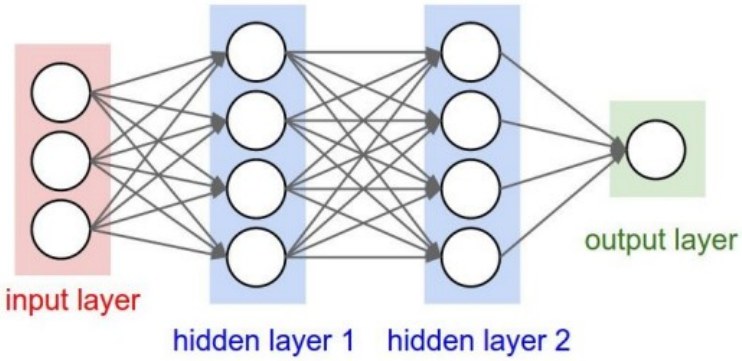

Figure 2.7: Neural network architecture consisting of an input layer, hidden layers, and an output layer [5].

tion to arbitrary accuracy as the number of neurons increases. They also serve as powerful channel estimators, complementing traditional estimation techniques in wireless communication systems [42], [43]. A typical neural network consists of an input layer, one or more hidden layers, and an output layer, as illustrated in Fig. 2.7. .

Neuron Model: Each neuron receives an input vector $\mathbf{x} = [x_1, x_2, \ldots, x_n]^T$ and produces an output by computing a weighted summation of its inputs, adding a bias term, and applying a nonlinear activation function. Mathematically, the operation of a single neuron can be expressed as

$$y = f\left(\mathbf{w}^T\mathbf{x} + b\right), \tag{2.46}$$

where $\mathbf{w} = [w_1, w_2, \ldots, w_n]^T$ is the weight vector, b is the bias, and $f(\cdot)$ is the activation function.

Layer Representation: Extending this formulation to a full layer of m neurons, the outputs can be written in vector form as

$$\mathbf{y} = f(\mathbf{W}\mathbf{x} + \mathbf{b}), \tag{2.47}$$

where $\mathbf{W} \in \mathbb{R}^{m \times n}$ is the weight matrix, $\mathbf{b} \in \mathbb{R}^m$ is the bias vector, and $f(\cdot)$ is applied element-wise. Thus, a neural network can be viewed as a composition of such layers.

Activation Functions: The activation function introduces nonlinearity, which is essential for approximating complex mappings. Common choices include:

- Sigmoid:

$$f(x) = \frac{1}{1 + e^{-x}}, \tag{2.48}$$

which maps real values to $(0, 1)$, often used for probabilistic binary classification.

- Hyperbolic tangent (tanh):

$$f(x) = \tanh(x) = \frac{e^x - e^{-x}}{e^x + e^{-x}}, \tag{2.49}$$

which maps to $(-1, 1)$ and is zero-centered.

- Rectified linear unit (ReLU):

$$f(x) = \max(0, x), \tag{2.50}$$

widely used in deep networks for efficiency and gradient stability.

- Softmax (for multi-class classification):

$$\text{Softmax}(z_j) = \frac{e^{z_j}}{\sum_{k=1}^{K} e^{z_k}}, \quad j = 1, \ldots, K, \tag{2.51}$$

which normalizes the output vector into a probability distribution across K classes.

Training Objective: Given training data $\{(\mathbf{x}_i, y_i)\}_{i=1}^{N}$, the network prediction is obtained by sequentially applying (2.46) and (2.47) across all layers, yielding $\hat{y}_i = f_{\mathbf{W},\mathbf{b}}(\mathbf{x}_i)$. The discrepancy between the predicted outputs $\hat{y}_i$ and the true targets y_i is measured using a loss function. For regression, the most common choice is the mean squared error (MSE):

$$\text{MSE} = \frac{1}{N} \sum_{i=1}^{N} (y_i - \hat{y}_i)^2 . \tag{2.52}$$

The training problem is therefore formulated as minimizing this cost with respect to the network parameters [43]:

$$\min_{\mathbf{W},\mathbf{b}} \frac{1}{N} \sum_{i=1}^{N} (y_i - f_{\mathbf{W},\mathbf{b}}(\mathbf{x}_i))^2 . \tag{2.53}$$

Summary: Equations (2.46) and (2.47) describe the forward propagation of signals through neurons and layers. The choice of activation function controls the nonlinearity applied at each stage. Finally, the optimization objective (2.53) drives the learning process by adjusting the weights and biases to minimize the cost function, such as MSE in regression or cross-entropy in classification [43].

2.6 Literature Review and Research Gap

VLC and VLP systems have attracted growing attention due to their potential to provide high-capacity communication and high-accuracy indoor localization. However, system performance is strongly affected by signal dependent noise whose variance scales with the received optical power. While early studies often ignored SDSN, some recent works have increasingly incorporated its impact on channel estimation and localization performance. More recently, RIN has also been investigated in VLC systems, though only from a channel estimation perspective.

In [44], the authors provided one of the earliest theoretical analyses of VLP accuracy under both thermal noise and SDSN. They derived the CRLB and showed that ignoring SDSN leads to overly optimistic accuracy predictions. Their results revealed that SDSN dominates performance at high RSS and low SNR, significantly degrading positioning accuracy. A precise LoS channel model for VLC introduced SDSN was proposed in [45]. They derived closed-form CRLB and MLE range estimator. Their work highlighted the harmful effect of SDSN and suggested the need for more robust approaches toward practical performance.

The study in [46] investigated VLC distance estimation under SDSN and imperfect synchronization. Using ToA-based CRLB analysis for synchronous, asynchronous, and bi-directional protocols, they showed that SDSN degrades accuracy, while the proposed bi-directional synchronization improves performance significantly. Authors in [35] investigated single-input single-output (SISO) VLC systems in the presence of SDSN. They derived the CRLB for channel estimation error and proposed LS and MLE estimators. Furthermore, they designed optimal and sub-optimal receivers and derived BER expressions, showing that SDSN, severely degrades system reliability. Authors in [20] introduced a SISO VLC

Table 2.2: Comparison of key SDSN/RIN works in VLC/VLP and their limitations.

Reference	**SDSN**	**RIN**	**Chan./Loc./Track**	**Contributions and Gaps**
Liu et al. (2020) [44]	✓	✗	✗/ ✓/ ✗	Derived CRLB under SDSN for range estimation.
Amini et al. (2021) [45]	✓	✗	✓/ ✓/ ✗	Proposed MLE-based range estimation; accuracy bounds derived for range estimation under SDSN
Cheema et al. (2021) [46]	✓	✗	✗/ ✓/ ✗	Investigated synchronization errors under SDSN; introduced bi-directional protocol in the case of distance estimation.
Yaseen et al. (2021) [35]	✓	✗	✓/ ✗/ ✗	LS/MLE estimators with SDSN addressed channel estimation only.
Yaseen et al. (2023) [20]	✓	✗	✓/ ✗/ ✗	LS/MLE/MAP/LMMS estimators with SDSN addressed random channel estimation .
Yaseen et al. (2025) [18]	✓	✓	✓/ ✗/ ✗	First joint SDSN+RIN analysis in the case of VLC channel estimation.
Comparison Insight	–	–	–	Existing works mainly derive CRLBs or focus on simplified SDSN/RIN models. Channel estimation is partly studied without making other estimation methods suitable for dependent noise, but localization and tracking in realistic noise conditions (SDSN+RIN+thermal) remain largely unexplored, motivating our proposed unified framework.

system under statistical random channel conditions and SDSN, and applied MLE, LS,least minimum mean square error (LMMSE), maximum a posteriori (MAP), and minimum mean square error (MMSE) estimators for channel estimation. They further demonstrated, via Monte Carlo simulations, that the presence of the SDSN significantly increases the MSE of the system, thereby degrading estimation performance.

More recently, in [18], they extended the analysis to laser diod (LD)-based VLC systems under the joint impact of SDSN and RIN. They derived CRLB, and analyzed LS and MLE estimators in the presence of both noise sources. This study represents the first comprehensive analysis of SDSN and RIN jointly, but it remained limited to channel estimation.

2.6.1 Research Gap

As highlighted in Table 2.2, a number of recent studies have started to incorporate the effect of SDSN and, more recently, RIN into VLC/VLP analyses. These works represent an important step forward compared to earlier models that ignored dependent noise altogether. However, their scope remains narrow and several critical issues are unresolved.

First, most contributions remain focused on channel estimation or distance estimation, while the more practical tasks of localization and tracking under dependent noise have not been addressed. Second, although SDSN and RIN have each been studied individually, there has been no comprehensive treatment of their joint effect on system performance, especially for localization and tracking in dynamic environments. Third, while analytical bounds such as the CRLB have been derived, prior studies have not advanced estimation techniques that actively overcome dependent noise effect, such as recursive Bayesian filters like EKF or machine-learning–based estimators. Fourth, there is a lack of benchmark comparisons between these recursive/nonlinear methods and classical estimators under SDSN and RIN.

Fifth, existing analyses are usually limited to a single type of light source, without a generalized model that accounts for LEDs, LDs, or arrays, and without studying how geometry and transmitter–receiver distance in systems affect performance under SDSN and RIN. Finally, none of the previous studies have examined how dependent noise shapes Bayesian bounds (e.g., BCRLB) in dynamic system settings or provided design rules that translate theory into reliable real-world VLC/VLP deployments. These open issues define the research gap and motivate the development of new frameworks that combine robust estimation techniques with realistic noise modeling to enhance end-to-end VLC/VLP performance, as proposed in the following chapters.

Chapter 3

A Novel Machine Learning Algorithm with Mathematical Modeling for Channel Estimation in VLC Systems

3.1 Introduction

In VLC systems, SDSN significantly degrades the accuracy of channel estimation, as its variance scales with the received optical power and cannot be effectively mitigated by traditional linear estimators such as LS. To address this challenge, this chapter introduces a simple yet novel machine learning–based estimator that explicitly accounts for the impact of signal-dependent noise. The proposed approach is innovative because it combines traditional estimation principles with the flexibility of neural network modeling, thereby capturing the non-linear behavior introduced by dependent noise. A rigorous mathematical framework is developed to characterize the estimator and compute its MSE, providing the-

oretical insight into its performance. Simulation results demonstrate that, in the presence of SDSN, the proposed estimator consistently outperforms the conventional LS method. Even in the ideal case without SDSN, the proposed algorithm remains slightly more efficient and accurate, confirming its robustness and broader applicability.

3.1.1 Related Work

Recent studies have explored machine learning for improving VLC channel estimation. Deep learning has shown effectiveness in enhancing accuracy and robustness. For instance, [47] proposed a Deep learning neural network (DNN)-based approach using a complex-valued neural network (CVNN) for multiple-input multiple-output (MIMO) DC-biased optical orthogonal frequency division multiplexing (DCO-OFDM) VLC systems. Their method employs a CVNN, which is specifically designed to process complex numbers directly. Similarly, the study in [48] introduced a flexible denoising convolutional neural network (FFDNet) for massive MIMO (m-MIMO) (m-MIMO) VLC channel estimation, while another work [49] proposed a deep residual convolutional blind denoising network (ResCBNet) to enhance estimation accuracy in indoor m-MIMO VLC systems.ResCBNet,trained with asymmetric and reconstruction loss functions, exhibits strong generalization capabilities and effectively handles complex noise environments. Furthermore, Authors in [50] applied machine learning to vehicular visible light communication (VVLC) channel modeling to improve path loss and channel frequency response (CRF) prediction beyond deterministic and stochastic methods. They compared multilayer perceptron (MLP)-NN,radial basis function (Rbf)-NN, and Random Forest using features such as distance, ambient light, and turbulence. Their results show Random Forest performs robustly with limited data, while MLP-NNs achieve better generalization for complex CRF

modeling.

However, despite the advancements in machine learning-based VLC channel estimation, existing approaches do not consider the impact of SDSN or explore less complex machine learning models. The dependence on highly complex Neural networks (NN) architectures results in significant computational overhead, limiting their practicality for real-time deployment in resource-constrained environments. Traditional LS estimation is a computationally efficient method for VLC channel estimation that requires no prior channel knowledge [21, 51, 52], but its performance degrades under SDSN. In this work, we enhance LS accuracy by integrating machine learning techniques, providing a more robust and efficient solution for VLC systems. To the author's best knowledge, no work in the literature has considered using machine learning to enhance the traditional LS estimation method to be used in the indoor VLC channel with the existence of the SDSN. Furthermore, no study has presented a mathematical framework for a machine learning network to estimate the channel in a VLC system, with or without considering SDSN.

3.2 System and Channel Models

This chapter presents a SISO-VLC downlink transmission model with an LED transmitter and a user within a circular coverage area, focusing on the LoS link between the transmitter and PD [53]. The model assumes static user positioning and includes both downlink and uplink transmission. In indoor environments, the LoS signal typically has a 7 dB advantage over the strongest non-line-of-sight (NLoS) component [54, 55] and references therein.

In the system model, the received signal at the PD is given by:

$$y = hx + \sqrt{hx}n_{\text{ds}} + n, \tag{3.1}$$

where x is the transmitted (pilot) signal, $n \sim \mathcal{N}(0, \sigma_n^2)$ is the thermal noise, and $\sqrt{hx}n_{\text{ds}}$ represents the sdsn with $n_{\text{ds}} \sim \mathcal{N}(0, \sigma_{ds}^2)$. SDSN is modeled as $n_{\text{ds}} \sim \mathcal{N}(0, \sigma_n^2\zeta^2)$, where $\zeta^2 = \frac{\sigma_{ds}^2}{\sigma_n^2}$ is the shot noise scaling factor, typically ranging from 1 to 10. The power of SDSN is proportional to both the input power x and the channel gain h, unlike thermal noise, which is independent of these factors [56, 57].

The channel gain h, representing the transmission link between the LED transmitter and the PD receiver, is modeled as described in [58, 59] and references therein:

$$h = \frac{A_{pd}\eta(m+1)}{2\pi D^2} \cos^m(\Theta) T_s(\Psi) g(\Psi) \cos(\Psi), \tag{3.2}$$

where Ψ denotes the angle of incidence relative to the surface normal of the PD, and Θ is the angle of irradiance with respect to the transmitter's surface normal. In this equation, $T_s(\Psi)$ represents the gain of the receiver's optical filter, and $g(\Psi) = \frac{n^2}{\sin^2(\Phi_{\text{FOV}})}$ is the gain of the optical concentrator. The gain $g(\Psi)$ depends on the refractive index n of the concentrator and the field of view (FOV) angle Φ_{FOV}. Note that $g(\theta_{\text{rx}}) = 0$ when $\theta_{\text{rx}} > \Phi_{\text{FOV}}$. Additionally, it A_{pd} represents the detection area of the PD, and η denotes the average responsivity of the receiver. The Euclidean distance between the transmitter and the receiver, D, is $D = \sqrt{L^2 + r^2}$, where L is the vertical distance from the LED to the PD surface and r is the horizontal distance from the center of the LED cell to the PD, as illustrated in Fig. 5.1. Finally, the Lambertian emission order m is expressed as $m = \frac{-1}{\log_2(\cos(\Phi_{1/2}))}$, where $\Phi_{1/2}$ denotes the semi-angle of the LED's emission.

3.3 Channel Estimation

Traditional RF-based communication methods, such as LS, MLE, MAP,MMSE and LMMSE estimators, can also be applied to VLC systems. However, VLC channels possess unique characteristics, such as positive and real signal requirements and the impact of SDSN [51], [60], which can limit the effectiveness of these techniques. Advanced methods like MAP and LMMSE require prior statistical information about the channel, which is often unavailable in practical VLC systems, particularly in large m-MIMO scenarios. Additionally, optimal methods such as MMSE rely on long pilot sequences, further increasing computational complexity and reducing practicality [51], [61]. This work addresses channel estimation in VLC systems by integrating an NN with the conventional LS estimator. The neural network mitigates SDSN-related performance degradation in LS estimation. After training, polynomial regression approximates the NN output, enabling a closed-form MSE calculation. This provides an efficient and accurate solution for VLC channel estimation.

We assume that the number of pilot symbols is denoted by N, and the LED transmits a pilot vector $\mathbf{x} = [x_1, x_2, \ldots, x_N]^T$, where $[.]^T$ represents the transpose operation. As a result, the received signal vector $\mathbf{y} = [y_1, y_2, \ldots, y_N]^T$ can be expressed as:

$$\mathbf{y} = h\mathbf{x} + \sqrt{h\,\mathrm{diag}(\mathbf{x})}\mathbf{n}_{ds} + \mathbf{n}, \tag{3.3}$$

where $\mathrm{diag}(\mathbf{x})$ is a $N \times N$ diagonal matrix containing the elements of the transmitted signal vector $\mathbf{x}$ along the main diagonal. The vectors $\mathbf{n} = [n_1, n_2, \ldots, n_N]^T$, $\mathbf{n}_{\mathrm{ds}} = [n_{\mathrm{ds1}}, n_{\mathrm{ds2}}, \ldots, n_{\mathrm{dsN}}]^T$ represent independent noise components. The entries of $\mathbf{n}$ are independent and identically distributed (i.i.d.) random variables, following $\mathbf{n} \sim \mathcal{N}(0, \sigma_n^2 I_N)$, where I_N is the identity matrix of size N. Similarly, the entries of $\mathbf{n}_{ds}$ follow $\mathbf{n}_{ds} \sim \mathcal{N}(0, \zeta^2\sigma_n^2 I_N)$, where ζ^2 represents the scaling factor for the SDSN. Finally, an important

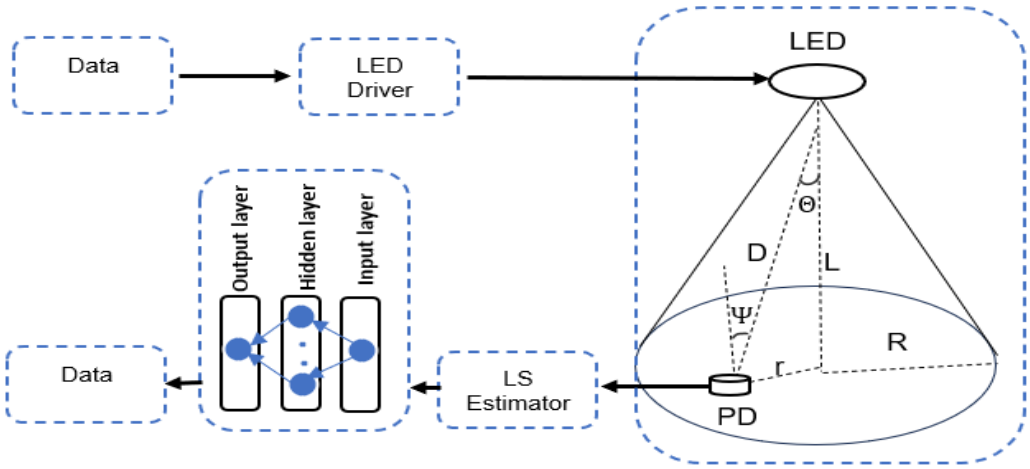

Figure 3.1: The SISO VLC system and channel models.

characteristic of VLC. systems is that the transmitted signal must be both positive and real. Therefore, all pilot symbols must satisfy the condition $x_i > 0, \forall i \in \{1, 2, \ldots, N\}$.

3.3.1 Least Squares Estimator

LS is a low-complexity estimator that does not need prior information. The estimated $\hat{h}$ using the LS estimator can be expressed as:

$$\hat{h}_{\text{LS}} = \frac{\mathbf{x}^T \mathbf{y}}{\|\mathbf{x}\|^2}. \tag{3.4}$$

To derive the MSE of the LS estimator, we first substitute (3.3) into (3.4). This allows us to express the ;sls estimator of the channel gain, h, as:

$$\hat{h}_{\text{LS}} = \frac{\mathbf{x}^T \mathbf{y}}{\|\mathbf{x}\|^2} = h + \frac{\mathbf{x}^T}{\|\mathbf{x}\|^2} \sqrt{h \ \text{diag}(\mathbf{x})} \mathbf{n}_{\text{ds}} + \frac{\mathbf{x}^T}{\|\mathbf{x}\|^2} \mathbf{n}. \tag{3.5}$$

The error of the LS estimator can be expressed as:

$$\epsilon_{\text{LS}} = \hat{h}_{\text{LS}} - h = \frac{\mathbf{x}^T}{\|\mathbf{x}\|^2}\left(\sqrt{h\ \text{diag}(\mathbf{x})}\mathbf{n}_{\text{ds}} + \mathbf{n}\right). \tag{3.6}$$

From (6), we can deduce that the error is a Gaussian random variable with zero mean and variance $\sigma^2_{\epsilon_{\text{LS}}}$, i.e., $\epsilon_{\text{LS}} \sim \mathcal{N}(0, \sigma^2_{\epsilon_{\text{LS}}})$. Therefore, the MSE of the LS estimator is simply the variance of the error, which can be expressed as:

$$\text{MSE}_{\text{LS}} = \sigma^2_{\epsilon_{\text{LS}}} = \frac{\sigma_n^2 \sum_{i=1}^{N} x_i^2(1 + \zeta^2 h x_i)}{\left(\sum_{i=1}^{N} x_i^2\right)^2}. \tag{3.7}$$

Assuming, without loss of generality, that the transmitted pilots $x_i = p$ for all i, the MSE can then be written as [62]:

$$\text{MSE}_{\text{LS}} = \sigma^2_{\epsilon_{LS}} = \frac{\sigma_n^2(1 + \zeta^2 h p)}{Np^2}. \tag{3.8}$$

It is worth mentioning that in the absence of the SDSN, i.e., $\zeta^2 = 0$, the MSE is inversely proportional to p^2 while, in the presence of the SDSN, the MSE is inversely proportional to p, indicating the harmful effect of the SDSN. Furthermore, increasing the number of pilots, N, will improve the estimation performance, and the presence or absence of the SDSN has no relation impact on the number of pilots.

3.3.2 Integrated Machine Learning and Least Squares Estimator

The proposed method begins by estimating the channel gain through a straightforward traditional estimator, such as the LS estimator, or another common approach like the MLE. In this work, the LS estimator is applied initially. The output from the LS estimation is

then refined and improved by passing it through NN.

Consider a feed-forward NN consisting of a single hidden layer with N_h neurons and a single output layer with one neuron. The output layer uses a linear activation function, while the hidden layer utilizes a nonlinear activation function. The hidden layer's output for each training sample is computed as:

$$\boldsymbol{y}_h = \Lambda^{(1)}(\boldsymbol{W}\hat{h}_{\mathrm{LS}} + \boldsymbol{b}). \tag{3.9}$$

where $\Lambda^{(1)}$ represents the hidden layer's activation function, $\boldsymbol{W} = [w_1, \ldots, w_k, \ldots w_{N_h}]^T$ is the weight matrix of dimensions $N_h \times 1$, and $\boldsymbol{b} = [b_1, \ldots, b_k, \ldots b_{N_h}]^T$ is the bias vector of size $N_h \times 1$. Next, the output layer generates the final output for each input as $\hat{h}_{\mathrm{NN}} = \Lambda^{(2)}(\boldsymbol{V}\boldsymbol{y}_h + \beta)$, where $\Lambda^{(2)}$ serves as the activation function of the output layer, $\boldsymbol{V} = [v_1, \ldots, v_k, \ldots v_{N_h}]$ is the weight matrix of dimensions $1 \times N_h$, and β is the scalar bias for the output layer.

In the training process of the ANN model, the set of parameters $\Gamma \triangleq \{\boldsymbol{W}, \boldsymbol{V}, \boldsymbol{b}, \beta\}$ is adapted to achieve the optimum Γ_{opt} that minimizes the cost function, which is the MSE between the output of the ANN and the real value of the channel gain; i.e., h therefore, the optimum set of parameters of the ANN model can be optimized as:

$$\Gamma_{\mathrm{opt}} = \min_{\Gamma} \mathbb{E}\left\{\left(h - \hat{h}_{\mathrm{NN}}\right)^2\right\}. \tag{3.10}$$

It is worth mentioning that the model's weights and biases are adjusted iteratively with each training sample. Considering M training samples, the optimal parameter Γ_{opt} is averaged over all samples, allowing for continuous refinement and improved accuracy.

3.4 Comprehensive Mathematical Framework and MSE Analysis

In this section, we analyze the neural network by examining its layers at the neuron level to derive an equivalent polynomial form. Using a Taylor series expansion, we approximate the network's behavior and derive a closed-form expression for the theoretical MSE of the estimated channel output, $\hat{h}_{\text{NN}}$, during the testing phase. This approach utilizes the fixed weights and biases from the training phase, enabling precise MSE performance assessment under the trained model parameters. As previously mentioned, we consider a feed-forward neural network with a single hidden layer containing N_h neurons and an output layer with a single neuron [63].

The output of the k^{th} neuron in the hidden layer, given that the activation function for the hidden layer is tanh, is:[1]

$$y_k = \tanh(u_k) = \tanh\left(w_k \hat{h}_{\text{LS}} + b_k\right) = \frac{e^{u_k} - e^{-u_k}}{e^{u_k} + e^{-u_k}}, \tag{3.11}$$

where $u_k = w_k \hat{h}_{\text{LS}} + b_k$, w_k and b_k are the weights and bias at the k^{th} neuron in the hidden layer, respectively. The output of the NN, $\hat{h}_{\text{NN}}$ is a linear combination of the activations of the hidden neurons multiplied by linear weights of the output layer v_k plus the output layer bias β [64]. It can be expressed as:

$$\hat{h}_{\text{NN}} = \sum_{k=1}^{N_h} v_k y_k + \beta = \sum_{k=1}^{N_h} v_k \tanh\left(w_k \hat{h}_{\text{LS}} + b_k\right) + \beta. \tag{3.12}$$

To find an approximate equivalent to the NN we use the Taylor expansion series.The

[1]The generalization to any activation function or additional hidden layers is straightforward.

Taylor expansion is particularly suitable in this context because it provides a systematic and mathematically rigorous method to approximate nonlinear functions with polynomials.

3.4.1 Taylor Series Approximation of $\tanh(u_k)$

The tanh function can be approximated by its Taylor series expansion around $u_k = 0$. The Taylor expansion of $\tanh(u_k)$ can be obtained as:

$$\tanh(u_k) = \sum_{n=0}^{\infty} \frac{d^n \tanh(0)}{du_k^n} \frac{u_k^n}{n!}, \tag{3.13}$$

where $\frac{d^n \tanh(0)}{du_k^n}$ represents the n^{th} derivative of $\tanh(u_k)$ evaluated around $u_k = 0$ and n represents the order of Taylor expansion. Using this series for the activation function, the output of the network can be rewritten as:

$$\hat{h}_{\text{NN}} = \sum_{k=1}^{N_h} v_k \sum_{n=0}^{\infty} \frac{d^n \tanh(0)}{du_k^n} \frac{u_k^n}{n!} + \beta. \tag{3.14}$$

Therefore, the MSE of $\hat{h}_{\text{NN}}$ at the testing phase after training is calculated as $\text{MSE}_{\text{NN}} = \mathbb{E}\left\{\left(h - \hat{h}_{\text{NN}}\right)^2\right\}$. After some mathematical manipulations, the MSE can be expressed as:

$$\begin{aligned} \text{MSE}_{\text{NN}} =& \mathbb{E}[h^2] - \mathbb{E}\left[2h\left(\sum_{k=1}^{N_h} v_k \sum_{n=0}^{\infty} \frac{d^n \tanh(0)}{du_k^n} \frac{(w_k \hat{h}_{\text{LS}} + b_k)^n}{n!} + \beta\right)\right] \\ &+ \mathbb{E}\left[\left(\sum_{k=1}^{N_h} v_k \sum_{n=0}^{\infty} \frac{d^n \tanh(0)}{du_k^n} \frac{(w_k \hat{h}_{\text{LS}} + b_k)^n}{n!} + \beta\right)^2\right], \end{aligned} \tag{3.15}$$

where $(w_k \hat{h}_{\text{LS}} + b_k)^n$ the term can be represented by a polynomial as $(w_k \hat{h}_{\text{LS}} + b_k)^n = \sum_{j=0}^{n} \binom{n}{j} (w_k \hat{h}_{\text{LS}})^{(n-j)} b_k^j$. After applying the expectation and performing the necessary cal-

culations on (3.15), the closed-form expression for $\mathrm{MSE}_{\mathrm{NN}}$ can be calculated as

$$\mathrm{MSE}_{\mathrm{NN}} = h^2 - 2h\left(\sum_{k=1}^{N_h}\sum_{n=0}^{\infty}\sum_{j=0}^{n}\frac{d^n\tanh(0)}{du_k^n}\frac{v_k}{n!}\binom{n}{j}(w_k)^{(n-j)}\mathbb{E}\left[(\hat{h}_{\mathrm{LS}})^{(n-j)}\right]b_k^j + \beta\right)$$
$$+\sum_{k=1}^{N_h}\sum_{k'=1}^{N_h}\sum_{n=0}^{\infty}\sum_{j=0}^{n}\sum_{n'=0}^{\infty}\sum_{j'=0}^{n'}\frac{d^n\tanh(0)}{du_k^n}\frac{v_k}{n!}\binom{n}{j}(w_k)^{(n-j)}b_k^j\frac{d^{n'}\tanh(0)}{du_{k'}^{n'}}\frac{v_{k'}}{n'!}\binom{n'}{j'}(w_{k'})^{(n'-j')}b_{k'}^{j'}$$
$$\times\,\mathbb{E}\left[(\hat{h}_{\mathrm{LS}})^{(n'-j')}(\hat{h}_{\mathrm{LS}})^{(n-j)}\right] + 2\beta\sum_{k=1}^{N_h}\sum_{n=0}^{\infty}\sum_{j=0}^{n}\frac{d^n\tanh(0)}{du_k^n}\frac{v_k}{n!}\binom{n}{j}(w_k)^{(n-j)}\mathbb{E}\left[(\hat{h}_{\mathrm{LS}})^{(n-j)}\right]b_k^j + \beta^2. \tag{3.16}$$

where the binomial function is defined as $\binom{a}{s} = \frac{a!}{s!(a-s)!}$, and since $\hat{h}_{\mathrm{LS}}$ is a Gaussian random variable with mean h and variance $\sigma^2_{\epsilon_{\mathrm{LS}}}$, i.e., $\hat{h}_{\mathrm{LS}} \sim \mathcal{N}(h, \sigma^2_{\epsilon_{\mathrm{LS}}})$, its n^{th} moment, i.e., $\mathbb{E}\left[(\hat{h}_{\mathrm{LS}})^n\right]$, can be found in many references, e.g., [65]. It is worth mentioning that, as we will see in Section 3.5, it is sufficient to use only the first two terms of the infinite series represented in (3.16). In fact, the first two terms will provide an accuracy of more than 99%.

A second remark is that we can see from equations (3.16) that the final MSE depends on the value of h as well as the weights and biases of the trained NN. Finally, to apply our proposed integrated estimation technique, the steps in Algorithm 1 should be followed. It is beneficial to note that for multiple test samples, the average $\mathrm{MSE}_{\mathrm{NN}}$ should be computed across all samples to assess overall performance. Moreover, our algorithm can be applied to enhance other estimation methods such as MLE, LMMSE, and MMSE; however, this increases complexity due to their need for more statistical information.

Algorithm 1 Integrated Machine Learning and Least Squares Estimator

Phase 1: Data Preparation
1) Generate the training data, we consider an indoor area of size $4\,\mathrm{m} \times 4\,\mathrm{m}$, and divide it into small blocks of $4\,\mathrm{cm} \times 4\,\mathrm{cm}$. We then calculate the true channel for each block, assuming PD in this block. After adding noise, we estimate $\hat{h}_{\mathrm{LS}}$ for each block from the received signal. This forms the training dataset, where $\hat{h}_{\mathrm{LS}}$ is the input, and the true channel h serves as the output.
2) Normalize the generated data and divide it into training (80%) and testing (20%) (The proposed algorithm can be directly applied to similar datasets.)

Phase 2: Neural Network Training and Testing
1) Initialize all NN state weights and biases.
2) Use $\hat{h}_{\mathrm{LS}}$ as input to the NN with the true channel values h as targets from the generated dataset.
3) Train the NN with stochastic gradient descent (SGD) to minimize the MSE between h and $\hat{h}_{\mathrm{LNN}}$, using the cost function in (3.10) averaged over all training samples.
4) Update the NN's weights and biases to minimize the MSE.
5) Save the trained model with optimized weights and biases for testing.

3.5 Simulation Results and Discussion

This section presents a numerical analysis of SISO-VLC systems, examining the impact of SDSN on channel estimation between the transmitter and the PD. We assess the LS estimator and its hybrid integration with an NN through both simulations and analytical evaluations. Furthermore, to generalize our proposed algorithm, we investigate how the NN enhances the performance of the ;smle (which is a direct extension to the presented approach). Furthermore, we compare the effectiveness of the proposed LS-shallow NN with the LS-MLP NN. The MLP, commonly used in channel estimation, features two hidden layers or more to analyze the impact of deeper architectures. The simulations, conducted in MATLAB, involve approximately 10^6 repeated Monte Carlo iterations per figure. The system parameters are set as follows: a field of view $\phi_{\mathrm{FOV}=70^\circ}$, transmission distance $L = 2\mathrm{m}$, and a responsivity factor $\eta = 0.4\mathrm{A/W}$. For the NN parameters, refer to

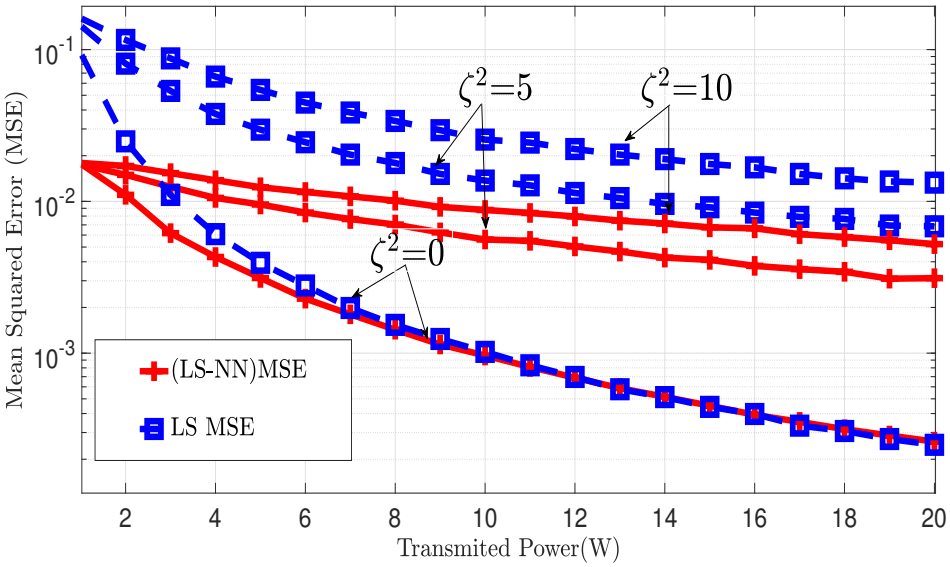

Figure 3.2: Comparison of the LS estimator and the integrated LS-NN estimator at different values of ζ^2.

Table 3.1.

In Fig. 3.2, the average MSE_{NN} and, MSE_{LS} for all testing samples, the corresponding estimated channels $\hat{h}_{\text{NN}}$ and $\hat{h}_{\text{LS}}$, are plotted against the transmitted power at thermal noise varince $\sigma_n^2 = 0.1$. From this figure, we observe that as the SDSN scaling factor ζ^2 increases, the MSE rises across all estimation methods. However, the proposed NN-based algorithm effectively reduces the MSE, particularly at higher ζ^2 values, outperforming the LS estimator. Additionally, at lower transmitted power levels, the NN-based method shows superior performance. Even in the absence of SDSN, it slightly outperforms the LS estimator, highlighting its robustness in handling material imperfections.

Fig. 3.3 compares the MSE from the NN estimation using the full tanh activation function and its Taylor expansion with the theoretical mathematical expression of the MSE at $\zeta^2 = 5$. The results demonstrate that the MSE obtained using the NN agrees with

Table 3.1: The Parameters Of The NN.

Parameters	Values
Size of the training data	8000
Size of the validation data	2000
Number of epochs	100
Number of hidden layers	1
Learning rate	0.001
Number of hidden layer neurons (N_h)	10
Loss function	MSE
Activation function	tanh

the theoretical MSE from (3.16), making it applicable for practical use. Additionally, you can see from the figure that when the σ_n^2 increases, the MSE increases in all techniques. Furthermore, the figure shows that, although the analytical expression for the MSE involves an infinite series, using only the first two terms yields highly accurate results. This trend also holds true for other activation functions.

Fig. 3.4 illustrates that the proposed algorithm, utilizing a shallow NN, enhances the MLE performance at different ζ^2 values when $\sigma_n^2 = 0.1$. This figure demonstrates that incorporating NN improves estimation accuracy in the presence of SDSN noise. Additionally, increasing the SDSN scaling factor leads to a higher MSE, while the NN further enhances estimation performance. The MLE estimator in the presence of SDSN is more complex to find, as described in [62]. Moreover, it requires knowledge of the likelihood function of the received signal, making it computationally demanding. In contrast, the LS estimator is less complex and mathematically tractable.

Fig. 3.5 presents a performance comparison of LS estimation, LS-NN, and LS-MLP across different values of σ_n^2 for $\zeta^2 = 10$. The results indicate that both LS-NN and LS-MLP consistently outperform LS alone at any σ_n^2. The MLP model comprises two hidden

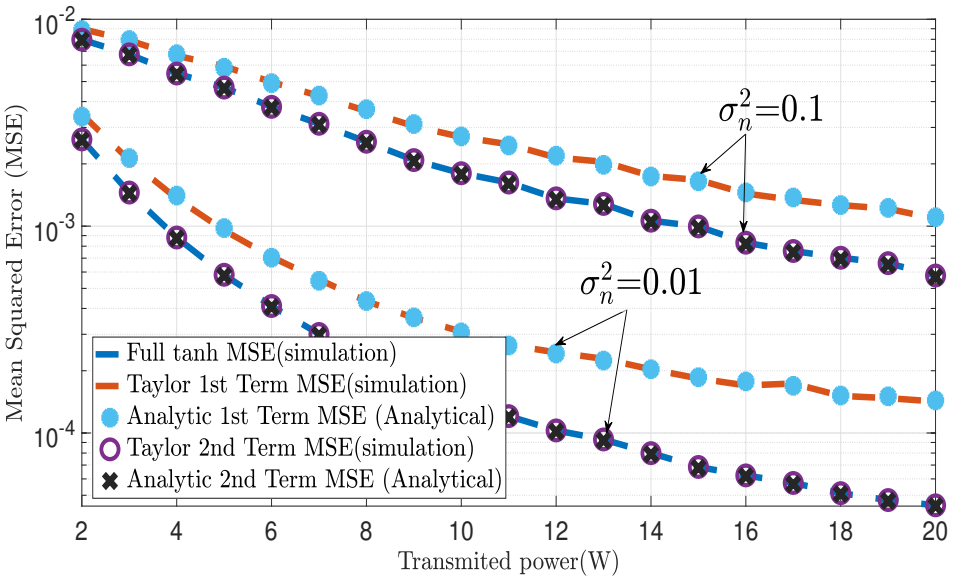

Figure 3.3: Comparison of NN simulation MSE with analytical MSE across varying terms in the Taylor expansion at different values of σ_n^2.

layers with 10 neurons each. However, the performance improvement of LS-NN and LS-MLP remains closely similar. Therefore, given the problem constraints, a single-layer NN is sufficient, avoiding unnecessary complexity in the neural network.

3.6 Conclusion

This chapter introduced the first integrated technique that combines LS estimation with an NN to estimate the channel in VLC under SDSN. A closed-form MSE expression was derived and validated against simulations, showing close alignment. The proposed approach improves accuracy under SDSN while maintaining low complexity. Once trained, the MSE_{NN} rule can be applied directly, offering a practical framework for future VLC systems. Moreover, the method can be directly extended to estimate the range between

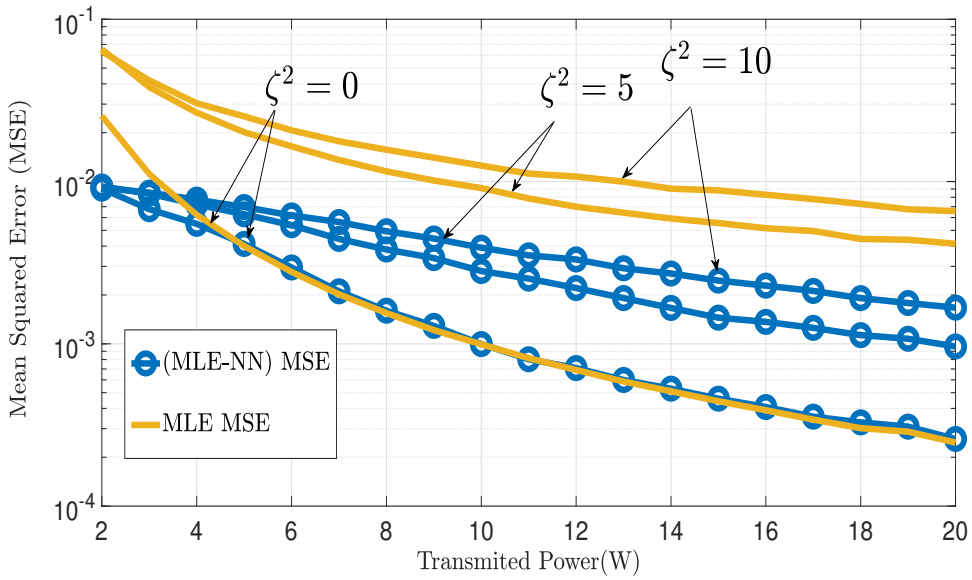

Figure 3.4: Comparison of MLE and integrated MLE-NN estimator at different values of ζ^2.

the transmitter and receiver, as the relation between range and channel can be calculated from eq.3.2 .

3.7 Publications Resulted from This Chapter

S. H. ElFar, S. Ikki, and M. Yassen, "A Novel Machine Learning Algorithm for Channel Estimation in VLC Systems," *IEEE Wireless Communications Letters*, vol. 14, no. 7, pp. 2084–2088, Jul. 2025.

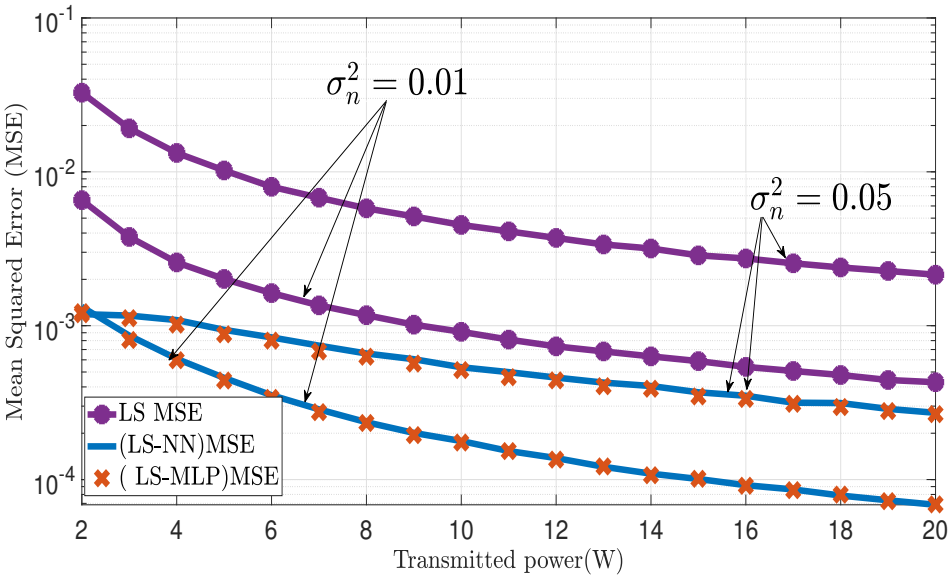

Figure 3.5: Comparison of LS, LS-NN, and LS-MLP at different values of σ_n^2.

Chapter 4

Insights into Visible Light Positioning: Range Estimation and Bayesian Cramér-Rao Lower Bound Analysis

4.1 Introduction

This chapter explores range estimation in VLP systems under SDSN. A SISO VLC setup is considered, and three estimation methods MLE, NLS, and the EKF are examined. The BCRLB is derived to evaluate the theoretical limits of estimation performance. Simulation results show that the EKF outperforms the other techniques, particularly at high SDSN levels, and closely approaches the BCRLB under favorable conditions. The study also investigates the effect of receiver tilting and system parameters such as transmitted power and number of pilot signals, offering practical insights for designing accurate and robust indoor VLP systems.

4.1.1 Related Work

Using VLP derives positions from RSS measured by smartphone image sensors or dedicated PDs viewing modulated luminaires, offering a precise and economical indoor method with strong immunity to RF interference and reduced multipath relative to RF systems [66].

Despite numerous studies addressing thermal noise in VLP systems, there remains a significant gap in research on the adverse impact of SDSN and strategies to mitigate its effects for improved estimation. Therefore, this work employs recursive estimation techniques, particularly the EKF, to enhance estimation robustness under SDSN.

The KF is a recursive estimator designed to estimate the state of a linear system [67], and it has been widely applied in VLP to improve target estimation accuracy. For recursive estimators, the BCRLB serves as a natural benchmark since it incorporates prior stochastic information [68]. However, because many positioning systems are inherently nonlinear, the KF often fails to meet its optimality conditions. To address this issue, nonlinear extensions such as the EKF have been developed and successfully applied in VLP systems [69].

4.2 System Model

In our system setup, an LED is affixed to the ceiling at a predetermined height. We employ a SISO VLP system for range detection. The LED is responsible for covering a specific circular area with radius Y, as depicted in Fig.4.1 and the received signal at the PD can be written as [62], [70]

$$r = hx + \sqrt{hx}n_{\text{ds}} + n, \tag{4.1}$$

where x, is the transmitted pilot (known) signal, n is the signal-independent thermal noise, $n \sim \mathcal{N}(0, \sigma_n^2)$, and $\sqrt{hx}n_{\text{ds}}$ denotes the SDSN, where $n_{\text{ds}} \sim \mathcal{N}(0, \sigma_{ds}^2)$. We represent the

SDSN in terms of thermal noise as $n_{\text{ds}} \sim \mathcal{N}(0, \sigma_n^2 \zeta^2)$, where $\zeta^2 = \sigma_{ds}^2/\sigma_n^2$, is the shot noise scaling factor that indicates the strength of the SDSN compared to the thermal noise.

In the context of the term ζ^2, it's important to highlight that this parameter can be set within a practical range, typically spanning from 1 to 10, by configuring the receiver's parameters [56, 62]. In general, shot noise typically follows a Poisson distribution. Nevertheless, as the number of received photons increases significantly, it converges towards a Gaussian distribution. This behavior is related to the high-intensity nature of light in VLC systems [71,72] . The channel gain h between the LED and the user can be expressed

$$h = \frac{A_{pd}\eta(m+1)}{2\pi d^2} \cos^m(\phi_{tx}) T_s(\theta_{rx}) g(\theta_{rx}) \cos(\theta_{rx}), \tag{4.2}$$

where several key parameters and relationships are incorporated in the above equation: ϕ_{tx} represents the angle of irradiance, θ_{rx} signifies the angle of incidence surface, $T_s(\theta_{rx})$ stands for the gain associated with the receiver's optical filter, $g(\theta_{rx}) = \frac{n^2}{\sin^2(\phi_{\text{FOV}})}$ describes the gain of the optical concentrator, which relies on the refractive index n of the concentrator and the field of view (FoV) angle, i.e., ϕ_{FOV}. It's important to note that $g(\theta_{rx}) = 0$ when $\theta_{rx} > \phi_{FOV}$. Additionally, A_{pd} denotes the detection area of the photodetector, and η represents the average responsivity of the receiver. Furthermore, $m = \frac{-1}{\log_2(\cos(\Phi_{1/2}))}$ is the Lambertian radiation order and is determined by the LED emission semi-angle $\Phi_{1/2}$ where the receiver and transmitter face each other $\cos(\phi_{tx}) = \cos(\theta_{rx})$.

Even more, we delve into scenarios where the receiver plane is not parallel to the transmitter plane, specifically addressing cases where the receiver is inclined at an angle γ [73], as illustrated in Fig. 4.1. In this general case, where there is a tilting angle, the channel equation changes as $\cos(\theta_{rx}) = \cos(\phi_{tx_t} - \gamma) = \frac{L_t}{d}\cos\gamma + \frac{y_t}{d}\sin\gamma$ [74], where $\cos(\phi_{tx_t}) = \frac{L_t}{d}$, ϕ_{tx_t} is the angle of irradiation in case of having a tilting angle, d is the Euclidean distance

from the transmitter to the receiver, which can be calculated as $d = \sqrt{L_t^2 + y_t^2}$, where L_t corresponds to the vertical distance from the LED to the PD surface and y_t is the horizontal distance from the center of the cell to the PD at any tilting angle value. Note that $L_t = L - L_0 = L - \beta \sin\gamma$, $y_t = y - y_0 = y - \beta(1 - \cos\gamma)$, where L and y are the vertical and horizontal distances at $\gamma = 0$ respectively, β is the PD length and L_0 and y_0 are the change in vertical and horizontal distances due to the presence of the tilting angle, as illustrated in Fig. 4.1, see [73] and the references therein. Hence, the received signal in (4.1) can be rewritten as

$$r = cxd^{-\alpha}x + \sqrt{cxd^{-\alpha}}n_{ds} + n, \tag{4.3}$$

where $\alpha = m + 3$ and

$$c = \frac{A_{pd}\eta(m+1)}{2\pi} T_s(\theta_{rx_t}) g(\theta_{rx_t}) L_{t^m} \left(L_t \cos\gamma + y_t \sin\gamma\right). \tag{4.4}$$

It's worth noting that the distortion variance is directly influenced by the distance between the transmitter and the receiver. This sets the additive distortion term apart from conventional receiver noise, which remains independent of distance.

4.3 Range estimation Techniques

In this section, we set out to estimate the range between the transmitter and the PD, which we label d. Our methodology incorporates two distinct estimation approaches. Initially, we apply a non-recursive approach using MLE and NLS estimators to determine an estimate of the distance.

Subsequently, we introduce the EKF as a recursive approach to estimate the same distance parameter. Unlike the MLE and NLS estimators, the EKF brings a dynamic

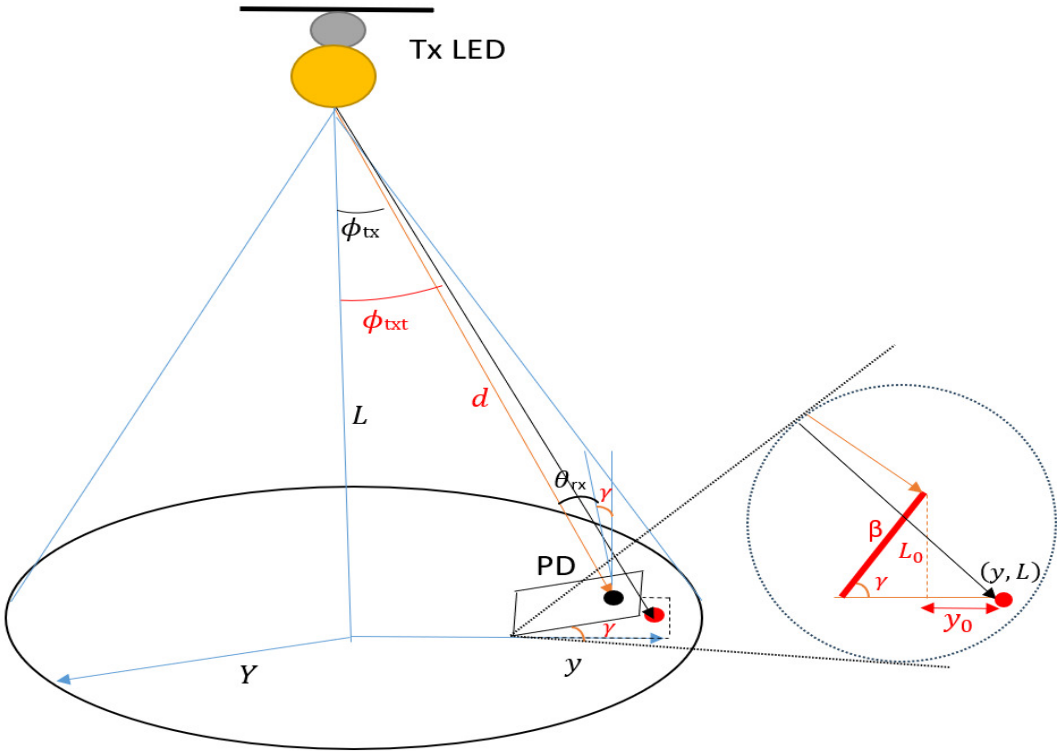

Figure 4.1: Visible light positioning system model.

analysis into play, allowing the adjustment of the estimate over time through its iterative equations [37].

4.3.1 Maximum Likelihood Estimator

The MLE estimator identifies unknown parameters by maximizing their likelihood function, as represented in their PDF [41]. We assume that the vertical distance (height) is a known quantity. Then, the vector of received signals, denoted by $\mathbf{r} = [r_1, r_2, \ldots, r_N]^T$, where $(.)^T$ represents the transpose operator, can be written as

$$\mathbf{r} = c\mathbf{x}d^{-\alpha} + \sqrt{cd^{-\alpha}}\mathbf{z} \odot \mathbf{n_{ds}} + \mathbf{n}. \tag{4.5}$$

Let N be the number of pilot symbols and $\mathbf{x} = [x_1, x_2, \cdots, x_N]^T$ be the transmitted pilots' vector, and $\mathbf{z} = [\sqrt{x_1}, \sqrt{x_2}, \cdots, \sqrt{x_N}]^T$ and $\odot$ is the Hadamard product operator and $\mathbf{n} = [n_1, n_2, \ldots, n_N]^T$ is the thermal noise vector, and $\mathbf{n}_{ds} = [n_{ds1}, n_{ds2}, \ldots, n_{dsN}]^T$ represents SDSN vector. The elements of $\mathbf{n}$ are independent and identically distributed (i.i.d) random variables, i.e., $\mathbf{n} \sim \mathcal{N}(0, \sigma_n^2 \mathbf{I}_N)$ where $\mathbf{I}_N$ is the identity matrix of size N. The same for $\mathbf{n}_{ds}$, all the elements are i.i.d, so $\mathbf{n}_{ds} \sim \mathcal{N}(0, \zeta^2 \sigma_n^2 I_N)$. It's important to note that all pilot symbols should hold positive values, i.e., $x_i > 0$, where $i \in \{1, 2, \cdots, N\}$. The first step in deriving the MLE estimator for our problem involves formulating the PDF for the initially received signal, which can be expressed as

$$f(\boldsymbol{r}|d) = \prod_{i=1}^{N} \frac{1}{\sqrt{2\pi\sigma_s^2}} \exp\left(-\frac{(r_i - c x_i d^{-\alpha})^2}{2\sigma_s^2}\right). \tag{4.6}$$

The range estimation can be calculated by solving for $\frac{\partial}{\partial d} \ln f(\boldsymbol{r}|d) = 0$ as follows

$$\frac{\partial}{\partial d} \ln f(\boldsymbol{r}|d) = \sum_{i=1}^{N} \frac{-1}{2\sigma_s^2} \frac{\partial \sigma_s^2}{\partial d} - \sum_{i=1}^{N} x_i c \alpha d^{-\alpha-1} \frac{(r_i - c x_i d^{-\alpha})}{\sigma_s^2} + \sum_{i=1}^{N} \frac{1}{2} (r_i - c x_i d^{-\alpha})^2 (\sigma_s^2)^{-2} \frac{\partial \sigma_s^2}{\partial d} = 0, \tag{4.7}$$

where $\sigma_s^2 = \sigma_n^2 + \sigma_{ds}^2$, recalling that $\sigma_{ds}^2 = x_i c d^{-\alpha} \zeta^2 \sigma_n^2$, therefore, $\frac{\partial \sigma_s^2}{\partial d} = -x_i c \alpha d^{-\alpha-1} \zeta^2 \sigma_n^2$. It can be seen that finding a closed-form solution for the roots of the given equation $\hat{d}_{ML}$ manually is virtually impossible. However, numerical methods and software tools such as MATLAB can easily compute the solution for $\hat{d}_{ML}$. Analytically studying the MSE, specifically the distance error of the MLE estimation, proves to be exceedingly challenging. Therefore, we rely on the simulation results presented later in the numerical section.

4.3.2 Nonlinear Least Squares

NLS problems arise when the received signal model cannot be expressed linearly in terms of the parameter we need to estimate like the relation between $\boldsymbol{r}$ and d as shown in (4.5). To simplify the NLS problems, we transform the parameters to linearize the problem [75]. By substituting $cd^{-\alpha}$ with g and solving it as a linear least squares problem. The least-squares estimator $\hat{g}_{\text{LS}}$ minimizes the sum of the squared differences between the observed and predicted values [37]. Therefore, the least squares estimator can be calculated using (4.5) as

$$\hat{g}_{\text{LS}} = \arg\min_{g} \|\boldsymbol{r} - \boldsymbol{x}g\|^2 = \frac{\boldsymbol{x}^T\boldsymbol{r}}{\|\boldsymbol{x}\|^2}. \tag{4.8}$$

From (4.5), $\hat{g}_{\text{LS}}$ can be written as

$$\hat{g}_{\text{LS}} = \frac{\boldsymbol{x}^T\boldsymbol{x}}{\|\boldsymbol{x}\|^2}g + \frac{\boldsymbol{x}^T}{\|\boldsymbol{x}\|^2}\sqrt{g}\mathbf{z} \odot \mathbf{n_{ds}} + \frac{\boldsymbol{x}^T}{\|\boldsymbol{x}\|^2}\mathbf{n}. \tag{4.9}$$

The performance of the LS estimator can be evaluated by determining the MSE, which is equivalent to the estimation error variance. After some mathematical manipulations, the MSE of the estimator can be given as

$$\sigma^2_{\hat{g}_{\text{LS}}} = \frac{\sigma_n^2 \sum_{i=1}^{N} (1 + \sigma^2_{gds})}{\|\boldsymbol{x}\|^2}, \tag{4.10}$$

where $\sigma^2_{gds} = x_i g \zeta^2$. From (4.8), the estimated range $\hat{d}_{\text{Ls}}$ can be written as

$$\hat{d}_{\text{LS}} = \left(\frac{\boldsymbol{x}^T\boldsymbol{r}}{c\|\boldsymbol{x}\|^2}\right)^{\frac{-1}{\alpha}}. \tag{4.11}$$

The MSE of the range estimator can be given as

$$\sigma^2_{\hat{d}_{\mathrm{LS}}} = \left(\frac{\partial d}{\partial g}\right)^2 \sigma^2_{\hat{g}_{\mathrm{LS}}}, \tag{4.12}$$

therefore If we assume the pilots are identical $x_i = p$, then the MSE can be simplified to

$$\sigma^2_{\hat{d}_{\mathrm{LS}}} = \frac{d^{2\alpha+2}\sigma_n^2 + pcd^{\alpha+2}\zeta^2\sigma_n^2}{Np^2c^2\alpha^2}. \tag{4.13}$$

From (4.13), we observe that the MSE of the NLS estimator increases with rising SDSN, a trend that will be explained in detail in the Simulation Results and Discussion section.

4.3.3 Extended Kalman Filter

To improve the precision of our range estimation over time, an initial estimation of d can be achieved using an MLE estimator or assumed, followed by refinement through the application of EKF sequences. This process incorporates the assumption that the range follows a dynamic model influenced by time and is subject to uncertainty noise. The computational complexity of EKF is higher than that of the MLE and NLS because EKF is a recursive method that depends on multiple iterations, each involving numerous mathematical calculations to update the state estimates. However, EKF is effective in reducing the impact of measurement noise, specially, SDSN in our case, through its recursive process and, the computational complexity is explained in detail in [76–78]. The current range estimation $d[t]$ at time t can be determined by a linear transformation of its previous state $d[t-1]$ with added uncertainty noise $u[t]$ where $t \geq 0$ and is mathematically represented by

$$d[t] = d[t-1] + u[t]. \tag{4.14}$$

Furthermore, the dynamic behavior of the range is characterized by a Gaussian transition model, while the uncertainty noise is treated as a stochastic Gaussian process [41], [79]. Thus, $u(t)$ follows the Gaussian distribution with zero mean and variance σ_u^2, i.e., $u[t] \sim N(0, \sigma_u^2)$. Moreover, the conditional probability of $f(d[t]|d[t-1]) \sim N(d[t-1], \sigma_u^2)$, when we assume samples are indepentent. Additionally, the measurement or observation vector $\boldsymbol{r}[t]$ with dimension $N \times 1$ in (4.5), can be expressed as

$$\boldsymbol{r}[t] = \boldsymbol{e}(d[t]) + \mathbf{n_s}[t], \tag{4.15}$$

where $\boldsymbol{e}(d[t]) = c\mathbf{x}d[t]^{-\alpha}$ and $\mathbf{n_s}[t] = \sqrt{cd[t]^{-\alpha}}\mathbf{z} \odot \mathbf{n_{ds}}[t] + \mathbf{n}[t]$. It is worth mentioning that $\boldsymbol{e}(d[t])$ represents the nonlinear equation modeling the relationship between the received vector and distance. Additionally, $\mathbf{n_s}[t]$ indicates the aggregate noise from thermal noise and shot noise, modeled as Gaussian with $\boldsymbol{n_s}[t] \sim \mathcal{N}(0, \boldsymbol{R})$, where $\boldsymbol{R} = \sigma_s^2 \boldsymbol{I}_N$.

When addressing the non-linear relationship between the received vector and the distance between the transmitter and receiver, we employ the EKF for its ability to manage non-linearity effectively [37]. The EKF method involves approximating the nonlinear $\boldsymbol{e}(d[t])$ function through a Taylor series expansion, specifically linearizing it at the point of the current estimate. This process allows the filter to update its state estimates by effectively handling the non-linearity of the system by linearizing $\boldsymbol{e}(d[t])$ around $\hat{d}[t|t-1]$ as follows.

$$\boldsymbol{e}(d[t]) \approx \boldsymbol{e}(\hat{d}[t|t-1]) + \left.\frac{\partial \boldsymbol{e}}{\partial d[t]}\right|_{d[t]=\hat{d}[t|t-1]} (d[t] - \hat{d}[t|t-1]). \tag{4.16}$$

We assume that the relationship between the received vector and range can be linearized, under the condition that noise is absent. This allows us to disregard the linearization effects of dependent noise. However, the influence of dependent noise is considered within the context of the covariance of measurement noise.

This approach enables a simplified linear analysis while ensuring that the complexities introduced by noise dependencies are accounted for in the uncertainty quantification of the measurements. Therefore, the measurement vector after linearization can be written as

$$\boldsymbol{r}[t] = \boldsymbol{s}[t]d[t] + \mathbf{n_s}[t] + \left(\boldsymbol{e}(\hat{d}[t|t-1]) - \boldsymbol{s}[t]\hat{d}[t|t-1]\right), \tag{4.17}$$

where

$$\boldsymbol{s[t]} = \left.\frac{\partial \boldsymbol{e}}{\partial d[t]}\right|_{d[t]=\hat{d}[t|t-1]}. \tag{4.18}$$

The following set of equations delineates the recursive sequence of steps necessary for the effective implementation of EKF [41]:

$$\hat{d}[t|t-1] = \hat{d}[t-1|t-1], \tag{4.19a}$$

$$v[t|t-1] = v[t-1|t-1] + \sigma_u^2, \tag{4.19b}$$

$$\boldsymbol{k}[t] = v[t|t-1]\boldsymbol{s^T}[t]\left(\boldsymbol{R}[t] + \boldsymbol{s}[t]v[t|t-1]\boldsymbol{s}^T[t]\right)^{-1}, \tag{4.19c}$$

$$\hat{d}[t|t] = \hat{d}[t|t-1] + \boldsymbol{k[t]}(\boldsymbol{r}[t] - \boldsymbol{e}(\hat{d}[t|t-1])), \tag{4.19d}$$

$$v[t|t] = (1 - \boldsymbol{k}[t]\boldsymbol{s}[t])v[t|t-1], \tag{4.19e}$$

where the Kalman gain $\boldsymbol{k}[t]$ with dimension $1 \times N$, $v[t]$ is the minimum prediction MSE with dimension 1×1. The initial value $\hat{d}[-1|-1]$ is set to d_0, which can either be estimated from the MLE estimator or assumed. Through iterations, its effect diminishes. Moreover, the initial value of $v = [-1|-1] = \sigma_u^2$.

4.4 Theoretical Bounds: Bayesian Cramér-Rao Lower Bound

In this section, we derive BCRLB, which represents the highest level of accuracy attainable in estimating the range $d[t]$ by any estimation techniques/algorithms. Initially, we derive the Fisher Information for the measurements $\mathrm{J}^{M}(d[t])$ as

$$\mathrm{J}^{M}(d[t]) = -\mathbb{E}\left\{\frac{\partial^2}{\partial d^2[t]} \ln f(\boldsymbol{r}[t]\big|d[t])\right\}, \tag{4.20}$$

where $\mathbb{E}$ is the expectation operator. Without loss of generality, and assuming that all the transmitted symbols are identical $x_i = p$ and, after tedious mathematical manipulation, the Fisher Information can be expressed as

$$\mathrm{J}^{M}(d[t]) = \frac{Np^2c^2\zeta^4\alpha^2(d[t])^{-2\alpha-2}}{2\left(1+\zeta^2cp(d[t])^{-\alpha}\right)^2} + \frac{Np^2c^2\alpha^2(d[t])^{-2\alpha-2}}{\sigma_n^2+\sigma_n^2\zeta^2c(d[t])^{-\alpha}p}. \tag{4.21}$$

Subsequently, we obtain the Bayesian information $\mathrm{J}^{B}d([t])$ by amalgamating the insights derived from measurement data with prior knowledge as follows

$$\mathrm{J}^{B}d([t]) = \underbrace{\mathrm{J}^{M}(d[t])}_{\text{Measurements}} + \underbrace{q_{22}[t] - q_{21}[t]\left[\mathrm{J}^{B}(d[t-1]) + q_{11}[t]\right]^{-1} q_{12}[t]}_{\text{Priori-Information}}. \tag{4.22}$$

After detailed mathematical manipulations as discussed in [80], the quantities $q_{11}[t]$, $q_{12}[t]$, $q_{21}[t]$, and $q_{22}[t]$ can be derived and obtained as follows

$$q_{11}[t] = \mathbb{E}\left\{-\frac{\partial^2 \ln f(d[t]|d[t-1]}{\partial d^2[t-1]}\right\} = \frac{1}{\sigma_u^2}, \tag{4.23a}$$

$$q_{21}[t] = \mathbb{E}\left\{-\frac{\partial^2 \ln f(d[t]|d[t-1]}{\partial d[t-1]d[t]}\right\} = \frac{-1}{\sigma_u^2}, \tag{4.23b}$$

$$q_{12}[t] = \mathbb{E}\left\{-\frac{\partial^2 \ln f(d[t]|d[t-1]}{\partial d[t]d[t-1]}\right\} = \frac{-1}{\sigma_u^2}, \tag{4.23c}$$

$$q_{22}[t] = \mathbb{E}\left\{-\frac{\partial^2 \ln f(d[t]|d[t-1]}{\partial d^2[t]}\right\} = \frac{1}{\sigma_u^2}, \tag{4.23d}$$

where $\mathrm{J}^B(d[t-1])$ is the Bayesian Fisher information at the previous time. Furthermore, the BCRLB($d[t]$) of the estimation of $d[t]$ at the t^{th} sample is given by BCRLB($d[t]$) = $1/\mathrm{J}^B d([t])$.

In considering the effect of SDSN on the BCRLB, several key insights can be derived:

- *Remark 1:* The value of the measurement Fisher information $\mathrm{J}^{(M)}d([t])$ increases as the number of pilots N increases, as shown in (4.21). This implies a reduction in BCRLB when N increases.

- *Remark 2:* As ζ tends towards zero, indicating no SDSN, (4.21) can be expressed as

$$\lim_{\zeta \to 0} 1/\mathrm{J}^M(d[t]) = \frac{\sigma_n^2}{Np^2c^2\alpha^2 d[t]^{-2\alpha-2}}. \tag{4.24}$$

  This shows that when $\zeta = 0$, the BCRLB increases as the thermal noise σ_n^2 increases. However, increasing the number of pilots and transmitted power will decrease the BCRLB.

- *Remark 3*: From (4.21), it's evident that $\mathrm{J}^M(d[t])$ depends on the parameter we look

to estimate, $d[t]$. Therefore, BCRLB depends on $d[t]$, with lower BCRLB when $d[t]$ is closer to the LED.

- *Remark 4:* At very high transmitted power, i.e., $p \to \infty$, $\mathrm{J}^M(d[t])$ is reduced to

$$\lim_{p\to\infty} 1/\mathrm{J}^M(d[t]) = \frac{\zeta^2\sigma_n^2}{Npc\alpha^2 d[t]^{-\alpha-2}}. \tag{4.25}$$

  It can be observed from (4.25) that BCRLB doesn't saturate at a high power level. Additionally, it is worth mentioning that BCRLB $\to 0$, when $p \to \infty$.

- *Remark 5:* It can be noticed from (4.24) that in the absence of SDSN, BCRLB is proportional to $1/p^2$, while in the presence of SDSN in (4.25), it is proportional to $1/p$. Therefore, SDSN mitigates the improvement in BCRLB that can be received by increasing the transmitted power p.

- *Remark 6:* The estimated range $\hat{d}$ without SDSN can be calculated using the MLE estimator by substituting $\zeta = 0$ in (4.7), and thus it can be written as

$$\hat{d}^{-\alpha} = \frac{1}{c}\sum_{i=1}^{N}\frac{r_i}{x_i}. \tag{4.26}$$

  This result is widely acknowledged in the literature, affirming the validity of our work.

4.5 Simulation Results and Discussion

This section presents the numerical performance of SISO-VLP systems under SDSN for range estimation between the transmitter and PD using MLE, NLS, and EKF techniques.

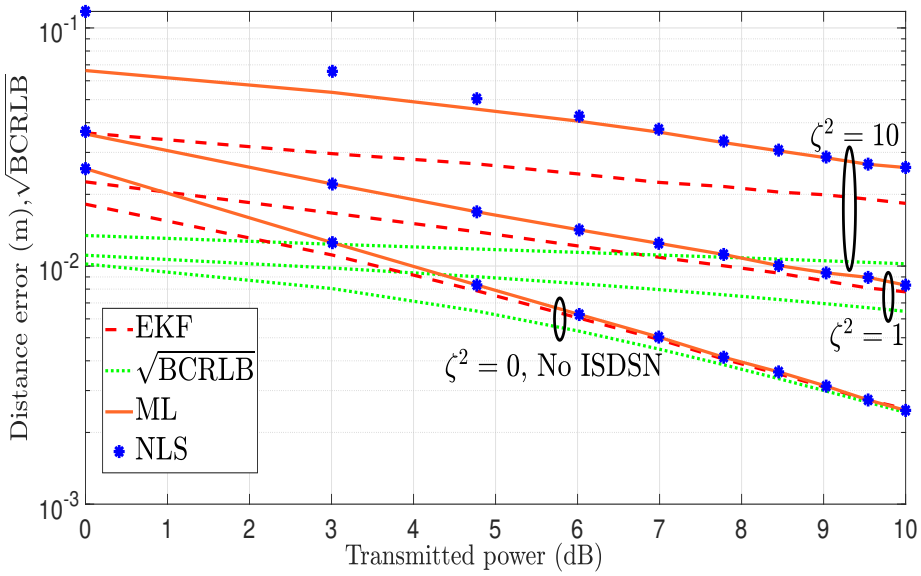

Figure 4.2: Comparing the distance error of ML, NLS, and EKF estimators and $\sqrt{\text{BCRLB}}$ at different ζ^2 values.

Simulations are conducted in MATLAB, with results derived from approximately 10^6 Monte Carlo iterations per figure. Furtermore, the simulation parameters are given as $\phi_{\text{FOV}} = 70°$, $L = 3m$, $A_{pd} = 0.1m^2$, $T_s(\theta_{rx}) = 1$, $g(\theta_{rx}) = 1$ and $\eta = 0.4$ A/Watt. Aditionally, we assume $\sigma_n^2 = 10^{-2}, \sigma_u^2 = 10^{-3}$ and $\gamma = 0$ unless otherwise specified.

In Fig. 4.2, the root mean square error (RMSE) for the estimated distance $\hat{d}$ is plotted against the transmitted power from the source. This Figure illustrates the impact of SDSN on MLE, NLS, and EKF estimation methods, as well as the($\sqrt{\text{BCRLB}}$). When the SDSN noise variance ζ^2 increases, the RMSE for all estimation methods rises accordingly. Notably, the $\sqrt{\text{BCRLB}}$ values also increase with increasing ζ^2, consistent with the inverse of (4.21). Furthermore, the EKF demonstrates superior performance in terms of error reduction compared to the MLE and NLS estimators, particularly at high ζ^2 values. Moreover, when $\zeta^2 = 0$, The RMSE of the estimator decreases with increasing power to align with

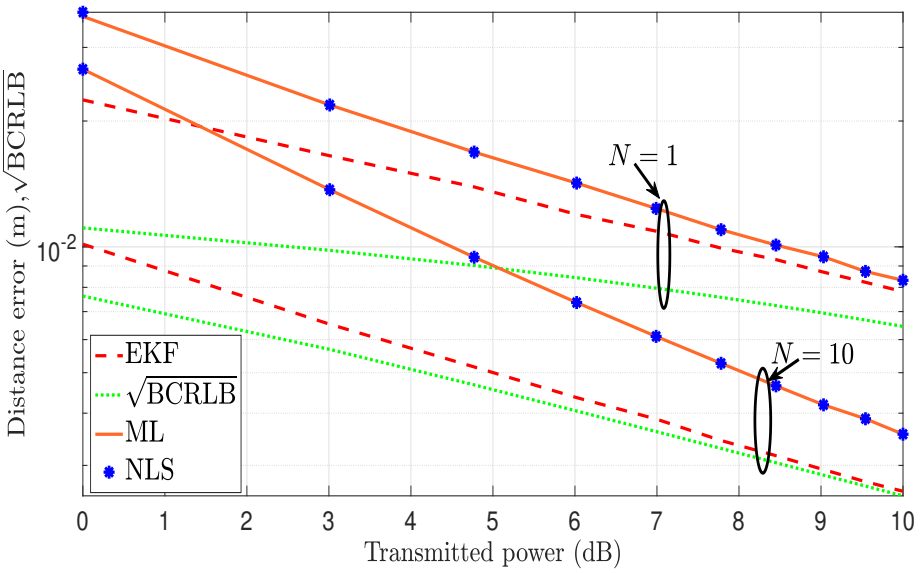

Figure 4.3: $\sqrt{\text{BCRLB}}$ and distance error of the ML, NLS, and EKF estimators at different numbers of pilots for $\zeta^2 = 1$.

$\sqrt{\text{BCRLB}}$. At high power levels, when $\zeta^2 = 0$, the variance of the NLS estimator becomes equal to the BCRLB This behavior is consistent with (4.13) and (4.24). It is important to note that from this figure, the EKF has a higher time complexity compared to the other estimators because it is a recursive technique. However, it offers better performance at high SDSN values, effectively mitigating the noise. For small signal-dependent noise values and to reduce complexity, the NLS or MLE estimators can be used, as they provide RMSE values close to those of the EKF.

Fig.4.3 discusses the effect of increasing the number of pilots N on the performance of MLE, NLS, EKFestimators and $\sqrt{\text{BCRLB}}$, where the value of $\zeta^2 = 1$. The figure clearly shows that as the number of pilots grows, the error in distance estimation decreases, which is compatible with the mathematical results. From this figure, we can see that at high power and a large number of pilots EKF RMSE and $\sqrt{\text{BCRLB}}$ become the same, which

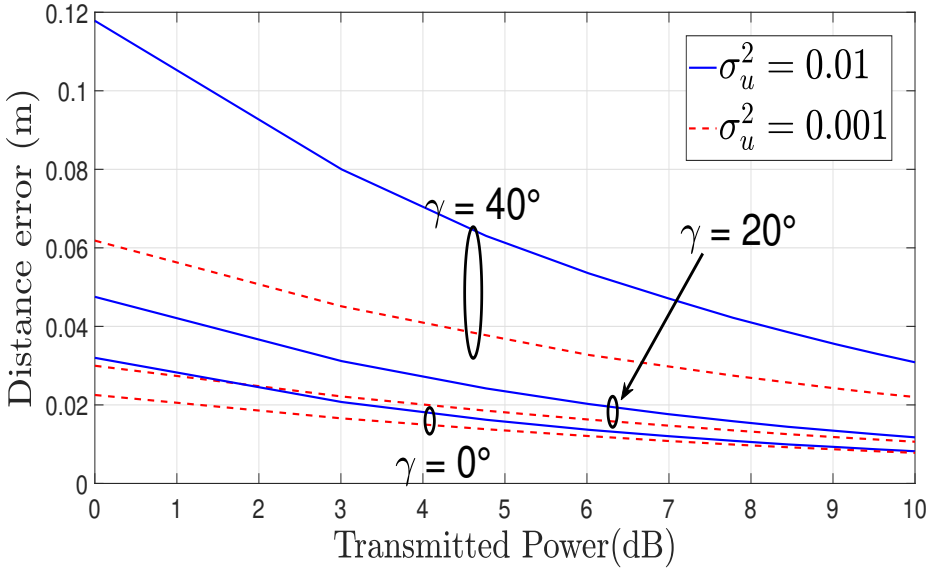

Figure 4.4: The impact of tilting angle on the RMSE of the EKF estimator for $\zeta^2 = 1$ and different valus of uncertainty noise variance σ_u^2.

is not the case in MLE and NLS estimators. This finding can be explained by the fact that EKF tracks the range of a sequence of time iterations and these prior measurements enhance the performance of EKF.

Fig.4.4 examines the impact of the receiver's tilting angle and uncertainty noise on the performance of the EKF estimator at $\zeta^2 = 1$, though this analysis is applicable for any value of ζ. The figure demonstrates that as the tilting angle of the receiver rises, the error of the estimated distance also rises. Similarly, when the uncertainty noise variance σ_u^2 grows, the distance error also grows. This rise in error due to the tilting angle occurs because the receiver plane does not face the transmitter, reducing the performance of the estimation and decreasing the amount of received signal, consistently with (4.3) and (4.4).

4.6 Conclusion

This chapter focuses on estimating the range of a user from a light source within a SISO framework, addressing the influence of SDSN. To achieve this, EKF, MLE, and NLS Estimator techniques were utilized. Simulations show that EKF outperforms MLE and NLS estimation. When the SDSN noise level approaches zero, the outcomes of all estimators converge, becoming the same at higher power settings.

Additionally, we derived the BCRLB in the presence of SDSN to benchmark the performance of our estimators. The results indicate that the BCRLB value decreases as the number of pilot symbols and transmitted power increases. Furthermore, at lower SDSN values, the BCRLB and EKF estimates converge, becoming closely aligned.

As a potential future direction, the range estimation problem can be extended by studying the impact of random receiver orientation. Incorporating orientation uncertainty would more closely reflect realistic deployment scenarios, where the photodetector may not always be perfectly aligned with the transmitter, and could reveal additional challenges for estimator design.

4.7 Publications Resulted from This Chapter

- S. H. ElFar et al., "Insights into Visible Light Positioning: Range Tracking and Bayesian Cramér-Rao Lower Bound Analysis," *IEEE Communications Letters*, vol. 28, no. 9, pp. 2056-2060, Sept. 2024.
- M. Yaseen, S. H. ElFar, and S. Ikki, "Machine Learning-Based Channel Estimation in Visible Light Communication," *IEEE MECOM conference*, pp. 263-267, 2024.

Chapter 5

Tracking and Positioning Dynamic Targets in VLC: Signal Dependent Noises and Bayesian Bound Analysis

5.1 Introduction

This chapter investigates the problem of position estimation and tracking in indoor VLC systems under a MISO configuration. The study specifically addresses the impact of SDSN and RIN, which significantly degrade localization accuracy in practical VLC scenarios. To establish a theoretical performance benchmark, a novel closed-form BCRLB is derived for 2D position estimation. The proposed EKF demonstrates superior localization accuracy by effectively accounting for motion dynamics through its recursive updates, unlike estimation methods that rely solely on noisy distance measurements. Our findings show that increasing the number of light sources improves spatial diversity, thereby enhancing positioning

precision. Furthermore, analysis indicates that RIN has a more pronounced negative effect on tracking accuracy than SDSN. The EKF's performance is validated against the proposed BCRLB, confirming its suitability for real-time and reliable indoor localization. Overall, this work provides meaningful insights into the design of robust and efficient VLC-based positioning systems.

5.1.1 Related Work

In VLP systems, several algorithms have been developed, each with distinct advantages and limitations. Proximity-based methods are simple and low-cost but offer limited accuracy. ToA, TDoA, and AoA techniques provide higher accuracy but require multiple LEDs, time synchronization, and complex hardware. Fingerprinting and image-sensing methods deliver high accuracy with fewer LEDs but suffer from poor portability and slower response. Hybrid methods improve robustness by combining techniques, but increase system complexity. In this work, we adopt the RSS-based approach due to its simplicity and low cost. However, since it relies on the channel model, we implement recursive estimation techniques to achieve robust positioning accuracy in localization and tracking [81], [10].

The authors in [82] presented and validated an AoA-based VLP system using a specific type of receiver, a quadrant solar cell (QSC). To enhance localization accuracy, they integrated third-orderridge regression machine learning (RRML) with the QSC. Experimental results demonstrated that the root-mean-square (RMS) of the average position error was reduced from 7.2177 cm to 3.2025 cm using third-order regression and further improved to 3.0881 cm with the proposed third-order RRML. This approach highlights the potential of combining AoA techniques with machine learning; however, it also relies on specialized hardware, which may limit system generalizability and increase implementation cost.

While in [83], the AoA estimators with PDs were used to accurately determine beacon LED positions in VLP systems, improving localization accuracy by mitigating errors from imprecise LED placements. AoA algorithms determine the receiver's position by utilizing the estimated signals' arrival angles from multiple light sources. Consequently, these algorithms are susceptible to the accuracy of the estimated angles, which can greatly influence their overall accuracy.

Authors in [84] present a VLP system combining a passive time of flight (ToF) camera with field- programmable gate array (FPGA) modulated LEDs, using AoA and TDoA algorithms for accurate indoor localization. In [85], a ToA-based system is proposed for smartphone positioning using modulated LEDs and acoustic signals. Both studies focus on experimental setups and do not provide analytical performance models or consider SDSN or RIN. Similarly, [86] applied a ToA scheme for user localization and synchronization in a periodic asymmetric ranging network, where a primary anchor node transmitted signals and secondary nodes received them.

To address the limitations and complexity of AoA and ToA techniques, the RSS method has been proposed and is widely utilized. This approach estimates the user's location based on the power of the received signal, as RSS is considered a straightforward and efficient localization technique. In [87], authors used a VLP implementation to estimate the position of a vehicle in a room using the RSS scheme and fixed LED-based light transmitters. In [88], the authors proposed a camera-assisted RSS algorithm for VLP systems to improve the accuracy of the positioning of the user. Moreover, in [89], an iterative least squares algorithm is introduced for static indoor VLP based on RSS, with consideration of SDSN. Nonetheless, the framework does not include the impact of RIN, nor does it address dynamic VLP scenarios involving time-varying receiver positions. Although many studies in the literature have studied the localization of a user using VLP, no work

has considered studying the effect of the joint presence of SDSN and RIN.

Recently, a number of studies have applied the EKF to enhance VLP. For instance, [90] proposes an EKF-based solution for PD-based VLP, where the measurement model incorporates Lambertian emission characteristics and geometric constraints. Similarly, [91] improves RSS-based localization by combining temporal averaging with Kalman filtering to reduce measurement variability. In [92], a fusion framework integrates VLP measurements with inertial navigation using EKF to maintain continuous tracking even in the presence of LED signal blockage and multipath effects. More recently, [93] introduces a joint position and orientation estimation scheme that fuses angle and distance information from multiple LEDs within an EKF framework, achieving improved accuracy in dynamic environments. Despite their contributions, these studies do not consider the effect of signal-dependent noise, such as SDSN and RIN, which are inherent in optical wireless systems and can substantially impact tracking performance. Furthermore, none of these works provides a mathematical benchmark like the BCRLB, which is essential for evaluating the theoretical accuracy limits of estimators, especially in recursive systems such as those relying on EKF.

A rigorous theoretical framework, such as the CRLB, is essential for analyzing and optimizing tracking performance in VLP systems. This framework provides a benchmark to assess the limits of accuracy and guide the development of more effective positioning techniques. A closed-form CRLB for the user location and orientation of NLoS propagation on the RSS-based VLP was derived in [94]. While in [95], the CRLB of the positioning error of a hybrid RF-VLC and positioning system using the RSS measurement method for positioning was derived. In [96], the authors derived the CRLB for the integrated visible light positioning and communication (VLPC) system using an RSS-based 3D positioning scheme. To the best of the authors' knowledge, there is no work in the literature that considers the derivation of the BCRLB for location error in the presence of SDSN and RIN

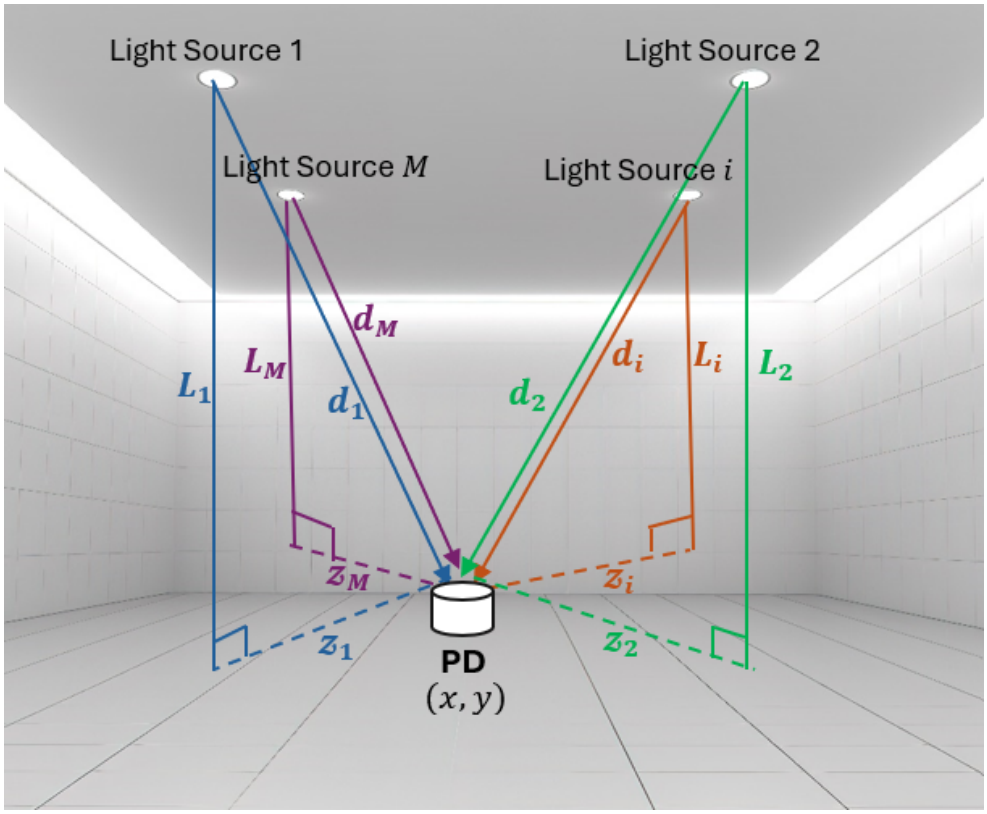

Figure 5.1: Visible light positioning system model

in a VLP system.

5.2 System And Channel Model

We consider an indoor MISO VLP system consisting of M light sources fixed on a room's ceiling, serving a single user equipped with a PD, as shown in Fig. 5.1. We assume that the user moves with a known velocity $\mathbf{v}$. Each light source transmits a visible light signal to the PD. The transmitted signal from each source is denoted as x, and, without loss of generality, we assume that all sources transmit with the same power, thus $x = p > 0$ [97].

The received signal vector $\boldsymbol{r} = [r_1, r_2, \cdots, r_i, \cdots, r_M]^T$ can be expressed as:

$$\mathbf{r} = \underbrace{\mathbf{h}x}_{\text{Signal}} + \underbrace{\sqrt{x\ \text{diag}(\mathbf{h})}\ \mathbf{n}_{\text{ds}}}_{\text{SDSN}} + \underbrace{x\ \text{diag}(\mathbf{h})\ \mathbf{n}_R}_{\text{RIN}} + \underbrace{\mathbf{n}}_{\text{Thermal Noise}}, \tag{5.1}$$

where M is the number of transmitted light sources, diag($\mathbf{h}$) is an $M \times M$ diagonal matrix with the elements of the channel gain vector $\mathbf{h} = [h_1, h_2, \cdots, h_i, \cdots, h_M]^T$ on the main diagonal. The noise terms are as follows: $\mathbf{n} = [n_1, n_2 \cdots, n_i, \cdots, n_M]^T$, is the thermal noise and SDSN vector is $\mathbf{n}_{ds} = [n_{ds1}, n_{ds2}, \cdots, n_{dsi}, \cdots, n_{ds_M}]^T$ and finally RIN $\mathbf{n}_R = [n_{R_1}, n_{R_2}, \cdots, n_{R_i}, \cdots, n_{R_M}]^T$ [98], [99].

The elements of $\mathbf{n}$ are independent and identically distributed Gaussian random variables, i.e., $\mathbf{n} \sim \mathcal{N}(0, \sigma_n^2 \mathbf{I}_M)$. Similarly, we have $\mathbf{n}_{ds} \sim \mathcal{N}(0, \sigma_{ds}^2 \mathbf{I}_M)$ and $\mathbf{n}_R \sim \mathcal{N}(0, \sigma_R^2 \mathbf{I}_M)$. The channel gain h_i between the ith light source and the user can be expressed as [18]:

$$h_i = \frac{A_{pd_i} \eta_i (m_i + 1)}{2\pi d_i^2} \cos_i^m(\phi_{tx_i}) T_s(\theta_{rx_i}) g(\theta_{rx_i}) \cos(\theta_{rx_i}), \tag{5.2}$$

where d_i is the Euclidean distance from the transmitter light source to the receiver, which can be calculated as $d_i = \sqrt{L^2 + z_i^2}$, where L corresponds to the vertical distance from the i^{th} light source to the PD surface, and z_i is the horizontal distance from the center of the light source cell to the PD, as illustrated in Fig.5.2, and ϕ_{tx_i} represents the angle of irradiance. It's worth mentioning that $\cos(\phi_{tx_i}) = \cos(\theta_{rx_i}) = \frac{L}{d_i}$, in the case when the receiver is oriented upwards and the transmitter is directed downwards, θ_{rx_i} signifies the angle of incidence surface, $T_s(\theta_{rx_i})$ stands for the gain associated with the receiver's optical filter, $g(\theta_{rx_i}) = n_i^2 / \sin^2(\phi_{\text{FOV}_i})$ describes the gain of the optical concentrator, which relies on the refractive index n_i of the concentrator and the FoV angle, i.e., ϕ_{FOV_i}. It's important to note that $g(\theta_{rx_i}) = 0$ when $\theta_{rx_i} > \phi_{\text{FOV}_i}$ [53], [100]. Additionally, A_{pd_i} denotes

the detection area of the PD and η represents the average responsivity of the receiver and finally $m_i = \frac{-1}{\log_2(\cos(\Phi_{i_{1/2}}))}$ is the Lambertian radiation order and is determined by the light source emission semi-angle $\Phi_{i_{1/2}}$.

Hence, the received signal vector can be rewritten as

$$\boldsymbol{r} = (\boldsymbol{c} \odot \boldsymbol{\beta})p + \sqrt{\text{diag}(\boldsymbol{c} \odot \boldsymbol{\beta})p}\boldsymbol{n_{ds}} + \text{diag}(\boldsymbol{c} \odot \boldsymbol{\beta})p\boldsymbol{n_R} + \boldsymbol{n}, \tag{5.3}$$

where $\boldsymbol{\beta} = [d_1^{-\alpha}, d_2^{-\alpha}, \cdots, d_i^{-\alpha}, \cdots, d_M^{-\alpha}]^T$, $\odot$ is the Hadamard product operator Assuming a constant $\boldsymbol{c} = [c_1, c_2, \cdots, c_i, \cdots, c_M]^T$, calculated as

$$c_i = \frac{A_{pd_i}\eta_i(m_i+1)}{2\pi} L^{m_i+1} T_s(\theta_{rx_i}) g(\theta_{rx_i}), \tag{5.4}$$

where $\alpha = m+3$. It's worth noting that the distortion variance is directly influenced by the distance between the transmitter and the receiver. This sets the additive distortion term apart from conventional receiver noise, which remains independent of distance. It is worth mentioning that in the ideal case, the received signal can be written as $\boldsymbol{r} = (\boldsymbol{c} \odot \boldsymbol{\beta})p + \boldsymbol{n}$.

5.3 PD Transition Model and Bayesian Cramér-Rao Lower Bound

In this section, we consider a PD moving in a 2D x-y plane. Since the PD's position changes over time, all measurements become time-dependent. We also present a closed-form expression for the BCRLB, which serves as a fundamental performance benchmark for position estimation under dynamic conditions. Because the estimation depends on the PD's motion over time, the BCRLB must be updated recursively as the PD's position

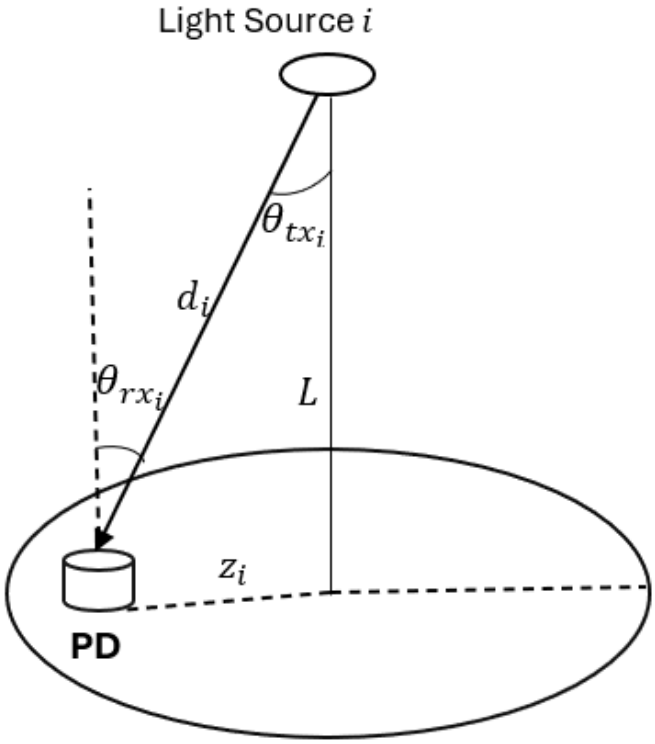

Figure 5.2: Visible light communication channel model

changes.

To derive the BCRLB, we first determine the Fisher information matrix (FIM) of the estimated distances, referred to as the distance Fisher information matrix (DFIM). Using the DFIM, we determined the FIM for the PD's position, denoted as the position Fisher information matrix (PFIM). Finally, with the PFIM in hand and incorporating the PD's dynamic motion, we are ultimately able to compute the time-varying BCRLB. To the best of the authors' knowledge, the previous bounds have not been determined, even for the ideal case, i.e., without SDSN and RIN.

5.3.1 PD Transition Model

In this subsection, we outline the mathematical model for the motion of PD within an indoor environment illuminated by multiple light source transmitters. While the PD moves, its position may experience slight deviations from the ideal path due to interactions with environmental obstacles and objects. The PD collects distance measurements from the light source transmitters at uniform intervals of Δ seconds, and these measurements are utilized to model and analyze its dynamic position over time [101], [102].

For the 2D motion model, the position of the PD at the t-th sample can be expressed as: $\mathbf{P}[t] = [x[t]\ ,\ y[t]]^T \in \mathbb{R}^2$. Therefore, the transition model governing the motion of the PD can be written as:

$$\mathbf{P}[t] = \mathbf{P}[t-1] + \mathbf{q}[t] + \mathbf{u}[t], \tag{5.5}$$

where $\mathbf{q}[t]$ denotes the control input associated with motion under time-varying velocity, defined as: $\mathbf{q}[t] = \Delta\mathbf{v}[t-1] + \frac{1}{2}\mathbf{a}\Delta^2$, with $\mathbf{v}[t] = [v_x[t], v_y[t]]^T$representing the velocity of the PD in the 2D $x-y$ plane and $\mathbf{a} = [a_x, a_y]^T$ denoting the acceleration [103]. The term $\mathbf{u}[t]$ captures random perturbations in the motion due to unexpected environmental factors.

The process noise $\mathbf{u}[t]$ is modeled as a Gaussian random vector with zero mean and covariance matrix $\boldsymbol{Q}$, such that:

$$\mathbf{u}[t] \sim \mathcal{N}(0, \boldsymbol{Q}). \tag{5.6}$$

For simplicity, assume that $\boldsymbol{Q} = \left[\sigma_x^2\ ,\ \sigma_y^2\right]^T$, where σ_x^2 and σ_y^2 denote the variances of the noise along the x and y axes, respectively. For any two samples $t \neq t'$, the process noise vectors $\boldsymbol{u}[t]$ and $\boldsymbol{u}[t']$ are independent, ensuring that:

$$E[\boldsymbol{u}[t]\ \ \boldsymbol{u}^\top[t']] = 0 \text{ for } t \neq t'. \tag{5.7}$$

This independence implies that $\boldsymbol{u}[t]$ is a vector of additive white Gaussian noise [104], [79]. Because the noise vectors are independent across time, the position sequence $\boldsymbol{P}[t]$ forms a Markov chain. As a result, this Markov property can be formulated as:

$$p(\boldsymbol{P}[t] \mid \boldsymbol{P}[0:t-1]) = p(\boldsymbol{P}[t] \mid \boldsymbol{P}[t-1]), \tag{5.8}$$

indicating that the conditional probability of the PD's position at time t depends only on its immediate previous state at time $t-1$. By leveraging the Gaussian nature of $\boldsymbol{u}[t]$, this conditional probability distribution is given by:

$$p(\boldsymbol{P}[t] \mid \boldsymbol{P}[\boldsymbol{t-1}]) \sim \mathcal{N}(\boldsymbol{P}[t-1] + \mathbf{q}[t], \boldsymbol{Q}). \tag{5.9}$$

In terms of the initial conditions, the initial state of the position $\mathbf{P}[-1]$ is independent of $\mathbf{u}[t]$ and follows a Gaussian distribution:

$$\mathbf{P}[-1] \sim \mathcal{N}(\mathbf{P}_0 + \mathbf{q}_0, \mathbf{Q}_0). \tag{5.10}$$

Here, $\mathbf{P}_0$, $\mathbf{Q}_0$, and $\mathbf{q}_0$ can be selected arbitrarily or derived from prior knowledge. These initial values are then provided as inputs to the EKF, as we will describe in the subsequent section. As the number of samples increases, the effect of the initial conditions becomes negligible [36, 105].

5.3.2 Distance Fisher Information Matrix (DFIM)

To establish a fundamental benchmark for dynamic position estimation, first, we derive DFIM based on the received signal, denoted as $\boldsymbol{J}_d^{(O)}[t]$. The DFIM quantifies the relationship between the information contained in the received signal and the distances between

the transmitting light source and the PD receiver. The matrix can be expressed as follows:

$$\mathbf{J}_{\mathbf{d}}^{(\mathrm{O})}[t] = -\mathbb{E}\left[\frac{\partial^2}{\partial \boldsymbol{d}[t]\partial \boldsymbol{d}[t]^T}\ln f(\boldsymbol{r}[t]|\boldsymbol{d}[t])\right], \tag{5.11}$$

where $\mathbb{E}[\cdot]$ is the expectation operator and $\mathbf{r}[t]$ is a M-dimensional Gaussian random vector with mean vector $\boldsymbol{\mu}[t] = (\mathbf{c} \odot \boldsymbol{\beta}[t])\, p$, where $\mathbf{c}$ and $\boldsymbol{\beta}[t]$ are system-specific parameters, and covariance matrix $\boldsymbol{\Sigma}_s[t] = \mathrm{diag}\,[\sigma_{s1}^2[t], \ldots, \sigma_{si}^2[t], \ldots, \sigma_{sM}^2[t]]$, where each variance term is $\sigma_{si}^2[t] = \sigma_{n_i}^2 + \sigma_{ds_i}^2\, c_i\, p_i\, d_i[t]^{-\alpha} + \sigma_{R_i}^2\, c_i^2\, p_i^2\, d_i[t]^{-2\alpha}$, representing the variance of the i-th observation, it follows that: $\mathbf{r}[t] \sim \mathcal{N}(\boldsymbol{\mu}[t], \boldsymbol{\Sigma}_s[t])$.

The probability density function (PDF) of $\boldsymbol{r}[t]$ conditioned on $\boldsymbol{d}[t]$ can be depicted as:

$$f(\boldsymbol{r}[t] \mid \boldsymbol{d}[t]) = \frac{1}{(2\pi)^{\frac{M}{2}}\,|\boldsymbol{\Sigma}_s[t]|^{1/2}} \exp\!\big(-\tfrac{1}{2}(\boldsymbol{r}[t]-\boldsymbol{\mu}[t])^T \boldsymbol{\Sigma}_s[t]^{-1}(\boldsymbol{r}[t]-\boldsymbol{\mu}[t])\big)\,. \tag{5.12}$$

Therefore, the DFIM ($\mathbf{J}_{\mathbf{d}}^{(\mathrm{O})}[t]$) is an $M \times M$ matrix, and each element in it can be computed as:

$$\mathrm{J}_{d}^{(\mathrm{O})}[t]_{(i,j)} = \frac{\partial \boldsymbol{\mu}[t]^T}{\partial d_i[t]} \boldsymbol{\Sigma}_s[t]^{-1} \frac{\partial \boldsymbol{\mu}[t]}{\partial d_j[t]} + \tfrac{1}{2}\,\mathrm{tr}\left(\boldsymbol{\Sigma}_s[t]^{-1} \frac{\partial \boldsymbol{\Sigma}_s[t]}{\partial d_i[t]} \boldsymbol{\Sigma}_s[t]^{-1} \frac{\partial \boldsymbol{\Sigma}_s[t]}{\partial d_j[t]}\right). \tag{5.13}$$

where tr(.) is the trace operator, and the derivatives of the mean and covariance matrix are given as follows:

$$\frac{\partial \boldsymbol{\mu}[t]}{\partial d_i[t]} = \big[\,0, \ldots, -p\alpha c_i d_i[t]^{-(\alpha+1)}, \ldots, 0\,\big]^\top, \tag{5.14}$$

$$\frac{\partial \boldsymbol{\Sigma}_s[t]}{\partial d_i[t]} = \mathrm{diag}\Big[0, \ldots, \Big(-\alpha\sigma_{ds_i}^2 c_i p_i d_i[t]^{-(\alpha+1)} - 2\alpha\sigma_{R_i}^2 c_i^2 p_i^2 d_i[t]^{-2(\alpha+1)}\Big), \ldots, 0\Big], \tag{5.15}$$

$$\boldsymbol{\Sigma}_s[t]^{-1} = \mathrm{diag}\left[\frac{1}{\sigma_{s1}^2[t]}, \ldots, \frac{1}{\sigma_{si}^2[t]}, \ldots, \frac{1}{\sigma_{sM}^2[t]}\right]. \tag{5.16}$$

Finally, after subsisting the derived expressions and the inverse covariance matrix $\mathbf{\Sigma}_s[t]^{-1}$ into (5.13), then carrying out the necessary summations and algebraic manipulations, we obtain the full expression of each element of DFIM ($\mathrm{J}_d^{(\mathrm{O})}[t]_{i,j}$). It is worth mentioning that this matrix is diagonal due to the statistical independence between the estimated distances, and its elements can be calculated as:

$$\mathrm{J}_d^{(\mathrm{O})}[t]_{(i,i)} = \frac{p^2 c_i^2 \alpha^2 d_i[t]^{-2(\alpha+1)}}{\sigma_{si}^2[t]} + \frac{1}{2}\frac{\big(-\sigma_{dsi}^2 c_i p \alpha d_i[t]^{-(\alpha+1)} - 2\sigma_{Ri}^2 c_i^2 p^2 \alpha d_i[t]^{-(2\alpha+1)}\big)^2}{\sigma_{si}^4[t]}. \quad (5.17)$$

The following remarks provide a deeper understanding of how noise and various parameters in (5.17) influence the calculation of the DFIM.

Remark 1: As the distance $d_i[t]$ increases, the value of $\mathrm{J}_d^{(\mathrm{O})}[t]_{(i,i)}$ decreases, resulting in a reduction of the corresponding diagonal element of the DFIM. Therefore, a reduction in the element of DFIM corresponds to an increase in the variance of the distance estimation error. This means that the accuracy of the estimated distance decreases as the PD moves farther away from the light source.

Remark 2: When $\sigma_{Ri}^2 = 0$ and $\sigma_{dsi}^2 = 0$, i.e., ideal case, for all estimated distances, the value of the corresponding diagonal elements of DFIM increases proportionally to the square of the transmitted power, as given by $\mathrm{J}_d^{(\mathrm{O})}[t]_{(i,i)} = \frac{p^2 c_i^2 \alpha^2 d_i[t]^{-2(\alpha+1)}}{\sigma_{ni}^2}$. In this scenario, the dominant noise source is thermal noise, which is independent of the transmitted signal's power. Therefore, increase in transmitted power can lead to higher estimation accuracy.

Remark 3: In (5.17), the expression for $\mathrm{J}_d^{(\mathrm{O})}[t]_{(i,i)}$ under the condition $\sigma_{Ri}^2 \to \infty$ simplifies to , $\lim_{\sigma_{Ri}^2 \to \infty} \mathrm{J}_d^{(\mathrm{O})}[t]_{(i,i)} = 2\alpha^2 d_i[t]^{-2}$ This indicates that, in the presence of high RIN, $\mathrm{J}_d^{(\mathrm{O})}[t]_{(i,i)}$ primarily depends on the distance between the transmitter and receiver and the material of the receiver. The influence of transmitted power becomes negligible, leading to a saturation level as the power increases.

Remark 4: In this scenario, taking the limit as power p tends to infinity: $\lim_{p\to\infty} \mathrm{J}_d^{(\mathrm{O})}[t]_{(i,i)} = \alpha^2 d_i[t]^{-2}\left(\frac{1}{\sigma_{Ri}^2}+2\right)$. if this happens to all measured distances in DFIM. This implies that the diagonal elements of DFIM reach a saturation level where its value depends on both σ_{Ri}^{-2} and the distance. Even with unlimited power, the impact of σ_{Ri}^2 remains significant. As σ_{Ri}^2 grows large, the system settles at this saturation point, rendering any further increase in power inconsequential.

Remark 5: In (5.17), when $\sigma_{dsi}^2 \to \infty$, the expression for $\mathrm{J}_d^{(\mathrm{O})}[t]_{(i,i)}$ simplifies to $\lim_{\sigma_{dsi}^2\to\infty} \mathrm{J}_d^{(\mathrm{O})}[t]_{(i,i)} = \frac{1}{2}\alpha^2 d_i[t]^{-2}$. This indicates that in cases dominated by σ_{dsi}^2 if we apply the same condition to all distances, the diagonal elements of DFIM become dependent on the distance and fabrication material of the receiver only.

Remark 6: In (5.17), when $\sigma_{Ri}^2 \to 0$, and $p \to \infty$ the expression for $\mathrm{J}_d^{(\mathrm{O})}[t]_{(i,i)}$ is simplified to $\mathrm{J}_d^{(\mathrm{O})}[t]_{(i,i)} = \frac{pc_i\alpha^2 d_i[t]^{-(\alpha+2)}}{\sigma_{dsi}^2} + \frac{1}{2}\alpha^2 d_i[t]^{-2}$. This result demonstrates that in the absence of σ_{Ri}^2 and as $p \to \infty$, the value of the corresponding diagonal elements of DFIM increases linearly with p. Additionally, in the same equation when $\sigma_{dsi}^2 \to 0$, and $p \to \infty$ the expression for $\mathrm{J}_d^{(\mathrm{O})}[t]_{(i,i)}$ is simplified to $\mathrm{J}_d^{(\mathrm{O})}[t]_{(i,i)} = \alpha^2 d_i[t]^{-2}(2+\frac{1}{\sigma_{Ri}^2})$.This result demonstrates that in the absence of σ_{dsi}^2 and as $p \to \infty$, the value of the corresponding diagonal elements of DFIM reaches an instant saturation level, and increasing power does not affect them. However, as discussed in Remark 2, when both $\sigma_{Ri}^2 \to 0$ and $\sigma_{dsi}^2 \to 0$, the diagonal elements of DFIM increase proportionally with p^2.

5.3.3 Position Fisher Information Matrix (PFIM)

Since our goal is to estimate the position of a dynamic PD we have derived a PFIM. This calculation is carried out by utilizing the DFIM and the known relationship between the measured distances and the x-y coordinates of the target. Specifically, each measured

distance is related to the target's position by $d_i[t] = \sqrt{(x[t]-x_i)^2+(y[t]-y_i)^2}$. The PFIM of the target position, denoted as $\mathbf{J_P}^{(\mathrm{O})}[t]$, has dimensions 2×2. To bridge the gap between the DFIM and the PFIM, we introduce the Jacobian matrix $\mathbf{T}[t]\in\mathbb{R}^{2\times M}$, which captures how variations in the target's x-y coordinates affect the measured distances and is defined as:

$$\mathbf{J}_{\mathbf{P}}^{(\mathrm{O})}[t] = \mathbf{T}[t]\mathbf{J}_{\mathbf{d}}^{(\mathbf{O})}[t]\mathbf{T}[t]^T, \tag{5.18}$$

$$\mathbf{T}[t] = \frac{\partial \mathbf{d}^T[t]}{\partial \mathbf{P}[t]} = \begin{bmatrix} \frac{\partial d_1[t]}{\partial x[t]} & \cdots & \frac{\partial d_i[t]}{\partial x[t]} & \cdots & \frac{\partial d_M[t]}{\partial x[t]} \\ \frac{\partial d_1[t]}{\partial y[t]} & \cdots & \frac{\partial d_i[t]}{\partial y[t]} & \cdots & \frac{\partial d_M[t]}{\partial y[t]} \end{bmatrix}, \tag{5.19}$$

where the partial derivatives with respect to x and y are given by:

$$\frac{\partial d_i[t]}{\partial x[t]} = \frac{(x[t]-x_i)}{\sqrt{(x[t]-x_i)^2+(y[t]-y_i)^2}}, \tag{5.20}$$

$$\frac{\partial d_i[t]}{\partial y[t]} = \frac{(y[t]-y_i)}{\sqrt{(x[t]-x_i)^2+(y[t]-y_i)^2}}. \tag{5.21}$$

After that substitute values of $\mathbf{T}[t]$, $\mathbf{J}_{\mathbf{d}}^{(\mathrm{O})}[t]$ in (5.18) the PFIM of location $\mathbf{J}_{\mathbf{P}}^{(\mathrm{O})}[t]$ can be expressed

$$\mathbf{J}_P^{(O)}[t] = \begin{bmatrix} \sum_{i=1}^{M} \mathrm{J}_d^{(\mathrm{O})}[t]_{(i,i)} \frac{(x-x_i)^2}{(x-x_i)^2+(y-y_i)^2} & \sum_{i=1}^{M} \mathrm{J}_d^{(\mathrm{O})}[t]_{(i,i)} \frac{(x-x_i)(y-y_i)}{(x-x_i)^2+(y-y_i)^2} \\ \sum_{i=1}^{M} \mathrm{J}_d^{(\mathrm{O})}[t]_{(i,i)} \frac{(x-x_i)(y-y_i)}{(x-x_i)^2+(y-y_i)^2} & \sum_{i=1}^{M} \mathrm{J}_d^{(\mathrm{O})}[t]_{(i,i)} \frac{(y-y_i)^2}{(x-x_i)^2+(y-y_i)^2} \end{bmatrix}. \tag{5.22}$$

Remark 7: PFIM in (5.22) depends on the number of light sources, M. As the number of light sources increases, more terms are added to the summation, increasing the PFIM and, consequently, decreasing the CRLB of the estimated position. This implies that increasing M improves the accuracy of position estimation. It is worth mentioning that the

minimum number of light sources is three; otherwise, the PFIM becomes singular, making it impossible to determine the CRLB matrix. In other words, the position estimation cannot be performed.

5.3.4 Bayesian Cramér-Rao Lower Bound (BCRLB)

The recursive or BCRLB is a theoretical performance limit on the accuracy of parameter estimates in dynamic, time-varying systems. Unlike the classical CRLB, which assumes fixed parameters and independent measurements, the BCRLB incorporates prior information and evolves as new measurements become available [40].

The Bayesian Fisher information matrix (BFIM) for the PD position tracking process, denoted as $\mathbf{J}_{\mathbf{P}}^{(\mathrm{B})}[t]$, is computed by combining the contributions from the measurement model in (5.18) and the prior information from dynamic motion in (5.5) can be calculated recursively as:

$$\mathbf{J}_{\mathbf{P}}{}^{(B)}[t] = \underbrace{\mathbf{J}_{\mathbf{P}}^{(\mathrm{O})}[t]}_{\text{Measurements}} + \underbrace{\mathbf{J}_{\mathbf{P}}{}^{(\mathrm{I})}[t]}_{\text{Priori Information}} . \tag{5.23}$$

And after extract $\mathbf{J}_P{}^{(\mathrm{I})}$ Priori part it can be expressed as:

$$\mathbf{J}_P^{(B)}[t] = \underbrace{\mathbf{J}_P^{(\mathrm{O})}[t]}_{\text{Measurements}} + \underbrace{\Big(\boldsymbol{G}_{22}[t] - \boldsymbol{G}_{21}[t]\big[\mathbf{J}_P^{(B)}[t-1] + \boldsymbol{G}_{11}[t]\big]^{-1}\boldsymbol{G}_{12}[t]\Big)}_{\text{Prior information}}, \tag{5.24}$$

where $\mathbf{J}_{\mathbf{P}}^{(\mathrm{I})}[t]$, quantifies the amount of useful information available for the tracking process based on the PD transition model. The $\boldsymbol{G}[t]$ matrices are related to $\mathbf{J}_{\mathbf{P}}{}^{(\mathrm{I})}[t]$ and are formally defined as:

$$\boldsymbol{G}_{ij}[t] = \mathbb{E}\left(-\frac{\partial^2 \log p(\mathbf{P}[t] \mid \mathbf{P}[t-1])}{\partial \mathbf{P}[t+i-2]\partial \mathbf{P}[t+j-2]^T}\right), \tag{5.25}$$

where $i, j = 1, 2$. Here, $p(\mathbf{P}[t] \mid \mathbf{P}[t-1])$ is the conditional probability of $\mathbf{P}[t]$ given $\mathbf{P}[t-1]$.

after detailed mathematical calculations, the quantities $\boldsymbol{G}_{11}[t]$, $\boldsymbol{G}_{12}[t]$, $\boldsymbol{G}_{21}[t]$, and $\boldsymbol{G}_{22}[t]$ can be derived and obtained as described in Appendix section. Hence $\boldsymbol{G}[t]$ are expressed as [68]:

$$\boldsymbol{G}_{11}[t] \in \mathbb{R}^{2\times 2} = \boldsymbol{Q}^{-1}, \tag{5.26a}$$

$$\boldsymbol{G}_{12}[t] \in \mathbb{R}^{2\times 2} = -\boldsymbol{Q}^{-1}, \tag{5.26b}$$

$$\boldsymbol{G}_{21}[t] \in \mathbb{R}^{2\times 2} = -\boldsymbol{Q}^{-1}, \tag{5.26c}$$

$$\boldsymbol{G}_{22}[t] \in \mathbb{R}^{2\times 2} = \boldsymbol{Q}^{-1}. \tag{5.26d}$$

Finally, the BCRLB for the position at the t-th sample is determined by calculating the inverse of the BFIM as defined in (5.23). Consequently, the Position error bound (PEB) which serves as a benchmark for the variance of the position estimation error at the time sample at the t-th sample is computed as follows:

$$\mathrm{PEB}[t] = \sqrt{\left[\mathbf{J}_{\boldsymbol{P}}^{(\mathrm{B})}[t]\right]^{-1}_{(1,1)} + \left[\mathbf{J}_{\boldsymbol{P}}^{(\mathrm{B})}[t]\right]^{-1}_{(2,2)}}. \tag{5.27}$$

Remark 8: As indicated by (5.24), the BFIM is affected by the process noise. When the process noise increases, the BFIM decreases which leads to an increase in the BCRLB. It is worth mentioning that as the measurements become less noisy, the contribution of the prior information decreases, and vice versa.

5.4 Position Estimation and Tracking

This section focuses on estimating and tracking the PD target's position in a MISO system featuring M transmitter light sources and a single PD receiver. It explores how the

measured distances from the light sources contribute to estimating the PD's location using various methods. Furthermore, this section describes how the EKF can track and estimate the PD location under varying noise conditions.

5.4.1 Distance Estimation

To determine the PD position, it is first necessary to estimate the distances between light sources and PD and we consider these distances as our measurements. At the t-th time sample, the true distances vector is defined as:

$$\mathbf{d}[t] = [d_1[t], d_2[t], \ldots, d_M[t]\,]^T. \tag{5.28}$$

To obtain the estimated distance from the $\mathbf{r}[t]$, this work adopts the MLE framework to estimate the distances, explicitly considering the impact of noise and the effect of signal-dependent noises during the estimation process. The estimation is obtained by maximizing the following cost function [77]:

$$\hat{\mathbf{d}}[t] = \underset{\mathbf{d}[t]}{\arg\max}\ \ln f(\mathbf{r}[t] \mid \mathbf{d}[t]), \tag{5.29}$$

where the log-likelihood function from (5.12) is expressed as:

$$\ln f(\mathbf{r}[t] \mid \mathbf{d}[t]) = -\frac{M}{2}\ln(2\pi) - \frac{1}{2}\ln\big|\mathbf{\Sigma}_s[t]\big| - \frac{1}{2}\big(\mathbf{r}[t] - \boldsymbol{\mu}[t]\big)^\top \mathbf{\Sigma}_s^{-1}[t]\big(\mathbf{r}[t] - \boldsymbol{\mu}[t]\big). \tag{5.30}$$

To estimate each an individual distance $d_i[t]$, the log-likelihood function is maximized by solving:

$$\frac{\partial \ln f(\mathbf{r}[t] \mid \mathbf{d}[t])}{\partial d_i[t]} = 0. \tag{5.31}$$

Due to the complexity of the resulting equations, finding a closed-form solution for $\hat{d}_i[t]$ is typically infeasible. Instead, numerical methods and computational tools, such as MATLAB, are employed to compute the solution efficiently.

5.4.2 Measurements Model

After estimating the distances we can assume the observation vector, $\hat{\mathbf{\Gamma}}[t]$, consists of the estimated distances:

$$\hat{\mathbf{\Gamma}}[t] = \left[\hat{d}_1[t], \dots \hat{d}_i[t], \dots, \hat{d}_M[t]\right]^\top. \tag{5.32}$$

The estimated distance vector $\hat{\mathbf{\Gamma}}[t]$ inherently contains noise and serves as an approximation of the true distance-vector $\mathbf{\Gamma}[t]$. The relationship between the estimated and true values is described as:

$$\hat{\mathbf{\Gamma}}[t] = \mathbf{\Gamma}[t] + \mathbf{w}[t], \tag{5.33}$$

where $\mathbf{w}[t] \in \mathbb{R}^{M\times 1}$ is the measurement noise vector at the t-th sample, with a covariance matrix $\mathbf{C}[\mathbf{t}]$, which quantifies the uncertainty in the estimation. Under a MLE framework, the variance of the estimation error for $d_i[t]$ typically approaches the CRLB. Thus, the CRLB serves as a valuable benchmark for evaluating how accurately $d_i[t]$ can be used to estimate position [104], [39]. Therefore, the covariance matrix $\mathbf{C}[t]$ can be expressed as:

$$\mathbf{C}[t] = \left(\mathbf{J}_{\mathbf{d}}^{(\mathbf{O})}[t]\right)^{-1}, \mathbf{C}[t] \in \mathbb{R}^{M\times M}, \tag{5.34}$$

where $\mathbf{J}_{\mathbf{d}}^{(\mathbf{O})}[t]$ is the DFIM, as derived in (5.17). Therefore, $\hat{\mathbf{\Gamma}}[t]$ can be expressed as:

$$\hat{\mathbf{\Gamma}}[t] \sim \mathcal{CN}\big(\mathbf{\Gamma}[t], \boldsymbol{C}[t]\big). \tag{5.35}$$

The estimated values, $\hat{\mathbf{\Gamma}}[t]$, are dependent on the postion state vector $\mathbf{P}[t]$ through a functional relationship:

$$\hat{\mathbf{\Gamma}}[t] = \mathbf{f}(\mathbf{P}[t]) + \mathbf{w}[t], \tag{5.36}$$

where $\mathbf{f}(\mathbf{P}[t])$ represents the mapping function that relates the postion vector $\mathbf{P}[t]$ to the true distances $\mathbf{\Gamma}[t]$ [106]. This model highlights how the underlying signal parameters influence the measurements. The estimation accuracy depends on the signal quality and the statistical properties of the noise vector $\mathbf{w}[t]$, both of which directly impact the subsequent tracking Processes [104].

5.4.3 Extended Kalman Filter (EKF)

Kalman filter is a widely used tool for sequentially estimating the states of dynamic systems under uncertainty. It is an optimal MMSE estimator when both the system dynamics and observation models are linear, and the noise is Gaussian. However, many real-world systems exhibit nonlinearities in the relationship between the state vector and the observations, making the standard Kalman filter inapplicable [80]. To address this, the EKF extends the Kalman filter framework to nonlinear systems by linearizing the nonlinear models around the current state estimate using a first-order Taylor expansion [107]. This linearization enables the EKF to approximate the estimation process for nonlinear systems, albeit with some loss in optimality.

In the tracking problem, the location vector $\mathbf{P}[t]$, representing the position of the system, evolves dynamically over time and is subject to process noise. The observations $\hat{\mathbf{\Gamma}}[t]$ depend nonlinearly on $\mathbf{P}[t]$, where $f(\mathbf{P}[t]) \in \mathbb{R}^{M\times 1}$. The EKF addresses this by approximating the nonlinear observation function $f(\mathbf{P}[t])$ with its first-order Taylor expansion around the current estimate $\hat{\mathbf{P}}[t|t-1]$. The Jacobian matrix of this linearized model,

denoted by $\mathbf{F}[t]$, is computed as [40], [80]:

$$\mathbf{F}[t] \in \mathbb{R}^{M\times 2} = \left.\frac{\partial f(\mathbf{P}[t])}{\partial \mathbf{P}[t]}\right|_{\mathbf{P}[t]=\hat{\mathbf{P}}[t|t-1]}. \tag{5.37}$$

The function $f(\mathbf{P}[t])$ is defined as:

$$f(\mathbf{P}[t]) = \begin{bmatrix} \sqrt{(x[t]-x_1)^2+(y[t]-y_1)^2} \\ \vdots \\ \sqrt{(x[t]-x_i)^2+(y[t]-y_i)^2} \\ \vdots \\ \sqrt{(x[t]-x_M)^2+(y[t]-y_M)^2} \end{bmatrix}. \tag{5.38}$$

The derivative with respect to $x[t]$ is:

$$\frac{\partial f_i(\mathbf{P}[t])}{\partial x[t]} = \frac{x[t]-x_i}{\sqrt{(x[t]-x_i)^2+(y[t]-y_i)^2}}. \tag{5.39}$$

Similarly, the derivative with respect to $y[t]$ is:

$$\frac{\partial f_i(\mathbf{P}[t])}{\partial y[t]} = \frac{y[t]-y_i}{\sqrt{(x[t]-x_i)^2+(y[t]-y_i)^2}}. \tag{5.40}$$

Consequently, the linearized version of the measurements equation in (5.36) can be given as:

$$\hat{\mathbf{\Gamma}}[t] = \mathbf{F}[t]\mathbf{P}[t] + \underbrace{\mathbf{w}[t]}_{\text{measurement error}} + \underbrace{\Big(f\big(\hat{\mathbf{P}}[t|t-1]\big) - \mathbf{F}[t]\hat{\mathbf{P}}[t|t-1]\Big)}_{\text{linearization error}}. \tag{5.41}$$

The EKF operates recursively through prediction and correction steps to refine the state estimate $\hat{\mathbf{P}}[t|t]$. In the prediction step, the state is forecasted using the previous estimate

as [79]:

$$\hat{\mathbf{P}}[t|t-1] = \hat{\mathbf{P}}[t-1|t-1] + \mathbf{q}[t|t-1], \tag{5.42}$$

and the error covariance matrix is updated as:

$$\mathbf{E}[t|t-1] = \mathbf{E}[t-1|t-1] + \mathbf{Q}, \tag{5.43}$$

where $\mathbf{Q}$ is the process noise covariance matrix. In the correction step, the Kalman gain $\mathbf{K}[t]$ is computed as:

$$\mathbf{K}[t] = \mathbf{E}[t|t-1]\mathbf{F}^{\top}[t]\big(\mathbf{C}[t] + \mathbf{F}[t]\mathbf{E}[t|t-1]\mathbf{F}^{\top}[t]\big)^{-1}. \tag{5.44}$$

Finally, the updated state estimate is:

$$\hat{\mathbf{P}}[t|t] = \hat{\mathbf{P}}[t|t-1] + \mathbf{K}[t]\big(\hat{\mathbf{\Gamma}}[t] - f(\hat{\mathbf{P}}[t|t-1])\big), \tag{5.45}$$

and the error covariance is revised as:

$$\mathbf{E}[t|t] = (\mathbf{I} - \mathbf{K}[t]\mathbf{F}[t])\mathbf{E}[t|t-1]. \tag{5.46}$$

In this context, the tracking process begins by initializing Equations (5.42) and (5.43) with $\hat{\mathbf{P}}[-1|-1] = \mathbf{P}_0$ and $\mathbf{E}[-1|-1] = \mathbf{Q}_0$. Here, (5.42) corresponds to the prediction step, formulated based on the transition model given in (5.5), while (5.43) calculates the minimum prediction MSE matrix, $\mathbf{E} \in \mathbb{R}^{2\times 2}$. Additionally, equation (5.44) determines the Kalman gain matrix $\mathbf{K}[t] \in \mathbb{R}^{2\times M}$ based on the measurement error matrix $\mathbf{C}[t]$, which quantifies the uncertainties in the measurement process and is defined in (5.34). Subsequently, the correction step in (5.45) refines the prediction $\hat{\mathbf{P}}[t \mid t-1]$ from (5.42) by

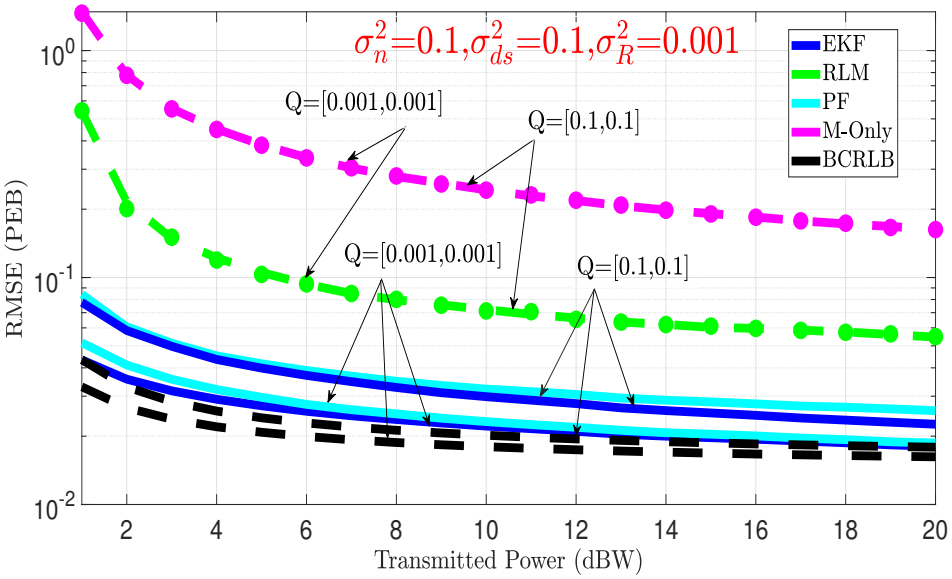

Figure 5.3: RMSE comparison for the EKF, M-Only, RLM, PF, and the PEB from BCRLB as in (5.27) under $\mathbf{Q} = [0.001, 0.001]$ and $\mathbf{Q} = [0.01, 0.01]$, with noise variances $\sigma_n^2 = 0.1$, $\sigma_{\text{ds}}^2 = 0.1$, and $\sigma_R^2 = 0.001$.

incorporating the current measurements, $\hat{\mathbf{\Gamma}}[t]$. This correction step aims to produce a more accurate estimate of the position vector, $\hat{\mathbf{P}}[t|t]$. The output, $\hat{\mathbf{P}}[t \mid t]$, represents the tracker's result for the t-th sample, which depends on all the information from the initial sample up to the t-th sample. The minimum MSE matrix for the updated state is given in (5.46). The updated $\hat{\mathbf{P}}[t|t]$ and $\mathbf{E}[t|t]$ are then re-fed as prior values for the next prediction step in (5.42),(5.43) [53], [69].

5.5 Simulation Results and Discussion

Simulations were conducted using MATLAB to evaluate the performance of the MISO-VLP system under the joint effects of SDSN and RIN. Approximately 10^6 Monte Carlo

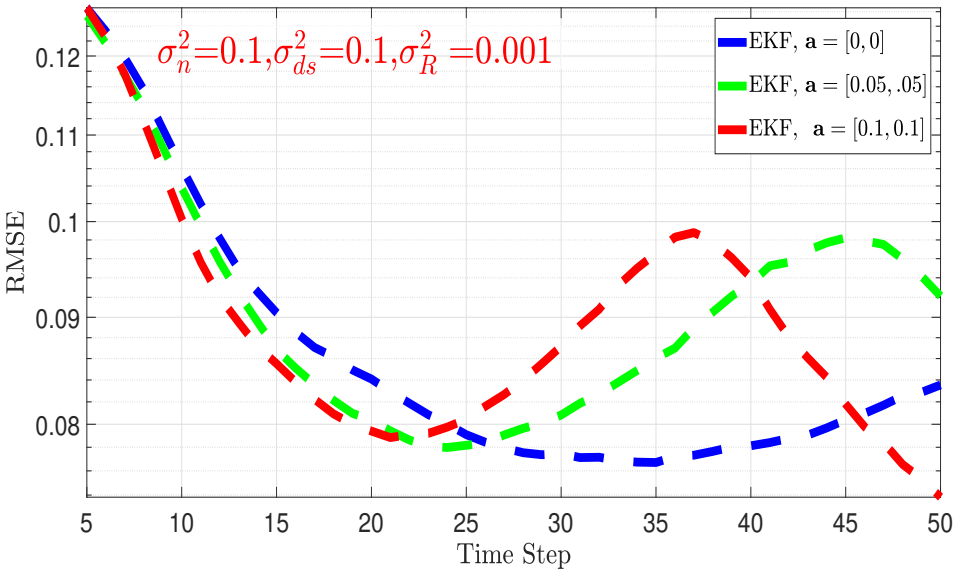

Figure 5.4: Compare RMSE over time for EKF at different values of acceleration under $\mathbf{Q} = [0.001, 0.001]$ and with noise variances $\sigma_n^2 = 0.1$, $\sigma_{\text{ds}}^2 = 0.1$, and $\sigma_R^2 = 0.001$.

iterations were performed to ensure statistical reliability. In each simulation run, six light sources were positioned within a $4\,\text{m} \times 4\,\text{m}$ room. The placement was constrained to guarantee that, at every time step, the receiver remained within the FoV of at least three light sources. This ensures robust signal reception and enables accurate trilateration.

All light sources were configured with identical physical and optical parameters, including a FoV angle of $\phi_{\text{FOV}} = 70°$, vertical separation $L = 3\,\text{m}$, active detection area $A_{\text{pd}} = 1\,\text{cm}^2$, and optical filter gain $T_s(\theta_{\text{rx}}) = 1$. The noise variances were defined as $\sigma_x^2 = 10^{-3}$, $\sigma_y^2 = 10^{-3}$, $\sigma_R^2 = 10^{-3}$, $\sigma_{\text{ds}}^2 = 10^{-1}$, and $\sigma_n^2 = 10^{-1}$.,Finally, without loosing the genrality, and to illustrate a representative scenario, six fixed light sources configuration was also analyzed with coordinates located at $[1, 1, 3]$, $[2, 1, 3]$, $[3, 1, 3]$, $[1, 3, 3]$, $[2, 3, 3]$, $[3, 3, 3]$. However, we would like to emphasize that our analysis is valid for any light source positions. The PD was initialized at $\mathbf{P}_0 = [2, 2, 0]$ meters in a two-dimensional plane and

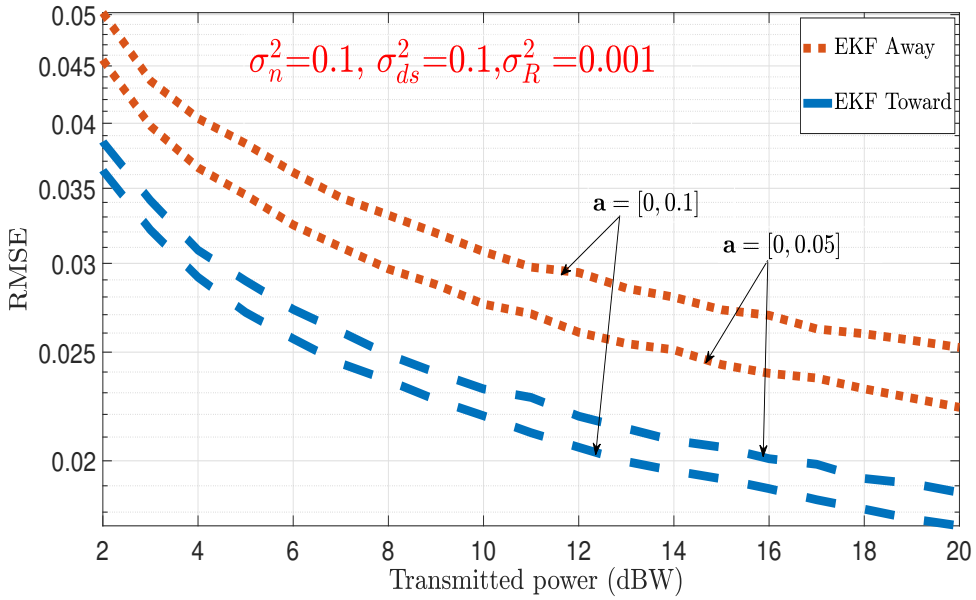

Figure 5.5: Compare RMSE of EKF and at different values of acceleration under $\mathbf{Q} = [0.001, 0.001]$ and with noise variances $\sigma_n^2 = 0.1$, $\sigma_{\text{ds}}^2 = 0.1$, and $\sigma_R^2 = 0.001$ in two cases toward light sources and away from them.

moved with a velocity limited to 1 m/s along both x-axis and y-axis. Pilot signals were transmitted at regular intervals of $\Delta = 0.01$ seconds and $\mathbf{a} = [0, 0]$. These are the default parameters unless stated otherwise.

In this work, we propose the use of the EKF for real-time tracking of a moving PD in VLP systems. The EKF integrates a dynamic motion model with nonlinear distance-based measurements to recursively estimate the PD's position in the presence of SDSN and RIN . In Fig. 5.3, we present a comparative RMSE analysis of four estimation techniques, including our proposed EKF-based localization method, to evaluate their performance in a VLP environment. The Measurement-Only (M-only) method estimates the PD position using geometric relationships derived from noisy distance measurements, typically solved through trilateration or numerical techniques, as described in detail in [4, 108] and the

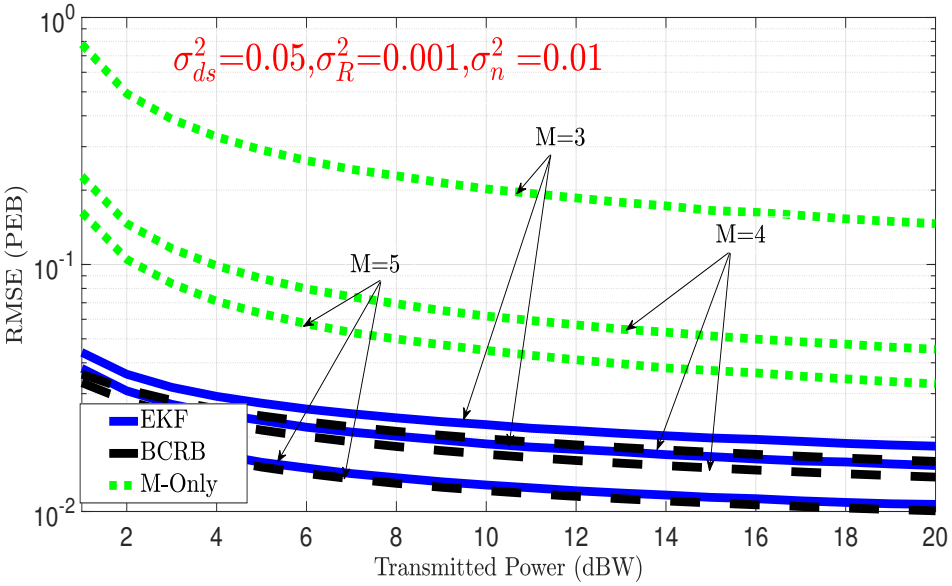

Figure 5.6: RMSE comparison for the EKF and the PEB from BCRLB as in (5.27) for varying numbers of light sources ($M = 3, 4, 5$), with noise variances $\sigma_n^2 = 0.01$, $\sigma_{\text{ds}}^2 = 0.05$, and $\sigma_R^2 = 0.001$.

references therein. The RLM algorithm applies a nonlinear least-squares optimization for real-time tracking, but lacks explicit modeling of system dynamics and process noise, limiting its robustness in dynamic scenarios and described in detail in [109–111] and the references therein. The PF uses a sampling-based Bayesian approach that is robust to nonlinearities and non-Gaussian noise but is computationally intensive, especially as the number of particles increases, and is described in detail in [101], [112], and the references therein. Our proposed EKF method combines both motion and measurement models in a recursive framework, offering a favorable balance between accuracy and computational complexity.

Moreover, the results in Fig. 5.3 show that the RMSE curves of the EKF and PF estimators (with the number of particles set to 100) are closely matched and consistently

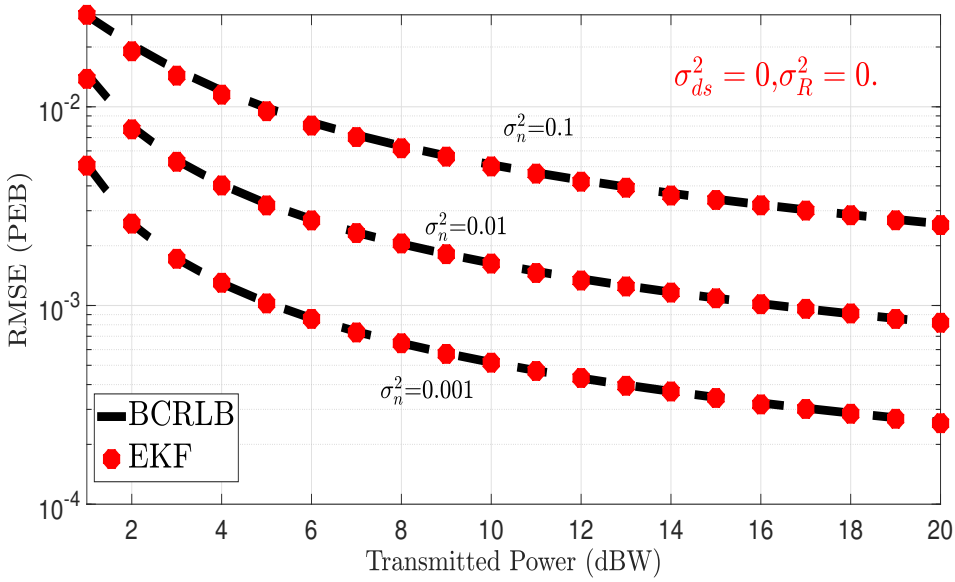

Figure 5.7: RMSE comparison for the EKF and the PEB from BCRLB as in (5.27) under varying thermal noise variances, with $\sigma_{\text{ds}}^2 = 0$ and $\sigma_R^2 = 0$.

outperform those of the RLM and M-only methods. Additionally, when varying the process noise covariance $\mathbf{Q}$, the RMSE of both M-only and RLM (with a damping factor set to 0.01) remains unchanged, as expected, since these methods do not model motion dynamics and are therefore insensitive to process noise. In this figure, the PD moves with linear velocity with the acceleration vector is defined as $\mathbf{a} = [0.1,\ 0.1]$ m/s^2.

In contrast, the RMSE for EKF and PF increases with larger $\mathbf{Q}$, along with a corresponding rise in the PEB calculated fromBCRLB. This behavior highlights their sensitivity to process uncertainty and reflects their reliance on accurate dynamic modeling. These findings align with the theoretical prediction in (5.24), where a higher process noise variance reduces the BFIM, resulting in an increased BCRLB and thereby validating the simulation results.

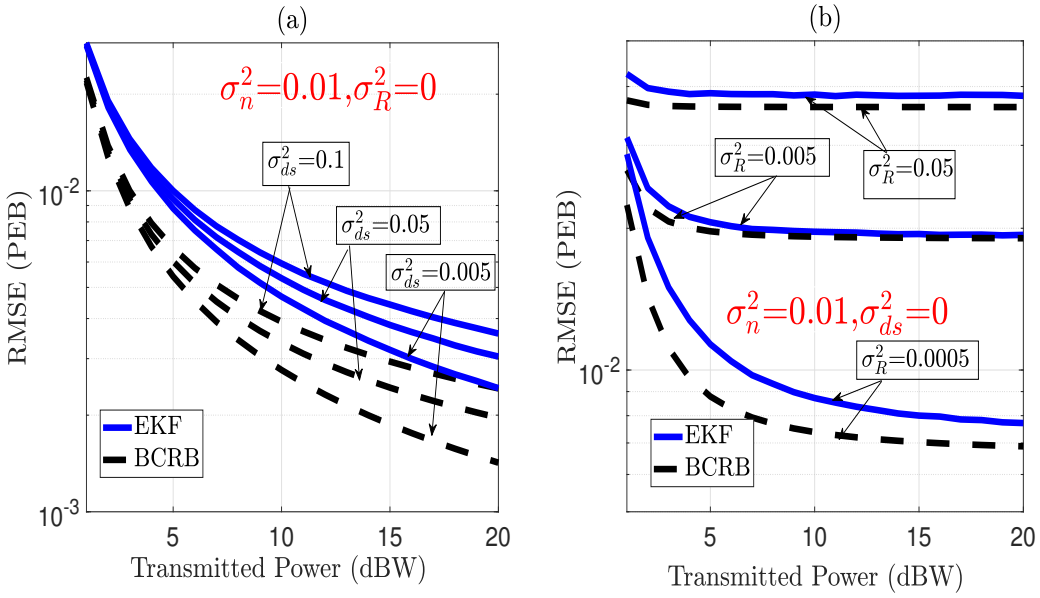

Figure 5.8: RMSE comparison for the EKF and the PEB from the BCRLB as in (5.27) under varying RIN and SDSN noise variances, with $\sigma_n^2 = 0.01$.

In Fig. 5.4, we assume that the PD moves with a velocity that changes linearly over time at accelaration, corresponding to different acceleration values, $\mathbf{a} = [0, 0]$, $\mathbf{a} = [0.05, 0.05]$ and $\mathbf{a} = [0.1, 0.1]$. The transmitted optical power is fixed at $p = 10$ Watts. As observed from the figure, the RMSE initially decreases for the EKF estimator across all acceleration levels. This trend suggests that the relative distance between the PD and the light sources decreases during the early stages of motion, indicating that the PD is generally moving toward the light source cluster. However, after a certain point, the RMSE begins to increase. This behavior occurs because, although the PD may be approaching some light sources, it is simultaneously moving farther away from others, thereby increasing the total relative distance from the entire set of light sources. In multi-source localization scenarios, proximity to a single light source does not necessarily guarantee improved accuracy, as estimation performance depends on the relative geometry and cumulative distances to all

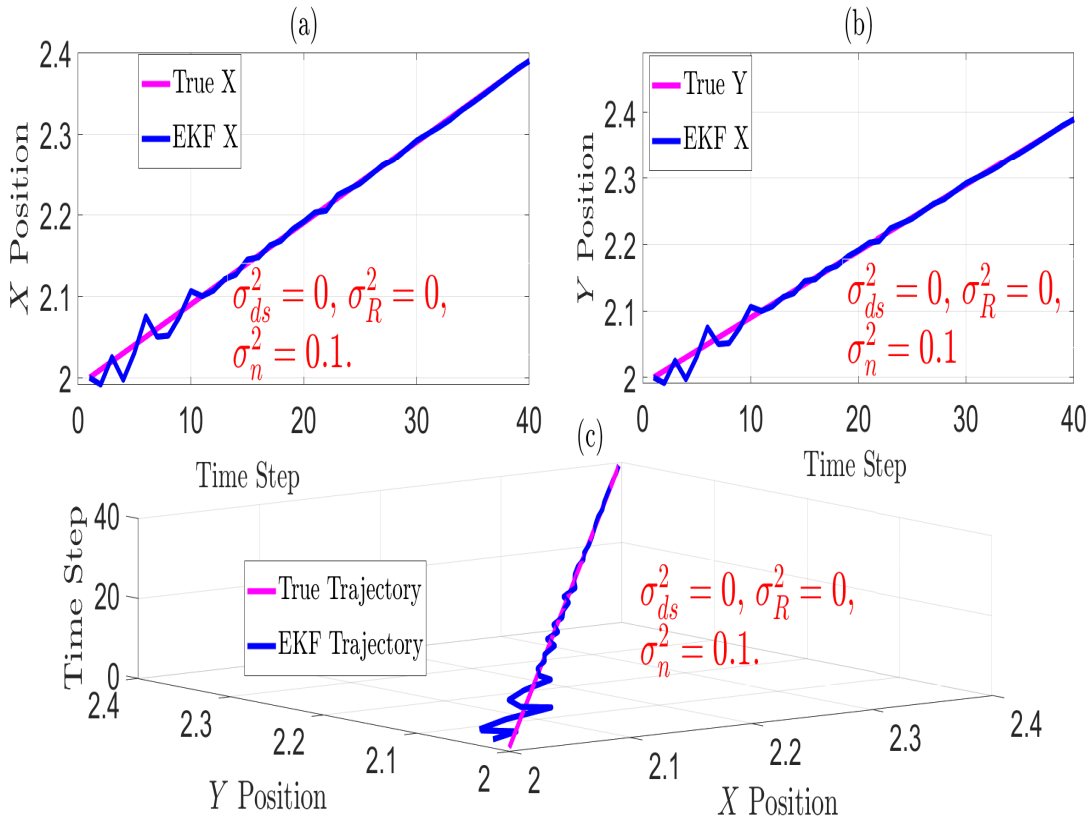

Figure 5.9: Position tracking comparison between the EKF trajectory and the true trajectory in the ideal case with $\sigma_R^2 = \sigma_{\text{ds}}^2 = 0$ and $\sigma_n^2 = 0.1$.

transmitters. Furthermore, the figure shows that higher acceleration leads to earlier shifts in the RMSE trend compared to lower acceleration. This observation highlights the role of acceleration in modulating the motion dynamics of the PD and its impact on localization performance.

Fig. 5.5 illustrates the RMSE performance of the EKF for a PD localizing under three light sources positioned at coordinates $[1, 1, 3], [2, 1, 3]$ and $[3, 1, 3]$. The PD is initialized at $[2, 2, 0]$ and moves linearly along the y-axis under two different acceleration magnitudes:

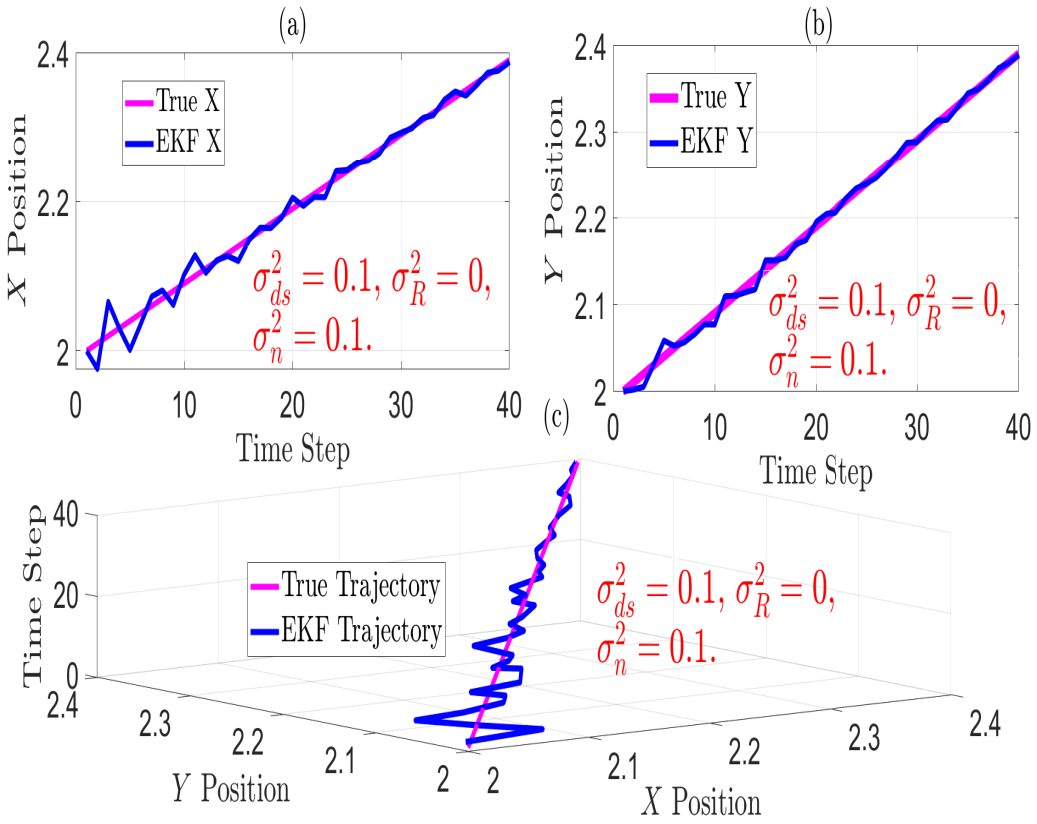

Figure 5.10: Position tracking comparison between the EKF trajectory and the true trajectory in the case of no RIN noise and the presence of SDSN noise with $\sigma_{\text{ds}}^2 = 0.1$ and $\sigma_n^2 = 0.1$.

$\mathbf{a} = [0, 0.05]\,\text{m/s}^2$ and $\mathbf{a} = [0, 0.1]\,\text{m/s}^2$. The motion is examined in two cases: the PD moving toward the light sources and moving away from them. In both cases, the RMSE behavior is strongly influenced by the distance between the PD and the light sources. When the PD moves toward the light sources, the RMSE is lower than when it moves away from them. This is due to the inverse dependence of signal strength on distance, which directly affects measurement quality and aligns with the (5.22) and Remark 1. Furthermore, the effect of acceleration magnitude is notable. In the scenario where the PD accelerates toward

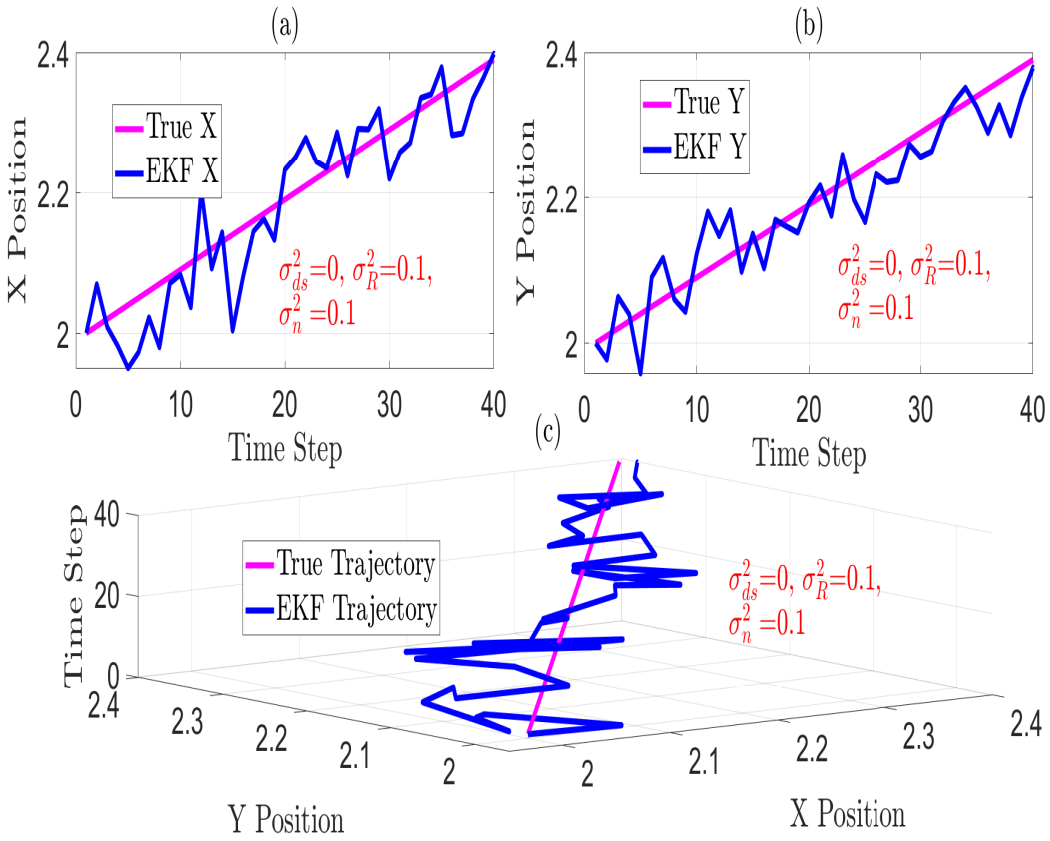

Figure 5.11: Position tracking comparison between the EKF trajectory and the true trajectory in the case of no SDSN noise and the presence of RIN noise with $\sigma_R^2 = 0.1$ and thermal noise with $\sigma_n^2 = 0.1$.

the light sources, the higher magnitude $\mathbf{a} = [0, 0.1], \mathrm{m/s}^2$ results in a faster reduction in RMSE. Conversely, when the PD accelerates away from the light sources, the same magnitude leads to a more rapid increase in RMSE compared to the lower acceleration $\mathbf{a} = [0, 0.05]\,\mathrm{m/s}^2$.

Fig. 5.6 illustrates the impact of the number of light sources on the RMSE of location estimation where $\sigma_n^2 = 0.01$, $\sigma_{ds}^2 = 0.05$ and $\sigma_R^2 = 0.001$ .The results demonstrate that increasing the number of light sources improves the accuracy of the location estimation,

reducing the RMSE in both the M-only approach and the EKF. Additionally, the EKF performance approaches the PEB that calculated from the BCRLB as the number of light sources increases. This improvement is consistent with the theoretical relationship described in (5.22), which highlights the dependency of the PFIM on the number of light sources, M. As M increases, the value of the PFIM, $\mathbf{J}_{\mathbf{P}}^{(\mathrm{O})}[t]$, increases, leading to a reduction in the BCRLB. This result confirms that incorporating more light sources enhances the precision of position estimation by providing greater spatial diversity and improving system observability.

Fig. 5.7 illustrates the performance of the EKF in location estimation under the scenario where σ_n^2 is non-zero, $\sigma_{ds}^2 = 0$, $\sigma_R^2 = 0$, and $\mathbf{v}(\mathbf{t}) = [0, 0]$. In this case, the only source of error from measurements is thermal noise with variance σ_n^2. The results demonstrate that, in the absence of SDSN and RIN, the EKF acts as the optimal estimator, with its RMSE of EKF closely aligning with the PEB derived for the BCRLB. Furthermore, the figure highlights that as the value of σ_n^2 increases, the RMSE also rises, which is consistent with the theoretical results presented in (5.17) and Remark 2. This confirms the expected dependency of estimation accuracy on noise levels. The performance comparison of the EKF and the BCRLB is presented in Fig. 5.8. In Fig.5.8 (a), we consider the case where $\sigma_R^2 = 0$, $\sigma_n^2 = 0.01$, and σ_{ds}^2 varies. It can be observed that the presence of SDSN prevents the EKF and the PEB from the BCRLB from becoming identical, unlike the results shown in Fig. 5.7. As the value of σ_{ds}^2 increases, both the RMSE and the PEB of the BCRLB increase, leading to a degradation in estimation performance.

In Fig. 5.8 (b), the scenario is reversed: $\sigma_{ds}^2 = 0$, while σ_R^2 varies, with σ_n^2 set to 0.01, similar to Fig 5.8 (a). The RMSE is larger when σ_R^2 is present compared to when σ_{ds}^2 is the dominating noise. Additionally, the RMSE and PEB from the BCRLB saturate at specific values, which does not occur in the case of SDSN, as shown in Fig. 5.8 (a). This

behavior is consistent with the theoretical results derived in (5.17) and Remark 6. As show in (5.17), σ_s^2 includes σ_R^2 multiplied by p^2 and σ_{ds}^2 multiplied by p. Consequently, increasing the RIN worsens the estimation accuracy more significantly than SDSN. This is further demonstrated in Fig. 5.8, where even though the values of σ_{ds}^2 are larger than σ_R^2, the RMSE does not reach saturation in the case of SDSN.

Fig. 5.9 shows the trajectory of the PD target location along the x- and y-axes in (a) and (b) sub-figures in sequence and in the 2D plane in the (c) sub-figure for $\sigma_{ds}^2 = 0$, $\sigma_n^2 = 0.1$, and $\sigma_R^2 = 0$. As observed with $\sigma_R^2 = 0$ and $\sigma_{ds}^2 = 0$, the EKF accurately tracks the moving target. However, in the presence of thermal noise ($\sigma_n^2 > 0$), the EKF learns to compensate for the thermal noise effect over time, as it is independent of the transmitted power. This aligns with the findings in Fig. 5.7.

In Fig. 5.10, we analyze the scenario where $\sigma_{ds}^2 = 0.1$, $\sigma_n^2 = 0.1$, and $\sigma_R^2 = 0$. The results indicate that the presence of SDSN noise significantly degrades the tracking accuracy of the EKF, and we can see that in x-y axes tracking in subfigures (a), (b), and 2D Plane in subfigure (c). This degradation stems from imperfections in the transmitter and receiver materials, which introduce signal-dependent noise that adversely affects the efficiency of the tracking process. As described in (5.41), the measurement noise variance is directly influenced by the variance of SDSN, leading to reduced estimation performance.

In Fig. 5.11, we analyze the impact of RIN noise on tracking accuracy. The results demonstrate that RIN noise significantly degrades the precision of target tracking. As explained in (5.41), the variance of RIN noise increases with the quadratic transmitted power, severely impairing the EKF's ability to track the target's position accurately. This emphasizes the EKF's sensitivity to power-dependent noise sources such as RIN and SDSN, further highlighting the challenges these noise types pose in maintaining tracking efficiency. We can see the RIN effect in the $x-$axis in Fig. 5.11 (a), in the $y-$axis in Fig. 5.11 (b),

and in the $x - y$ plane in Fig. 5.11 (c).

5.6 Conclusion

In this chapter, we investigated position estimation and tracking in indoor VLC systems using a MISO-VLC setup with multiple light sources as transmitters. An EKF was applied for real-time position tracking, and its performance was compared against several alternative techniques. These included a measurement-only approach based on solving geometric equations from noisy distances, the RLM method, and a PF. The results demonstrated that the EKF achieves significantly lower RMSE in estimated positions. While PF offers similar accuracy, it incurs higher computational complexity, and RLM and mesumenrt only show less robustness due to its sensitivity to nonlinearity and lack of state propagation.

Additionally, we evaluated the impact of increasing the number of light sources on localization accuracy. Our findings indicate that as the number of light sources increases and the target remains within their effective coverage, the spatial diversity improves, leading to enhanced estimation precision. We further investigated the effects of signal-dependent noise sources, specifically RIN and SDSN. The results showed that higher levels of RIN degrade both tracking and estimation performance more severely than SDSN. To establish a theoretical performance benchmark, we derived a closed-form BCRLB. The analysis revealed that the BCRLB is influenced by SDSN, RIN, and process noise, validating the EKF's effectiveness against this theoretical bound and confirming its suitability for dynamic VLC-based localization systems. It is worth noting that the current work assumes LoS propagation. In practice, NLoS components may arise, e.g., due to reflections, potentially impacting the estimator's accuracy. Therefore, extending the proposed VLP and tracking framework to account for NLoS conditions in conjunction with signal-dependent

noise represents an important direction for future research.

5.7 Publications Resulted from This Chapter

Sara ElFar, Maysa Yaseen and Salama Ikki, "Tracking and Positioning Dynamic Targets in VLC: Signal Dependent Noises and Bayesian Bound Analysis," *IEEE Transactions on Communications* , Accepted, 2025.

Chapter 6

Conclusions and Future Work

This thesis has presented a comprehensive study of channel estimation, range estimation, localization, and tracking in visible light systems under the influence of signal-dependent noise sources. A set of novel estimation approaches and recursive techniques was introduced, supported by closed-form theoretical analyses and benchmark evaluations such as the closed-form expressions of the MSE and the BCRLB. The findings demonstrate that the proposed frameworks are well-suited for scenarios dominated by signal-dependent noise. The contributions of this thesis can be summarized by chapter as follows:

Chapter 3 : Channel Estimation

We proposed a novel channel estimation framework that integrates the conventional LS estimator with a NN. This hybrid LS–NN estimator was designed to mitigate the degradation of LS in the presence of SDSN. A closed-form MSE expression for the integrated estimator was derived using theoretical analysis and validated through simulations. Results showed strong alignment between analysis and simulations, confirming that once the NN weights

and biases are determined, the MSE_{NN} rule can be applied directly. This contribution provides the first step toward combining traditional estimation with machine learning for robust channel estimation in VLC systems.

In this chapter, we further study the case of employing a MLP as the neural network structure. By varying the number of hidden layers, we investigate how the network complexity influences estimation accuracy. From the semi-analytical mathematical analysis, we gain insights into the role of neural network weights and biases in correcting the errors introduced by the LS estimator. To evaluate the performance of the proposed framework, we also integrate the MLE with the NN, thereby enhancing estimation robustness under different noise conditions. Various training techniques are applied to demonstrate the efficiency of the proposed algorithm and to highlight the improvement achieved by the hybrid estimation scheme compared to conventional approaches.

Chapter 4: Range Estimation

We investigated range estimation in a SISO VLC system under the influence of SDSN. To address this problem, both non-recursive and recursive estimation methods were applied. For the non-recursive case, we considered MLE and NLS, where a closed-form expression for the MSE of NLS was derived using parameter transformation. In parallel, we examined a recursive estimation method based on the EKF, which served as a dynamic benchmark against the non-recursive approaches.

Simulation results demonstrated that estimation errors increase as the severity of SDSN grows, yet the EKF consistently provided superior accuracy and robustness compared to its non-recursive counterparts. We further analyzed the impact of receiver plane tilting and confirmed the high sensitivity of estimation accuracy to receiver orientation. Finally,

we derived BCRLB, which established a theoretical benchmark and was found to closely align with the observed simulation results, reinforcing the validity of the proposed analysis.

Chapter 5 : Localization and Tracking

We extended the analysis to position estimation and tracking in MISO VLC systems. An EKF was applied for dynamic tracking and evaluated against several alternative techniques. Measurement-only localization was performed using noisy geometric equations, while recursive approaches such as the RLM algorithm and PF were also investigated. Among these methods, the EKF achieved the best balance between accuracy and computational complexity. Although PF offered comparable accuracy, it required considerably higher computational cost. In contrast, the RLM and measurement-only techniques were found to be less robust, mainly due to their sensitivity to nonlinearities and lack of state propagation.

We further examined the impact of increasing the number of light sources, which revealed that a higher source density improves spatial diversity and enhances localization precision. Importantly, this thesis is the first to systematically analyze the combined effects SDSN and glsrin on localization performance. The results demonstrated that RIN causes more severe degradation than SDSN. To provide a theoretical benchmark, we derived a closed-form BCRLB that incorporates both SDSN and RIN, and showed that the EKF closely approaches this bound in dynamic tracking scenarios.

6.1 Limitations and Future Research Directions

This thesis has provided new insights into channel estimation, range estimation, localization, and tracking in visible light systems under signal-dependent noise. While several important challenges have been addressed, some aspects were beyond the scope of this study and naturally point to future research opportunities.

One such aspect is the restriction to LoS scenarios and relatively static channel models. In practice, NLoS conditions, time-varying channels, and user mobility play a significant role. Extending the analysis to incorporate these effects, possibly through advanced time-series methods such as recurrent neural networks (RNN) and Autoregressive neural networks (ARNNs), will yield more realistic system models.

Another promising direction lies in expanding the role of machine learning. This work focused primarily on integrating neural networks with classical estimators, but further advances can be achieved through meta-learning and federated learning. These approaches would enable estimators to quickly adapt to new environments and allow distributed devices to collaborate without central data collection, aligning well with the vision of edge intelligence in future wireless systems.

Future research can also extend beyond the indoor scenarios studied here. Outdoor VLC, vehicular communication, and underwater VLC are emerging fields where the techniques developed in this thesis could be adapted to address new propagation challenges such as scattering, Doppler shifts, and weather-induced fading.

Hybridization with other technologies offers another rich area for exploration. Cooperative localization frameworks that fuse VLC with RF-based systems (e.g., Wi-Fi, mmWave, or 5G/6G) can improve coverage and reliability. Similarly, moving from 2D to 3D localization will be essential for deployment in complex real-world environments such as airports,

hospitals, and shopping malls.

Finally, while this thesis has primarily analyzed SDSN and RIN, practical deployments must also contend with other impairments such as ambient light interference, LED flicker, and cross-channel disruptions. Incorporating these effects into estimation and tracking frameworks represents an important step toward fully practical systems.

In summary, the contributions of this thesis lay the foundation for robust estimation under signal-dependent noise. Future research that expands the scope to dynamic environments, advanced learning paradigms, hybrid system designs, and broader application scenarios will further advance VLC-based localization and tracking toward real-world adoption.

Appendix: Derivation of the Prior Information FIM

This appendix provides the detailed derivation of the prior information FIM, denoted as $\mathbf{J_P}^{(I)}$ The prior information about the PD transition is modeled statistically as Gaussian in (5.5). The log function of the Gaussian PDF can be expressed as:

$$\log p(\mathbf{P}[t] \mid \mathbf{P}[t-1]) = A - \frac{1}{2}\log|\mathbf{Q}| - \frac{1}{2}\left(\mathbf{P}[t] - (\mathbf{P}[t-1] + \mathbf{q}[t])\right)^T \mathbf{Q}^{-1}\left(\mathbf{P}[t] - (\mathbf{P}[t-1] + \mathbf{q}[t])\right), \tag{1}$$

where A is a constant, and $\mathbf{Q}$ is a matrix representing process noise. The first derivatives of the log-likelihood with respect to $\mathbf{P}[t]$ and $\mathbf{P}[t-1]$ are:

$$\frac{\partial \log p(\mathbf{P}[t]|\mathbf{P}[t-1])}{\partial \mathbf{P}[t]} = -(\mathbf{Q})^{-1}\left(\mathbf{P}[t] - (\mathbf{P}[t-1] + \mathbf{q}[t])\right), \tag{2}$$

and

$$\frac{\partial \log p(\mathbf{P}[t] \mid \mathbf{P}[t-1])}{\partial \mathbf{P}[t-1]} = (\mathbf{Q})^{-1}\left(\mathbf{P}[t] - (\mathbf{P}[t-1] + \mathbf{q}[t])\right). \tag{3}$$

The second derivatives of the log-likelihood are:

$$\frac{\partial^2 \log p(\mathbf{P}[t] \mid \mathbf{P}[t-1])}{\partial \mathbf{P}[t] \partial \mathbf{P}[t]^T} = -(\mathbf{Q})^{-1}, \tag{4}$$

$$\frac{\partial^2 \log p(\mathbf{P}[t] \mid \mathbf{P}[t-1])}{\partial \mathbf{P}[t-1] \partial \mathbf{P}[t-1]^T} = -(\mathbf{Q})^{-1}, \tag{5}$$

$$\frac{\partial^2 \log p(\mathbf{P}[t] \mid \mathbf{P}[t-1])}{\partial \mathbf{P}[t] \partial \mathbf{P}[t-1]^T} = (\mathbf{Q})^{-1}, \tag{6}$$

$$\frac{\partial^2 \log p(\mathbf{P}[t] \mid \mathbf{P}[t-1])}{\partial \mathbf{P}[t-1] \partial \mathbf{P}[t]^T} = (\mathbf{Q})^{-1}. \tag{7}$$

Using these derivatives, the components of the Fisher information matrix ($\boldsymbol{G}[t]$) are defined as follows:

$$\boldsymbol{G}_{11}[t] = \mathbb{E}\left(-\frac{\partial^2 \log p(\mathbf{P}[t] \mid \mathbf{P}[t-1])}{\partial \mathbf{P}[t-1] \partial \mathbf{P}[t-1]^T}\right) = (\mathbf{Q})^{-1}, \tag{8a}$$

$$\boldsymbol{G}_{12}[t] = \mathbb{E}\left(-\frac{\partial^2 \log p(\mathbf{P}[t] \mid \mathbf{P}[t-1])}{\partial \mathbf{P}[t-1] \partial \mathbf{P}[t]^T}\right) = -(\mathbf{Q})^{-1}, \tag{8b}$$

$$\mathbf{G}_{21}[t] = \mathbb{E}\left(-\frac{\partial^2 \log p(\mathbf{P}[t] \mid \mathbf{P}[t-1])}{\partial \mathbf{P}[t] \partial \mathbf{P}[t-1]^T}\right) = -(\mathbf{Q})^{-1}, \tag{8c}$$

$$\boldsymbol{G}_{22}[t] = \mathbb{E}\left(-\frac{\partial^2 \log p(\mathbf{P}[t] \mid \mathbf{P}[t-1])}{\partial \mathbf{P}[t] \partial \mathbf{P}[t]^T}\right) = (\mathbf{Q})^{-1}. \tag{8d}$$

which concludes the proof.

References

[1] (2021, Sep.) Introduction to infrared reflectography. [Online]. Available: https://www.opusinstruments.com/infrared-reflectography/

[2] J. Chen, T. Liu, and T. Shu, "A survey on visible light communication standards," *GetMobile: Mobile Computing and Communications*, vol. 25, no. 1, pp. 9–15, 2021.

[3] R. Hui and M. O'Sullivan, *Fiber-Optic Measurement Techniques*. Academic Press, 2022.

[4] H. M. Le, J.-P. Rossi, and D. Slock, "A geometric interpretation of trilateration for rss-based localization," in *2020 28th European Signal Processing Conference (EUSIPCO)*. IEEE, 2021, pp. 1797–1801.

[5] S. Y. Khamaiseh, D. Bagagem, A. Al-Alaj, M. Mancino, and H. W. Alomari, "Adversarial deep learning: A survey on adversarial attacks and defense mechanisms on image classification," *IEEE Access*, vol. 10, pp. 102 266–102 291, 2022.

[6] Z. Ghassemlooy, W. Popoola, and S. Rajbhandari, *Optical wireless communications: system and channel modelling with Matlab®*. CRC press, 2019.

[7] A. Singla, D. Sharma, and S. Vashisth, "Data connectivity in flights using visible light communication," in *2017 International Conference on Computing and Communication Technologies for Smart Nation (IC3TSN)*. IEEE, 2017, pp. 71–74.

[8] S. Rajagopal, R. D. Roberts, and S.-K. Lim, "Ieee 802.15. 7 visible light communication: modulation schemes and dimming support," *IEEE Communications Magazine*, vol. 50, no. 3, pp. 72–82, 2012.

[9] H.-S. Kim, D.-R. Kim, S.-H. Yang, Y.-H. Son, and S.-K. Han, "An indoor visible light communication positioning system using a rf carrier allocation technique," *Journal of lightwave technology*, vol. 31, no. 1, pp. 134–144, 2012.

[10] Z. Zhu, Y. Yang, M. Chen, C. Guo, J. Cheng, and S. Cui, "A survey on indoor visible light positioning systems: Fundamentals, applications, and challenges," *arXiv preprint arXiv:2401.13893*, 2024.

[11] H. Liu, H. Darabi, P. Banerjee, and J. Liu, "Survey of wireless indoor positioning techniques and systems," *IEEE Transactions on Systems, Man, and Cybernetics, Part C (Applications and Reviews)*, vol. 37, no. 6, pp. 1067–1080, 2007.

[12] P. Müller, H. Wymeersch, and R. Piché, "Uwb positioning with generalized gaussian mixture filters," *IEEE Transactions on Mobile Computing*, vol. 13, no. 10, pp. 2406–2414, 2014.

[13] P. Davidson and R. Piché, "A survey of selected indoor positioning methods for smartphones," *IEEE Communications surveys & tutorials*, vol. 19, no. 2, pp. 1347–1370, 2016.

[14] Z. Song, G. Jiang, and C. Huang, "A survey on indoor positioning technologies," in *Theoretical and Mathematical Foundations of Computer Science: Second International Conference, ICTMF 2011, Singapore, May 5-6, 2011. Selected Papers*. Springer, 2011, pp. 198–206.

[15] T. Komine and M. Nakagawa, "Fundamental analysis for visible-light communication system using led lights," *IEEE transactions on Consumer Electronics*, vol. 50, no. 1, pp. 100–107, 2004.

[16] S. Mohapatra, G. Satapathy, S. P. Dash, and P. R. Sahu, "Performance analysis of visible light communication system with imperfect csi," *IEEE Communications Letters*, vol. 24, no. 12, pp. 2844–2848, 2020.

[17] M. Safari, "Efficient optical wireless communication in the presence of signal-dependent noise," in *2015 IEEE International Conference on Communication Workshop (ICCW)*. IEEE, 2015, pp. 1387–1391.

[18] M. Yaseen, M. Elamassie, S. Ikki, and M. Uysal, "Signal-dependent shot and relative intensity noise in channel estimation of laser diode-based indoor vlc systems," *IEEE Transactions on Communications*, 2024.

[19] K. Lau and A. Yariv, "Ultra-high speed semiconductor lasers," *IEEE Journal of Quantum Electronics*, vol. 21, no. 2, pp. 121–138, 1985.

[20] M. Yaseen, A. E. Canbilen, and S. Ikki, "Channel estimation in visible light communication systems: The effect of input signal-dependent noise," *IEEE Transactions on Vehicular Technology*, vol. 72, no. 11, pp. 14 330–14 340, 2023.

[21] Q. Gao, S. Hu, C. Gong, and Z. Xu, "Modulation designs for visible light communications with signal-dependent noise," *Journal of Lightwave Technology*, vol. 34, no. 23, pp. 5516–5525, 2016.

[22] H. Haas, J. Elmirghani, and I. White, "Optical wireless communication," p. 20200051, 2020.

[23] S. Arai, M. Kinoshita, and T. Yamazato, "Optical wireless communication: A candidate 6g technology?" *IEICE Transactions on Fundamentals of Electronics, Communications and Computer Sciences*, vol. 104, no. 1, pp. 227–234, 2021.

[24] M. Z. Chowdhury, M. T. Hossan, A. Islam, and Y. M. Jang, "A comparative survey of optical wireless technologies: Architectures and applications," *ieee Access*, vol. 6, pp. 9819–9840, 2018.

[25] G. Pang, K.-L. Ho, T. Kwan, and E. Yang, "Visible light communication for audio systems," *IEEE Transactions on Consumer Electronics*, vol. 45, no. 4, pp. 1112–1118, 1999.

[26] L. U. Khan, "Visible light communication: Applications, architecture, standardization and research challenges," *Digital Communications and Networks*, vol. 3, no. 2, pp. 78–88, 2017.

[27] E. Gerhátné Udvary, "Visible light communication survey," *Infocommunications journal*, vol. 11, no. 2, pp. 22–31, 2019.

[28] P. S. Farahsari, A. Farahzadi, J. Rezazadeh, and A. Bagheri, "A survey on indoor positioning systems for iot-based applications," *IEEE Internet of Things Journal*, vol. 9, no. 10, pp. 7680–7699, 2022.

[29] M. A. Arfaoui, M. D. Soltani, I. Tavakkolnia, A. Ghrayeb, M. Safari, C. M. Assi, and H. Haas, "Physical layer security for visible light communication systems: A survey," *IEEE Communications Surveys & Tutorials*, vol. 22, no. 3, pp. 1887–1908, 2020.

[30] A. N. Barreto, B. Faria, E. Almeida, I. Rodriguez, M. Lauridsen, R. Amorim, and R. Vieira, "5g–wireless communications for 2020," *Journal of Communication and Information Systems*, vol. 31, no. 1, 2016.

[31] P. H. Pathak, X. Feng, P. Hu, and P. Mohapatra, "Visible light communication, networking, and sensing: A survey, potential and challenges," *IEEE Commun. Surveys Tuts.*, vol. 17, no. 4, pp. 2047–2077, 2015.

[32] S. W. Hasinoff, "Photon, poisson noise," in *Computer vision: a reference guide*. Springer, 2021, pp. 980–982.

[33] J. Wei, Y. Wang, C. Gong, and N. Huang, "Noise analysis and modulation optimization for nonlinear visible light communication system with signal-dependent noise," *IEEE Photonics Journal*, vol. 15, no. 6, pp. 1–11, 2023.

[34] C. Beenakker and C. Schönenberger, "Quantum shot noise," *Physics Today*, vol. 56, no. 5, pp. 37–42, 2003.

[35] M. Yaseen, M. Alsmadi, A. E. Canbilen, and S. S. Ikki, "Visible light communication with input-dependent noise: Channel estimation, optimal receiver design and performance analysis," *Journal of Lightwave Technology*, vol. 39, no. 23, pp. 7406–7416, 2021.

[36] M. F. Keskin, A. D. Sezer, and S. Gezici, "Localization via visible light systems," *Proceedings of the IEEE*, vol. 106, no. 6, pp. 1063–1088, 2018.

[37] S. M. Kay, *Fundamentals of statistical signal processing: estimation theory*. Prentice-Hall, Inc., 1993.

[38] P. Tichavsky, C. H. Muravchik, and A. Nehorai, "Posterior cramér-rao bounds for discrete-time nonlinear filtering," *IEEE Transactions on signal processing*, vol. 46, no. 5, pp. 1386–1396, 1998.

[39] D. A. Tubail, M. El-Absi, S. Ikki, and T. Kaiser, "Hardware-aware joint localization-synchronization and tracking using reconfigurable intelligent surfaces in 5g and beyond," *IEEE Open Journal of the Communications Society*, 2024.

[40] D. A. Tubail and S. S. Ikki, "Bayesian cramer-rao bound, extended and unscented kalman filters based tracking through non-ideal transceivers in 5g and beyond," *IEEE Transactions on Vehicular Technology*, 2024.

[41] D. A. Tubail and S. Ikki, "Range-direction tracking and bayesian cramer-rao bound analysis in mmwave systems equipped with imperfect transceivers," *IEEE Wireless Communications Letters*, 2023.

[42] Machine Learning for Science Team. (2020) Supervised learning with neural networks. Accessed: 2025-08-21. [Online]. Available: https://ml-lectures.org/docs/supervised_learning_w_NNs/ml_supervised_w_NNs.html

[43] I. Goodfellow, "Deep learning-ian goodfellow, yoshua bengio, aaron courville-google books," 2016.

[44] X. Liu, D. Zou, N. Huang, and S. Zhang, "A comprehensive accuracy analysis of visible light positioning under shot noise," in *2020 IEEE/CIC International Conference on Communications in China (ICCC Workshops)*. IEEE, 2020, pp. 167–172.

[45] C. Amini, P. Azmi, and S. S. Kashef, "An accurate ranging algorithm based on received signal strength in visible light communication," *Journal of Lightwave Technology*, vol. 39, no. 14, pp. 4654–4660, 2021.

[46] A. Cheema, M. Alsmadi, and S. Ikki, "Distance estimation error performance of visible light communication under the effect of signal-dependent noise," in *2021 IEEE 32nd Annual International Symposium on Personal, Indoor and Mobile Radio Communications (PIMRC)*. IEEE, 2021, pp. 771–776.

[47] S. K. G. S. Bose and A. Kumar, "Dnn based channel estimation for indoor mimo multipath visible light communication system," in *2023 14th International Conference on Computing Communication and Networking Technologies (ICCCNT)*, 2023, pp. 1–7.

[48] Z. Gao, Y. Wang, X. Liu, F. Zhou, and K.-K. Wong, "Ffdnet-based channel estimation for massive mimo visible light communication systems," *IEEE Wireless Communications Letters*, vol. 9, no. 3, pp. 340–343, 2020.

[49] S. Bose, S. K. Ghorai, and A. Kumar, "Dnn based channel estimation for indoor mimo multipath visible light communication system," in *2023 14th International Conference on Computing Communication and Networking Technologies (ICCCNT)*. IEEE, 2023, pp. 1–7.

[50] B. Turan and S. Coleri, "Machine learning based channel modeling for vehicular visible light communication," *IEEE Transactions on Vehicular Technology*, vol. 70, no. 10, pp. 9659–9672, 2021.

[51] M. H. Rahman, M. Z. Chowdhury, I. B. K. Y. Utama, and Y. M. Jang, "Channel estimation for indoor massive mimo visible light communication with deep residual

convolutional blind denoising network," *IEEE Transactions on Cognitive Communications and Networking*, vol. 9, no. 3, pp. 683–694, 2023.

[52] J. C. Estrada-Jiménez, B. G. Guzmán, M. J. F.-G. García, and V. P. G. Jiménez, "Superimposed training-based channel estimation for miso optical-ofdm vlc," *IEEE Transactions on Vehicular Technology*, vol. 68, no. 6, pp. 6161–6166, 2019.

[53] S. H. ElFar, M. Yaseen, and S. Ikki, "Insights into visible light positioning: Range tracking and bayesian cramér-rao lower bound analysis," *IEEE Communications Letters*, 2024.

[54] J. Pradhan, V. K. Kappala, and S. K. Das, "Performance of channel estimation for multiuser vlc system using dco-ofdm and aco-ofdm," in *TENCON 2023-2023 IEEE Region 10 Conference (TENCON)*. IEEE, 2023, pp. 1064–1069.

[55] Q. Gao, C. Gong, and Z. Xu, "Joint transceiver and offset design for visible light communications with input-dependent shot noise," *IEEE Transactions on Wireless Communications*, vol. 16, no. 5, pp. 2736–2747, 2017.

[56] H. Chen and Z. Xu, "A two-dimensional constellation design method for visible light communications with signal-dependent shot noise," *IEEE Commun. Lett.*, vol. 22, no. 9, pp. 1786–1789, Sept. 2018.

[57] S. M. Moser, "Capacity results of an optical intensity channel with input-dependent gaussian noise," *IEEE Trans Inf. Theory*, vol. 58, no. 1, pp. 207–223, Jan 2012.

[58] L. Yin, W. O. Popoola, X. Wu, and H. Haas, "Performance evaluation of non-orthogonal multiple access in visible light communication," *IEEE Transactions on Communications*, vol. 64, no. 12, pp. 5162–5175, 2016.

[59] Z. Ghassemlooy, W. Popoola, and S. Rajbhandari, *Optical wireless communications: system and channel modeling with MATLAB*, 1st ed. CRC Press, May 2017.

[60] L. Wu, J. Cheng, Z. Zhang, J. Dang, and H. Liu, "Channel estimation for optical-ofdm-based multiuser miso visible light communication," *IEEE Photonics Technology Letters*, vol. 29, no. 20, pp. 1727–1730, 2017.

[61] X. Shi, S.-H. Leung, and J. Min, "Adaptive least squares channel estimation for visible light communications based on tap detection," *Optics Communications*, vol. 467, p. 125712, 2020.

[62] M. Yaseen, M. Alsmadi, A. E. Canbilen, and S. Ikki, "Visible light communication with input-dependent noise: Channel estimation, optimal receiver design and performance analysis," *Journal of Lightwave Technology*, vol. 39, no. 23, pp. 7406–7416, Dec. 2021.

[63] P. Morala, J. A. Cifuentes, R. E. Lillo, and I. Ucar, "Towards a mathematical framework to inform neural network modelling via polynomial regression," *Neural Networks*, vol. 142, pp. 57–72, 2021.

[64] ——, "Nn2poly: A polynomial representation for deep feed-forward artificial neural networks," *IEEE Transactions on Neural Networks and Learning Systems*, 2023.

[65] A. Winkelbauer, "Moments and absolute moments of the normal distribution," *arXiv preprint arXiv:1209.4340*, 2012.

[66] E. Gonendik and S. Gezici, "Fundamental limits on rss based range estimation in visible light positioning systems," *IEEE Communications Letters*, vol. 19, no. 12, pp. 2138–2141, 2015.

[67] B. Chen, L. Dang, N. Zheng, and J. C. P. , *Kalman Filtering Under Information Theoretic Criteria*, 1st ed. Switzerland: Spring Nature, Aug. 2023.

[68] B. Masri, *Recursive Cramer-Rao Lower Bound for Random Parameters*. University of California, Riverside, 2016.

[69] Y. Wang, H. Jie, and L. Cheng, "A fusion localization method based on a robust extended kalman filter and track-quality for wireless sensor networks," *Sensors*, vol. 19, no. 17, p. 3638, 2019.

[70] M. A. Arfaoui, M. D. Soltani, I. Tavakkolnia, A. Ghrayeb, M. Safari, C. M. Assi, and H. Haas, "Physical layer security for visible light communication systems: A survey," *IEEE Commun. Surveys Tuts.*, vol. 22, no. 3, pp. 1887–1908, 2020.

[71] M. G. Ulkar, T. Baykas, and A. E. Pusane, "Vlcnet: Deep learning based end-to-end visible light communication system," *Journal of Lightwave Technology*, vol. 38, no. 21, pp. 5937–5948, 2020.

[72] H. Chen and Z. Xu, "A two-dimensional constellation design method for visible light communications with signal-dependent shot noise," *IEEE Communications Letters*, vol. 22, no. 9, pp. 1786–1789, 2018.

[73] F. Chen, N. Huang, and C. Gong, "Rss-based visible light positioning with unknown receiver tilting angle: robust design and experimental demonstration," *Optics Express*, vol. 30, no. 22, pp. 39 775–39 793, 2022.

[74] J.-Y. Wang, Q.-L. Li, J.-X. Zhu, and Y. Wang, "Impact of receiver's tilted angle on channel capacity in vlcs," *Electronics Letters*, vol. 53, no. 6, pp. 421–423, 2017.

[75] A. K. Murugavel, N. Ranganathan, R. Chandramouli, and S. Chavali, "Least-square estimation of average power in digital cmos circuits," *IEEE transactions on very large scale integration (VLSI) systems*, vol. 10, no. 1, pp. 55–58, 2002.

[76] W. Wei, S. Gao, Y. Zhong, C. Gu, and G. Hu, "Adaptive square-root unscented particle filtering algorithm for dynamic navigation," *Sensors*, vol. 18, no. 7, p. 2337, 2018.

[77] R. K. Vinayak, W. Kong, G. Valiant, and S. Kakade, "Maximum likelihood estimation for learning populations of parameters," in *International Conference on Machine Learning*. PMLR, 2019, pp. 6448–6457.

[78] D. Huang, W. Lan, H. H. Zhang, and H. Wang, "Least squares estimation of spatial autoregressive models for large-scale social networks," 2019.

[79] K. Fronckova and P. Prazak, "Possibilities of using kalman filters in indoor localization," *Mathematics*, vol. 8, no. 9, p. 1564, 2020.

[80] H. Singh, A. Chattopadhyay, and K. V. Mishra, "Inverse extended kalman filter—part i: Fundamentals," *IEEE Transactions on Signal Processing*, 2023.

[81] J. K. L. Zhang and Y. Yan, "Accuracy of the frequency and phase measurement concerning different noise sources for phase doppler anemometry," in *2015 IEEE 3rd International Conference on Smart Instrumentation, Measurement and Applications (ICSIMA)*, 2015, pp. 1–6.

[82] C.-Y. Hong, Y.-C. Wu, Y. Liu, C.-W. Chow, C.-H. Yeh, K.-L. Hsu, D.-C. Lin, X.-L. Liao, K.-H. Lin, and Y.-Y. Chen, "Angle-of-arrival (aoa) visible light positioning (vlp) system using solar cells with third-order regression and ridge regression algorithms," *IEEE Photonics Journal*, vol. 12, no. 3, pp. 1–5, 2020.

[83] K. Zhang, Z. Zhang, and B. Zhu, "Beacon led coordinates estimator with selected aoa estimators for visible light positioning systems," *IEEE Transactions on Wireless Communications*, vol. 23, no. 3, pp. 1713–1727, 2023.

[84] Z. Liu, N. Stevens, and M. H. Conde, "Visible light positioning using arrays of time-of- flight pixels," in *2022 IEEE Sensors*, 2022, pp. 1–4.

[85] T. Akiyama, M. Sugimoto, and H. Hashizume, "Time-of-arrival-based smartphone localization using visible light communication," in *2017 International Conference on Indoor Positioning and Indoor Navigation (IPIN)*, 2017, pp. 1–7.

[86] S. Zhao, X.-P. Zhang, X. Cui, and M. Lu, "A new toa localization and synchronization system with virtually synchronized periodic asymmetric ranging network," *IEEE Internet of Things Journal*, vol. 8, no. 11, pp. 9030–9044, 2021.

[87] F. Garbuglia, W. Raes, J. De Bruycker, N. Stevens, D. Deschrijver, and T. Dhaene, "Bayesian active learning for received signal strength-based visible light positioning," *IEEE Photonics Journal*, vol. 14, no. 6, pp. 1–8, 2022.

[88] L. Bai, Y. Yang, C. Guo, C. Feng, and X. Xu, "Camera assisted received signal strength ratio algorithm for indoor visible light positioning," *IEEE Communications Letters*, vol. 23, no. 11, pp. 2022–2025, 2019.

[89] X. Liu, D. Zou, N. Huang, and Y. Wang, "An efficient iterative least square method for indoor visible light positioning under shot noise," *IEEE Photonics Journal*, vol. 15, no. 1, pp. 1–10, 2022.

[90] D. Astharini, S. W. Wasiati, and A. H. Lubis, "Improved extended kalman filter for photodetector based visible light positioning," *International Journal of Engineering Advanced Research*, vol. 4, no. 1, pp. 73–84, 2022.

[91] E. Shawky, M. El-Shimy, A. Mokhtar, E.-S. A. El-Badawy, and H. M. Shalaby, "Improving the visible light communication localization system using kalman filtering with averaging," *Journal of the Optical Society of America B*, vol. 37, no. 11, pp. A130–A138, 2020.

[92] Z. Li, L. Feng, and A. Yang, "Fusion based on visible light positioning and inertial navigation using extended kalman filters," *Sensors*, vol. 17, no. 5, p. 1093, 2017.

[93] P. Saengudomlert and P. Ubolkosold, "Joint position and orientation estimation for visible light positioning using extended kalman filters," in *2024 21st International Conference on Electrical Engineering/Electronics, Computer, Telecommunications and Information Technology (ECTI-CON)*, 2024, pp. 1–5.

[94] B. Zhou, A. Liu, and V. Lau, "Performance limits of visible light-based user position and orientation estimation using received signal strength under nlos propagation," *IEEE Transactions on Wireless Communications*, vol. 18, no. 11, pp. 5227–5241, 2019.

[95] S. Shi, G. Gui, Y. Lin, C. Yuen, O. A. Dobre, and F. Adachi, "Joint beamformer design and power allocation method for hybrid rf-vlcp system," *IEEE Internet of Things Journal*, vol. 11, no. 5, pp. 7878–7892, 2023.

[96] S. Ma, S. Cao, H. Li, S. Lu, T. Yang, Y. Wu, N. Al-Dhahir, and S. Li, "Waveform design and optimization for integrated visible light positioning and communication," *IEEE Transactions on Communications*, vol. 71, no. 9, pp. 5392–5407, 2023.

[97] M. Yasir, S.-W. Ho, and B. N. Vellambi, "Indoor position tracking using multiple optical receivers," *Journal of Lightwave Technology*, vol. 34, no. 4, pp. 1166–1176, 2016.

[98] J. Duan, X.-G. Wang, Y.-G. Zhou, C. Wang, and F. Grillot, "Carrier-noise-enhanced relative intensity noise of quantum dot lasers," *IEEE Journal of Quantum Electronics*, vol. 54, no. 6, pp. 1–7, 2018.

[99] L. Yin, W. O. Popoola, X. Wu, and H. Haas, "Performance evaluation of non-orthogonal multiple access in visible light communication," *IEEE Transactions on Communications*, vol. 64, no. 12, pp. 5162–5175, 2016.

[100] X. Chen and M. Jiang, "Adaptive statistical bayesian mmse channel estimation for visible light communication," *IEEE Trans. Signal Process.*, vol. 65, no. 5, p. 1287–1299, Mar 2017.

[101] D. Simon, "Optimal state estimation: Kalman, h, and nonlinear approaches. hoboken," *NJ: John Wiley and Sons, Jg*, vol. 10, p. 0470045345, 2006.

[102] B. D. Anderson and J. B. Moore, *Optimal filtering*. Courier Corporation, 2005.

[103] X. Chen, X. Wang, and J. Xuan, "Tracking multiple moving objects using unscented kalman filtering techniques," *arXiv preprint arXiv:1802.01235*, 2018.

[104] S. K. Sengijpta, "Fundamentals of statistical signal processing: Estimation theory," 1995.

[105] B. Teng, X. Yuan, R. Wang, and S. Jin, "Bayesian user localization and tracking for reconfigurable intelligent surface aided mimo systems," *IEEE Journal of Selected Topics in Signal Processing*, vol. 16, no. 5, pp. 1040–1054, 2022.

[106] Y. Chen, Y. Wang, X. Guo, Z. Han, and P. Zhang, "Location tracking for reconfigurable intelligent surfaces aided vehicle platoons: Diverse sparsities inspired approaches," *IEEE Journal on Selected Areas in Communications*, vol. 41, no. 8, pp. 2476–2496, 2023.

[107] B. Chen, L. Dang, N. Zheng, and J. C. Principe, "Kalman filtering under information theoretic criteria," in *Kalman Filtering Under Information Theoretic Criteria*. Springer, 2023, pp. 89–126.

[108] N. Kalikulov, K. Dautov, and R. C. Kizilirmak, "Location estimation for dco-ofdm based vlc in realistic indoor channel," in *2017 IEEE 11th International Conference on Application of Information and Communication Technologies (AICT)*. IEEE, 2017, pp. 1–4.

[109] J. Chu, J. Li, and T. Zong, "Parameter identification of volterra nonlinear system based on levenberg-marquardt recursive algorithm," in *2022 34th Chinese Control and Decision Conference (CCDC)*, 2022, pp. 5948–5952.

[110] D. P. Bertsekas, "Incremental least squares methods and the extended kalman filter," *SIAM Journal on Optimization*, vol. 6, no. 3, pp. 807–822, 1996.

[111] S. Horvath and H. Neuner, "Comparison of levenberg-marquardt and extended kalman filter based parameter estimation of artificial neural networks in modelling deformation processes," in *The 3rd Joint International Symposium on Deformation Monitoring, Vienna*, 2016.

[112] I. V. Stelzer, J. Kager, and C. Herwig, "Comparison of particle filter and extended kalman filter algorithms for monitoring of bioprocesses," *Computer Aided Chemical Engineering*, vol. 40, no. 1, pp. 1483–1488, 2017.